# NUMERICAL SIMULATION OF INTERFACIAL AND MULTIPHASE FLOWS USING THE FRONT TRACKING METHOD

JAN FRODE STENE
(MASTER OF SCIENCE
NORWEGIAN UNIVERSITY OF SCIENCE AND TECHNOLOGY)

A THESIS SUBMITTED FOR THE DEGREE
OF DOCTOR OF PHILOSOPHY

DEPARTMENT OF MATHEMATICS
NATIONAL UNIVERSITY OF SINGAPORE

2010

# Acknowledgements

I would first and foremost like to express my sincere gratitude towards my supervisors, Professor Lin Ping and Dr. Hua Jinsong, for their continued guidance and generous support throughout my PhD endeavours. Thanks also go to Professor Bao Weizhu who kindly filled the role as my NUS supervisor towards the end of my studies, and support staff has always made sure administrative matters have run smoothly. In addition, I am very much indebted to Professor Helmer Aslaksen who has been most helpful in personal as well as top-level academic matters.

The research scholarship provided by NUS, which gave me the opportunity to pursue this PhD in the first place, is gratefully acknowledged. I have also greatly benefited from the excellent facilities available throughout NUS, and many thanks go to the Institute of High Performance Computing (IHPC) for providing the state-of-the-art supercomputing resources necessary to obtain the extensive simulation results in the current work.

I finally thank the numerous professors and fellow students from whom I have learned so much, both at NUS and at my previous university NTNU in Norway.

London, United Kingdom Jan Frode Stene
January 2010

# Contents

# Summary

Multiphase flows are very common both in nature and in many industrial applications. One example is the rise of bubbles in viscous liquids, which is also an important fundamental problem in fluid physics. This study describes the development of a robust, fully three-dimensional direct numerical simulation algorithm and its application to the aforementioned flows. The algorithm is based on the front tracking method, originally proposed by Tryggvason and his co-workers, and has been validated against experiments over a wide range of intermediate Reynolds and Bond numbers using an axisymmetric model [J. Hua, J. Lou, Numerical simulation of bubble rising in viscous liquid, J. Comput. Phys. 22 (2007) 769-795]. In the current work, this numerical algorithm is further extended to simulate 3D bubbles rising in viscous liquids with high Reynolds and Bond numbers and with large density and viscosity ratios representative of the common airwater two-phase flow system. To facilitate the 3D front tracking simulation, mesh adaptation is implemented for both the front mesh on the bubble surface and the background mesh. On the latter mesh, the governing NavierStokes equations for incompressible, Newtonian flow are solved using a finite volume scheme based on the Semi-Implicit Method for Pressure-Linked Equations (SIMPLE) algorithm, and it appears to be robust even for high Reynolds numbers and high density and viscosity ratios. A non-inertial reference frame that moves with the rising bubble is introduced, allowing long-term simulations of rising bubbles without having to increase the size of the computational domain. The 3D bubble surface is tracked explicitly using an adaptive, unstructured triangular mesh. The numerical model is integrated with the software package PARAMESH, a block-based adaptive mesh refinement (AMR) tool developed for parallel computing. PARAMESH allows background mesh adaptation as well as the solution of the governing equations in parallel on a supercomputer. Further, Peskin distribution function is applied to interpolate the variable values between the front and the background meshes.

Detailed sensitivity analysis of the numerical modelling algorithm has been carried out, and simulation results are typically compared with experimental data in terms of bubble shapes and rise velocities. Air bubbles rising in water are simulated for a wider range of initial bubble diameters than reported elsewhere, and we also investigate Leonardo's paradox by simulating the path instability of rising bubbles. Another application studies the interaction between two rising bubbles and illustrates how the current method handles the merging of bubbles.

In the pursuit of improving the flow solver further, we also investigate the reformulation of the governing flow equations through the use of a sequential regularization method, a novel approach in the context of multiphase flows. We conclude that the new approach appears feasible, though further work would be required for a more definite assessment.

# List of Tables

# List of Figures

# Chapter 1

# Introduction

## Background

Mankind has been captivated by fluid flows for millennia due to their practical importance: the flow of water in rivers, ocean currents, wind and weather in the atmosphere or the flow of blood in our veins. While these naturally occurring phenomena remain a source of fascination, advanced industrial applications involving complex fluid flows have also become very important in the modern day. Examples include flow of oil and gas in wells and pipelines, fluidized beds, distillation and bubble columns and fuel cell systems. It is clear that fluid flows are crucial in many industries, and the understanding of these flows is therefore essential to design safe and efficient equipment and processes. Experiments have traditionally been used to gain insights into relevant flow physics, though this approach has certain limitations due to one or more of the following reasons:

- Excessively expensive in terms of time or finances

- Infeasible operating conditions, e.g. explosions (too high pressures), fires (too high temperatures) and pollution (toxic effects).
- Unacceptable interference on flow patterns from the measurement equipment

An alternative way of obtaining the desired knowledge is to develop and solve physical models describing the phenomena. The Navier-Stokes equations form the fundamental basis for the modelling of most fluid flows and were formulated almost 200 years ago. Yet, due to their complexity, it was only with the development of the electronic computer that the early numerical solutions could be obtained in the 1950s. Since then numerical algorithms have continuously been developed and improved, and at the same time computing power has evolved dramatically as well as become much more affordable. This has led to the emergence and rapid growth of the field of Computational Fluid Dynamics (CFD). While CFD has come a long way in providing key tools to a wide range of industries, the field continues to develop and still faces many challenges in the pursuit of ever more accurate results for increasingly complex systems.

**Categories of fluid flow**

It is often useful to categorize the abundance of both natural and industrial occurring fluid flows, and a variety of categorizations are possible depending on the point of interest. In the current work we make a distinction between *single* and *multiphase* flows. Single phase flows involve fluids consisting of one or more components where all components are either in the gas phase (e.g. air) or liquid phase (e.g. sea water). Put simply we may then say that multiphase flows encompass all other types of fluid flows. Another category is *interfacial* flows which is characterized by the presence of an interface due the immiscibility of two or more fluids. Single phase flows may be interfacial, e.g. flow involving oil and water, while an interface will always be present in multiphase flows. It is multiphase and interfacial flows that will be investigated in this thesis - specifically in the context of gas bubbles rising in viscous liquids.

## Current work and contribution

Researchers Jinsong Hua and Jing Lou at the Institute of High Performance Computing (IHPC) in Singapore validated an improved numerical algorithm based on the front tracking method against experiments over a wide range of intermediate Reynolds and Bond numbers for gas bubbles rising in viscous liquids using an axisymmetric model [50]. That formed the starting point of the current work which was carried out as a research collaboration between the Department of Mathematics at the National University of Singapore (NUS) and the Computational Fluid Dynamics group at IHPC. The main objective was as follows:

> Develop a state-of-the-art three-dimensional solution algorithm capable of simulating realistic bubble flows and hence providing more insights into the fundamentals of bubble dynamics.

The aptitude of the method that has been developed lies in the combination of several powerful components, modifying and integrating them to obtain an overall simulation algorithm with cutting-edge capabilities. Present contributions include:

- The development and implementation of a robust, fully three-dimensional simulation algorithm with these key components:
    - The moving interface is handled using a front tracking approach
    - A Semi-Implicit Method for Pressure-Linked Equations (SIMPLE) is adopted and modified to handle discontinuities present in the governing Navier-Stokes equations due the interface
    - The SIMPLE flow solver is integrated with PARAMESH: a block-based, adaptive mesh refinement (AMR) tool for multi-processing
- Simulation of flows in an extended, wider range of Reynolds and Bond numbers for large, realistic ratios of the density and viscosity of the fluids:
    - Simulation of air bubbles rising in pure water for bubble diameters from 0.5 mm to 30 mm, far wider than other simulations reported in the literature
    - Reproduction of path instability for rising bubbles through the use of a non-inertial moving reference frame, using less simplifying assumptions than reported elsewhere in the literature
- Reformulation of the governing equations through the use of a sequential regularization method - a novel approach in the context of multiphase flows.

Some results of this work have been published in the Journal of Computational Physics [49] and in Moving Interface Problems and Applications in Fluid Dynamics, a volume of Contemporary Mathematics by the American Mathematical Society [47]. Highlights were also presented at the 6th International Conference on Multiphase Flow in Leipzig, Germany, in 2007 [48], and these publications form a very important part of this thesis.

# Thesis outline

This thesis is structured as follows. Motivation and a detailed statement of the model problem is given in Chapter 2 along with an overview of the main computational techniques typically deployed to solve the problem. The specific method of choice that is adopted and further developed in the current work is then comprehensively described in Chapter 3. The implementation and feasibility of this method is then assessed thoroughly in Chapter 4 through sensitivity analyses and validation against experimental results. The powerful capabilities of the simulation algorithm is further demonstrated when applied to study two complex multiphase phenomena: path instability of rising bubbles and the interaction of two rising bubbles in Chapters 5 and 6, respectively. A reformulation of the model problem through sequential regularization and a modified solution algorithm is investigated in Chapter 7, while Chapter 8 finally concludes this thesis with a summary of the main conclusions and recommendations for further work.

# Chapter 2

# Model Problem and Computational Techniques

## 2.1 Introduction

In the previous chapter we illustrated how multiphase flows play an important role in both everyday life and engineering practice. It is clear that various types of multiphase flows can vary dramatically in terms of complexity. One basic and important example is the rise of a single gas bubble in an otherwise quiescent viscous liquid, e.g. a bubble of air rising in water. The understanding of the flow dynamics of this system is of great importance in engineering applications and to the fundamental understanding of multiphase flow physics, and it is indeed this system that will be the model problem of choice in this thesis.

Rising bubbles have long been studied theoretically [24, 76], experimentally [6] as well as computationally through numerical modelling [97]. While all these efforts have provided us with valuable insights into the dynamics of bubbles rising in viscous liquids, there are still many questions that remain unanswered due to the involvement of complex physics. The behaviour of a bubble rising in a viscous liquid is not only affected by the physical properties such as density and viscosity of both phases (see [21]), but also by the surface tension on the interface between the two phases and by the bubble shape evolution [82, 8]. The difficulties in describing and modelling the complex behaviour of a rising bubble are to a large extent due to the coupling of factors such as buoyancy, surface tension, bubble/liquid momentum inertia, viscosity, bubble shape evolution and rise history of the bubble. Several of these factors are coupled in a highly nonlinear manner, making the situation even more complex. In addition, the physics of the behaviour of bubbles is of a three-dimensional nature. Due to the enormous complexity of the fully three-dimensional governing equations, most of the past theoretical works were done with a lot of assumptions, and the results are thus only valid for certain flow regimes [76, 109]. Furthermore, the experimental works were limited by the available technologies to monitor, probe and sense the moving bubbles without interfering with their physics [6, 111, 104].

We have mentioned both theoretical and experimental difficulties that researchers face when studying bubbles rising in a viscous liquid. With the rapid advance of computing power and the continuous improvement of numerical methods, first principle based numerical simulations promise great potential in extending our knowledge of multiphase flows in general, and of the fundamental system of a single bubble rising in a viscous liquid in particular. Nevertheless, there are still great challenges and difficulties in simulating such a system accurately. This may be attributed to the following facts:

1. the sharp interface between the gas bubble and the surrounding liquid should be tracked accurately without introducing excessive numerical smearing

2. the surface tension gives rise to a singular source term in the governing equations, leading to a sharp pressure jump across the interface

3. the discontinuity of the density and viscosity across the fluid interface may lead to numerical instability, especially when the jumps in these properties are high. For example, the density ratio of liquid to gas could be as high as 1000

4. the geometric complexity caused by bubble deformation and possible topological change is the main difficulty in handling the geometry of the interface; a large bubble may break up into several small ones, and a bubble may also merge with other bubbles

5. the complex physics on the interface, e.g. the effects of surfactants, film boiling and phase change (heat and mass transfer) and chemical reactions

Fortunately, various methods for multiphase flow have been developed to address these difficulties, and each method typically has its own characteristic strengths and weaknesses. An overview of various relevant numerical methods will follow in Section 2.3, while the numerical methodology adopted in this thesis is described in detail in Chapter 3. However, let us first turn our attention to the mathematical formulation of the model problem, which will be presented in Section 2.2

## 2.2 Model and governing equations

This section will establish the mathematical formulation of our model problem and its associated notation. Much of the derivations and equations presented here are quite standard and can be found in numerous publications on fluid dynamics - the author found Batchelor's classic book from 1967 particularly useful [5]. More recent references used for this section include the Von Karman lecture notes [112] by Tryggvason et al. as well as the review paper [102] by Scardovelli and Zaleski.

### 2.2.1 Mass conservation

The principle of conservation of mass is the basis for the continuity equation. Consider a closed piecewise smooth surface $S$ that encloses a volume $V$ within our fluid domain. The total fluid mass in $V$ at time $t$ can then be expressed as $M_V(t) = \int \rho dV$. Further, the mass leaving the volume $V$ at time $t$ can be expressed as $\int \rho \mathbf{u} \cdot \mathbf{n} dS$, where $\mathbf{n}$ is the outer unit normal of the surface $S$. Ignoring any mass sources/sinks, the rate of change of the mass in the volume $V$ can then be expressed as

$$\frac{d}{dt}\iiint_V \rho dV = -\iint_{\partial V} \rho \mathbf{u} \cdot \mathbf{n} dS. \tag{2.1}$$

Assuming that the velocity $\mathbf{u}$ is continuously differentiable, we can apply the divergence theorem to the right-hand side of Equation (2.1):

$$\iint_{\partial V} \rho \mathbf{u} \cdot \mathbf{n} dS = \iiint_V \nabla \cdot (\rho \mathbf{u}) dV \tag{2.2}$$

Substituting the right-hard side of Equation (2.2) into Equation (2.1) and differentiating under the integral sign since the volume $V$ is independent of time, yields

$$\iiint_V \Big[\frac{\partial \rho}{\partial t} + \nabla \cdot (\rho \mathbf{u})\Big] dV = 0 \tag{2.3}$$

Now this equation is valid for an arbitrarily chosen volume $V$ with a piecewise smooth boundary, and hence

$$\frac{\partial \rho}{\partial t} + \nabla \cdot (\rho \mathbf{u}) = 0 \tag{2.4}$$

at all points in the fluid domain. In this thesis we shall generally assume that the flow is *incompressible* - namely that the material derivative of the density $\frac{D\rho}{Dt}$ is zero:

$$\frac{D\rho}{Dt} = \frac{\partial \rho}{\partial t} + \mathbf{u} \cdot \nabla \rho = 0 \tag{2.5}$$

Combining Equation (2.4) and (2.5) then yields this simple mass conservation condition for incompressible flow:

$$\nabla \cdot \mathbf{u} = 0. \tag{2.6}$$

### 2.2.2 Momentum conservation

**Single phase flow**

The general form of the Navier-Stokes equation for a single compressible Newtonian fluid can be expressed in vector form as:

$$\frac{\partial (\rho \mathbf{u})}{\partial t} + \nabla \cdot \rho \mathbf{u}\mathbf{u} = -\nabla p + \nabla \cdot (\mu(\nabla \mathbf{u} + (\nabla \mathbf{u})^T)) + \rho \mathbf{g}, \tag{2.7}$$

where $\mathbf{uu} = \mathbf{uu}^T$ is a matrix. Assuming incompressible flow with constant viscosity $\mu$ and constant density $\rho$, Equation (2.7) simplifies to

$$\rho(\frac{\partial \mathbf{u}}{\partial t} + \mathbf{u} \cdot \nabla \mathbf{u}) = -\nabla p + \mu \nabla^2 \mathbf{u} + \rho \mathbf{g}, \tag{2.8}$$

where $\nabla^2 \mathbf{u} = \nabla \cdot (\nabla \mathbf{u})$.

### Two-phase flow

Assume that we have two immiscible Newtonian fluids. We will now have an additional force at the interface between the two fluids due to surface tension, leading to an additional term in the momentum equation as compared to Equation (2.7) governing single phase flow. The modified equation is

$$\begin{aligned}\frac{\partial(\rho \mathbf{u})}{\partial t} + \nabla \cdot \rho \mathbf{uu} = &- \nabla p + \nabla \cdot \big(\mu(\nabla \mathbf{u} + (\nabla \mathbf{u})^T)\big) \\ &+ \int_\Gamma \sigma \kappa \mathbf{n} \delta(\mathbf{x} - \mathbf{x}_\Gamma) dS + (\rho - \rho_L)\mathbf{g}.\end{aligned} \tag{2.9}$$

It is here worth pointing out that the density $\rho$ and viscosity $\mu$ will be discontinuous across the two-fluid interface $\Gamma$, for example, across a liquid-gas interface which we shall focus on in this thesis. The equation is then valid throughout the domain for both phases and is often referred to as the 'one-fluid' or 'whole-domain' formulation.

The surface tension term is a singular source term that is non-zero only at the interface between the liquid and the gas phase. In Equation 2.9 this is expressed by the use of three-dimensional delta distribution $\delta(\mathbf{x}) = \delta(x_1)\delta(x_2)\delta(x_3)$, where $\mathbf{x} = (x_1, x_2, x_3)$.

### Two-fluid formulation

An alternative formulation of the governing equation can be obtained by splitting the flow domain into two parts: one part contains the liquid phase and the other part contains the gas phase. In this case we may write down the momentum equations for each phase separately, namely

$$\rho_L(\frac{\partial \mathbf{u}}{\partial t} + \mathbf{u} \cdot \nabla \mathbf{u}) = -\nabla p + \mu_L \nabla^2 \mathbf{u} + \rho_L \mathbf{g} \tag{2.10}$$

for the liquid phase and

$$\rho_G(\frac{\partial \mathbf{u}}{\partial t} + \mathbf{u} \cdot \nabla \mathbf{u}) = -\nabla p + \mu_G \nabla^2 \mathbf{u} + \rho_G \mathbf{g} \tag{2.11}$$

for the gas phase. Each of these equations will be accompanied by the continuity equation $\nabla \cdot \mathbf{u} = 0$. The surface tension between the two phases then couples the two momentum equations through the following stress balance on the interface:

$$[-p + \mu(\nabla \mathbf{u} + \nabla^T \mathbf{u})] \cdot \mathbf{n} = \sigma\kappa\mathbf{n} \quad \text{and} \quad [\mu(\nabla \mathbf{u} + \nabla^T \mathbf{u})] \cdot \mathbf{t} = 0, \tag{2.12}$$

where $[z]$ represents the jump of the variable $z$ at the interface. Further details on these interfacial jump conditions may be found in either [112] or [102].

### A note on the incompressibility assumption

Above we have assumed that the fluid is incompressible throughout the domain. Whereas this is a very common assumption for many liquid flows, single phase gas flows are often treated as compressible. As such we here briefly justify our assumption of an incompressible gas phase inside the rising bubble.

Batchelor [5, pp. 167–169] gives a detailed theoretical discussion on the necessary conditions for a fluid to be approximately incompressible. The most important condition applicable to our system is $\frac{u^2}{c^2} << 1$, where $u$ is the magnitude of the fluid velocity $\mathbf{u}$ and $c$ is the local speed of sound. The speed of sound in air at typical atmospheric conditions is approximately 340 m/s, which roughly means that the condition is satisfied if the fluid velocity is less than 100 m/s.

In Chapter 4.3 numerical results based on the incompressible fluid assumption are compared with experimental data in terms of velocity and shape of single air bubbles rising in liquid. The model predictions agree well with experimental results, indicating that the incompressibility assumption for the gas phase is reasonable. This observation is supported by Pianet et al. [89] who carried out two sets of numerical simulations, considering both incompressible and compressible single gas bubbles rising in liquid. The two sets of results that were obtained are very similar and thus show only a negligible effect of compressibility.

It should be noted, however, that there are other two-phase flow systems where the gas phase may not be considered incompressible. In such cases one may model the liquid phase as incompressible and the gas phase as compressible as done in the work by Caiden et al. [17].

### 2.2.3 Non-dimensional governing equations

To gain further insight into a physical system, it is often beneficial to express its governing equations in a non-dimensional form. We here define the effective bubble diameter $D = \sqrt[3]{6V_B/\pi}$ as the characteristic length, where $V_B$ is the bubble volume. We may thus introduce the following dimensionless characteristic variables:

$$\begin{aligned} x^* = \frac{x}{D}, \quad u^* = \frac{u}{\sqrt{gD}}, \quad t^* = \sqrt{\frac{g}{D}}t, \quad \rho^* = \frac{\rho}{\rho_L}, \\ p^* = \frac{p}{\rho_L g D}, \quad \mu^* = \frac{\mu}{\mu_L} \quad \kappa^* = D\kappa \text{ and } \mathbf{g}^* = \frac{\mathbf{g}}{g}, \end{aligned} \tag{2.13}$$

where $g = \|\mathbf{g}\|$. Let us also introduce two useful dimensionless numbers - namely the Archimedes and Bond numbers - defined as

$$Ar = \frac{\rho_L \sqrt{gD^3}}{\mu_L} \text{ and } Bo = \frac{\rho_L g D^2}{\sigma}, \tag{2.14}$$

respectively. Utilizing these quantities, we may re-express the governing equations in non-dimensional form as follows:

$$\nabla \cdot \mathbf{u}^* = 0 \tag{2.15}$$

and

$$\begin{aligned}\frac{\partial(\rho^*\mathbf{u}^*)}{\partial t^*}+\nabla\cdot\rho^*\mathbf{u}^*\mathbf{u}^* =&-\nabla p^*+\frac{1}{Ar}\nabla\cdot\big(\mu^*(\nabla\mathbf{u}^*+(\nabla\mathbf{u}^*)^T)\big)\\&+\frac{1}{Bo}\int_{\Gamma^*}\kappa^*\mathbf{n}\delta(\mathbf{x}^*-\mathbf{x}^*_{\Gamma^*})dS^*+(\rho^*-1)\mathbf{g}^*.\end{aligned}\tag{2.16}$$

The non-dimensionalization of the surface integral term is non-trivial and is based on the following relations:

$$\begin{aligned}\int_{\Gamma}\sigma\kappa\mathbf{n}\delta(\mathbf{x}-\mathbf{x}_\Gamma)dS=&\int_{\Gamma^*}\sigma\frac{\kappa^*}{D}\mathbf{n}\delta(D\mathbf{x}^*-D\mathbf{x}^*_{\Gamma^*})d(D^2S^*)\\=&D\int_{\Gamma^*}\sigma\kappa^*\mathbf{n}\frac{1}{D^3}\delta(\mathbf{x}^*-\mathbf{x}^*_{\Gamma^*})dS^*=\frac{1}{D^2}\int_{\Gamma^*}\sigma\kappa^*\mathbf{n}\delta(\mathbf{x}^*-\mathbf{x}^*_{\Gamma^*})dS^*.\end{aligned}$$

For simplicity and ease of notation, we shall subsequently omit the (*) superscript, such that the final form of the non-dimensional governing equations are expressed as:

$$\nabla\cdot\mathbf{u}=0\tag{2.17}$$

and

$$\begin{aligned}\frac{\partial(\rho\mathbf{u})}{\partial t}+\nabla\cdot\rho\mathbf{u}\mathbf{u}=&-\nabla p+\frac{1}{Ar}\nabla\cdot\big(\mu(\nabla\mathbf{u}+(\nabla\mathbf{u})^T)\big)\\&+\frac{1}{Bo}\int_{\Gamma}\kappa\mathbf{n}\delta(\mathbf{x}-\mathbf{x}_\Gamma)dS+(\rho-1)\mathbf{g}.\end{aligned}\tag{2.18}$$

It is indeed Equations (2.17) and (2.18) that will be the starting point for our numerical solution methodology.

### A note on dimensionless numbers

By studying the non-dimensional formulation, it can be noticed that the flow is entirely characterized by the following four dimensionless parameters: the density and viscosity ratios of the fluids, the Archimedes number and the Bond number. The Archimedes number was also used in the previous work [8] to characterize the rise of a bubble in liquid due to buoyancy, reflecting the ratio of buoyancy to viscous forces. In experimental work it is common to use a different set of dimensionless numbers [6], the most important one being the bubble Reynolds number $Re$:

$$Re = \frac{\rho_L D U_\infty}{\mu_L}, \tag{2.19}$$

where $U_\infty$ is the experimentally measured terminal velocity of the rising bubble. Another dimensionless number one may encounter in this setting is the Froude number $Fr$:

$$Fr = \frac{U_\infty}{\sqrt{gD}}. \tag{2.20}$$

We thus have the following relationship between the Archimedes number of our formulation and the Reynolds number used in experiments: $Re = Ar \cdot Fr$. Finally, we mention two other dimensionless numbers frequently used by experimentalists, namely the Eötvös number ($E$), which is exactly the same as the Bond number ($Bo$) defined above, and the Morton number $M$:

$$M = \frac{g\mu_L^4}{\rho_L \sigma^3} = \frac{Bo^3}{Ar^4}. \tag{2.21}$$

## 2.3 Overview of main computational techniques

The purpose of this section is to provide the reader with an overview of some of the main computational techniques that are used for multiphase and interfacial flow simulations. More comprehensive reviews of such numerical methods have been given by Scardovelli and Zaleski [102] and Annaland et al. [116]. For even more in-depth description of computational methods for multiphase flows the reader is referred to very recent books on the topic by Prosperetti and Tryggvason [91] from 2007 and by Yeoh and Tu [121] from 2009.

Most of the current numerical techniques applied in the simulation of multiphase/interfacial flows have been developed with focus on the following two main aspects: (i) capturing/tracking the sharp interface, e.g. interface capturing, grid fitting, front tracking or hybrid methods as elaborated in Section 2.3.1; and (ii) stabilizing the flow solver to handle discontinuous fluid properties and highly singular interfacial source terms, e.g. the projection-correction method [116] and the SIMPLE algorithm [21, 50]. More details on flow solvers follow in Section 2.3.2.

### 2.3.1 The fluid-fluid interface

The volume of fluid [44, 11, 95, 16], level-set [85, 107, 103, 83, 84] and phase-field [1, 52, 122, 18] approaches fall into the first category of front capturing methods. In these methods the interface is captured using various volume functions defined on the grid that is used to solve the one-fluid formulation of the governing equations for multiphase flow. Since the interface capturing method uses the same grid as the flow solver, it is relatively easy to implement. However, the accuracy of this approach is limited by the numerical diffusion from the solution of the convection equation of the volume function. Various schemes have been developed to advect, reconstruct / reinitialize the volume function to improve the accuracy in calculating the interface position. One example is the high-order shock-capturing scheme used to treat the convective terms in the governing equations [51]. Although the explicit reconstruction of the interface is circumvented, the implementation of such high-order schemes is quite sophisticated, and they do not work well for the sharp discontinuities encountered in multiphase/interfacial flows. In addition, a relatively fine grid is needed in the vicinity of the interface to obtain good resolution. Nevertheless, some impressive fully 3D results of single bubbles rising using a VOF method have been presented by Bothe and coworkers [58, 9].

The second category of approaches tries to track the moving interface by fitting the background grid points to the interface. The fitting is achieved through re-meshing techniques such as deforming, moving, and adapting the background grid points. This method is also well-known as boundary-fitting approach, and the boundary here refers to the interface between the fluids. The grid-fitting approach [97, 56, 10] is capable of capturing the interface position accurately. Early development on this approach was done by Ryskin and Leal [97]. Curvilinear grids were used to follow the motion of a rising bubble in liquid. This method is suitable for relatively simple geometries undergoing small deformations, and applications to complex, fully three-dimensional problems with unsteady deforming phase boundaries are very rare. This is mainly due to difficulties in maintaining the proper volume mesh quality and in handling complex interface geometry such as topological change. In spite of these difficulties, recent work by Hu et al. [46] showed some very impressive results on 3D simulations of moving spherical particles in liquid.

The third category is the front tracking method. This method generally solves the flow field on a fixed grid and tracks the interface position in a Lagrangian manner by a separate set of interface markers. The approach used in this work is based on front tracking, and a review of front tracking in general can be found in Section 3.1.1. This is then followed by a detailed description of the approach adopted in this thesis in Section 3.2.

### 2.3.2 The equations governing the flow field

Besides the numerical techniques employed to capture/track the moving interface, it is also very important to develop a stable numerical method to solve the governing equations of the flow field. Some investigators have considered simplified models such as Stokes flow [90], where inertia is completely ignored, and inviscid potential flow [45], where viscous effects are ignored in. In both cases, the motion of deformable boundaries can be simulated with boundary integral techniques. However, when considering the transient Navier-Stokes equations for incompressible, Newtonian fluid flow, the so-called ”one-fluid” formulation for multiphase flow has proved most successful [11, 107, 113]. The governing equation for this approach is given by (2.9) and also comes with certain challenges: the fluid density and viscosity are discontinuous across the fluid interface, and the surface tension is a singular source term. Various techniques have been developed to deal with these difficulties, including the immersed boundary method by Peskin that dates back to 1977 [87] - see [88] for a recent review of the method. A notable method motivated by Peskin's approach is the immersed interface method by LeVeque and Li [60, 61]. Other popular modern methods that use the "one-fluid" formulation include the projection-correction method [111, 116] and the SIMPLE algorithm [21, 50]. Various multiphase/interfacial flow problems have been successfully simulated by the front tracking method [113] with a projection-correction flow solver. It appears that previously reported results have been limited to flows with low to intermediate Reynolds numbers (<100) and small density ratios (<100) [15]. It is thus natural to reexamine the approach with an aim to make it more robust and applicable to wider flow regimes. Some revised versions of the project-correction method have been proposed to improve its capability in handling situations with large density and viscosity ratios [116]. Recently, Hua and Lou [50] tested a SIMPLE-based algorithm to solve the incompressible Navier-Stokes equations. Their axisymmetric simulation results indicate that the newly proposed method can robustly solve the Navier-Stokes equations with large density ratios up to 1000 and large viscosity ratios up to 500. Due to its apparent robustness, this solver has been extended to full 3D and deployed in this study. A detailed description of the approach follows in Chapter 3.

# Chapter 3

# Front Tracking for Two-Phase Flow: The Method

## 3.1 Introduction

The historical evolution of the front tracking approach up and its current adaptation in this thesis is discussed later on in this introduction. Section 3.2 gives a detailed description of the treatment of the moving interface, while the solver for the governing flow equations is the topic of Section 3.3. The implementation of a moving reference frame is then discussed in Section 3.4, and Section 3.5 presents the relevant boundary conditions. Finally the chapter is concluded by a summary of the solution algorithm in Section 3.6.

### 3.1.1 A brief history of the front tracking approach

The idea of front tracking was introduced by Richtmyer and Morton in the 1960s [94]. Front tracking methods have evolved and been continually improved on ever since, and several variations of what is referred to as front tracking methods exist today. Generally these methods solve the flow field on a background grid and tracks the interface position in a Lagrangian manner by a set of separate interface markers. These interface markers can be free particles without connection, or they can be logically connected elements, possibly containing accurate geometric information about the interface such as area, volume, curvature, deformation, etc. The background grid used for solving the flow equations may be completely fixed and used with the one-fluid formulation, or it may be modified near the interface for use with the two-fluid formulation.

One early implementation of the front tracking technique was proposed by pioneer researchers Glimm and his coworkers in the early 1980s [37]. That variation of front tracking has been developed extensively [38, 35, 36, 99], and includes their well-established FronTier code, part of which has been made publicly available [30]. Applications have typically been to hyperbolic systems such as the Euler equations of compressible gas flow. They represent the front interface using a set of moving markers and solve the flow field on a separate background grid. The background grid is modified only near the front to make background grid points coincide with the front markers of the interface. In this case, some irregular grids are reconstructed and special finite difference stencils are created for the flow solver, increasing the complexity of the method and making it more difficult to implement.

Independently, another front tracking technique was developed by Peskin and collaborators [34, 87]. In their method, the interface is represented by a connected set of particles that carry forces, either imposed externally or adjusted to achieve a specific velocity at the interface. A fixed background grid is kept unchanged even near the front interface, and the interface forces are distributed onto the background to solve the ”one-fluid” formulation of the flow equations.

A number of combinations and improvements of these basic approaches have been proposed to enhance the capabilities in dealing with the sharp, moving interface where complex physical phenomena and processes could occur. One of the most promising approaches is arguably the front tracking method as proposed by Tryggvason and his collaborators. Its origin can be traced back to the landmark paper [114] by Unverdi and Tryggvason in 1992. Numerous modifications and improvements have since been introduced and applied to various two- and three-dimensional multiphase problems [108, 55, 41, 42, 113, 15, 33, 67, 77, 110]. Dijkhuizen et. al. also very recently published work in this area with three accompanying papers: one paper described their improved front tracking method [28], while the two other papers validated their method with particular focus on the lift [26] and drag [27] forces on single rising bubbles.

Actually, this approach may be viewed as a hybrid method: a fixed background grid is used to solve the fluid flow just as in traditional front capturing methods, while a separate interface mesh is used to track the interface position explicitly in a typical of front tracking manner. The tracked interface carries information about jumps in the density and the viscosity and also about interfacial forces such as surface tension. Fluid properties are then distributed onto the fixed background grid according to the position of the interface. The surface tension can be calculated according to the geometry of the interface and is also distributed onto the background grid in the vicinity of the interface.

Inspired by the Tryggvason approach of dealing with the interface, Hua and Lou [50] presented a 2D axisymmetric model using a robust SIMPLE-based solver for the flow equations. They presented extensive simulations and model validation on a single bubble rising in a quiescent liquid. The comprehensive simulations showed good results in a wide flow regime with high density and viscosity ratios, and the algorithm is as such promising in the direct numerical simulation of multiphase flow. It is indeed this very approach that is the origin of the method adopted in this thesis.

### 3.1.2 Motivation and strengths of current approach

Even though the studies by Hua and Lou [50] showed great promise, they were unfortunately limited to the 2D axisymmetric model where fluid flows and bubble shapes are assumed to be axisymmetric. Hence, it would be interesting to investigate the robustness of the proposed numerical approach for multiphase flow in flow regimes of higher Reynolds and Bond numbers where the bubble may not be axisymmetric anymore. Therefore, a fully three-dimensional modelling approach is proposed in this study. In addition, other features such as mesh adaptation, a moving reference frame and parallel processing are introduced to enhance the model capability in simulating the rise of a 3D bubble in a viscous liquid.

The governing Navier-Stokes equations are solved on a fixed Cartesian grid with an adaptive block structure, while the interface is represented by a set of explicitly tracked front markers. These markers form an adaptive triangular surface mesh that is advected with a velocity interpolated from the surrounding fluid. An illustration of such a mesh system is shown in Figure 3.1. A single set of the governing equations is solved in the entire computational domain by treating the two fluids as one single fluid with variable fluid properties across the interface - often referred to as the ”one-field” or ”one-fluid” approach. The interface is assumed to have a given finite thickness (normally about two to four times the background grid size) so that jumps in the fluid properties across the surface can be reconstructed smoothly by solving a Poisson equation. A parallel adaptive mesh refinement (AMR) tool, PARAMESH [70], is integrated with the modified SIMPLE flow solver, and the governing equations are solved in a non-inertial moving reference frame attached to the rising bubble.

The AMR feature crucially allows a relatively high-resolution mesh in the vicinity of the bubble surface. The non-inertial moving reference frame technique translates the computational domain with the rising bubble, allowing the computational domain to be relatively small and always centred around the bubble. The latter feature is particularly useful for studying the path instability of a rising bubble or the interaction of multiple bubbles, which may need very long simulation periods. For example, it is observed in experiments that the paths of millimetre-sized air bubbles rising in water normally stabilize after a rise distance of 50-100 times the initial bubble diameter. If a stationary frame were applied to simulate this situation, the computational domain would be huge compared to the domain of interest, and the total number of grid points could too large even though an AMR feature is adopted. The SIMPLE-based flow solver avoids solving the pressure equation directly and is shown to be robust even for large density and viscosity ratios.

In conclusion, this front tracking approach combined with several powerful features as described above have proven to be a very capable methodology for simulating the rise of fully three-dimensional bubbles in a viscous liquid. We now turn our attention to details of its implementation.

## 3.2 Front tracking as adopted in this study

### 3.2.1 Overview

When the governing Navier-Stokes equations are solved numerically on a fixed grid, the values of the density and viscosity on these grid points are required. Hence the density and viscosity are physically discontinuous across the interface

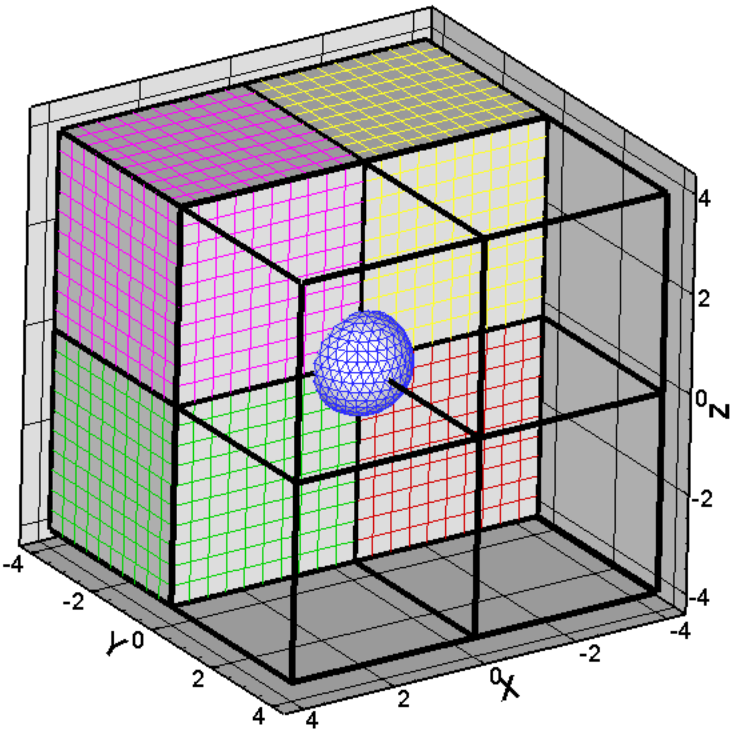

Figure 3.1: Simulation of a single bubble rising using the front tracking method. Multiple unstructured blocks with Cartesian mesh are used for the flow solver while the bubble surface is represented by an unstructured triangular mesh.

between the two immiscible fluids, and this abrupt jump at grid points adjacent to the interface has traditionally caused great problems in many numerical methods. In Tryggvason et al. [114, 113] a fixed background mesh is adopted to solve the governing flow equations, and a separate mesh is applied to track the position of the interface as well as the discontinuities across the front. An illustration of such a mesh system is shown in Figure 3.1. The discontinuities across the front are distributed from the front mesh to the background mesh, and continuous distributions of the fluid properties can be reconstructed on the fixed background mesh. The singular source term on the interface is distributed to the background grid similarly, and the governing equations can thus be solved on the fixed background grid using any preferred numerical approach.

### 3.2.2 A smooth indicator function

It is a reasonable assumption that each fluid is incompressible, and fluid properties such as density and viscosity are constant in each fluid phase. Consequently an important feature of the governing Navier-Stokes Equation (2.18) is that the material properties density $\rho$ and viscosity $\mu$ will be discontinuous across the bubble interface. A preliminary step in solving Equation (2.18) is therefore to determine the value of the material properties throughout the fluid domain. Let $b(\mathbf{x}, t)$ represent either the density or viscosity, and let $I(\mathbf{x}, t)$ be an indicator function that is zero in the liquid phase and 1 in the gas phase. We may then define the material property in terms of the indicator function:

$$b(\mathbf{x}, t) = b_L + (b_G - b_L) \cdot I(\mathbf{x}, t) \tag{3.1}$$

where $L$ and $G$ refer to the liquid and gas phase, respectively. Further let $\Omega$ be the domain of the gas phase and let Γ be the interface between the two phases. The indicator function may then be expressed as

$$I(\mathbf{x}, t) = \int_{\Omega(t)} \delta(\mathbf{x} - \mathbf{x}_{\mathbf{\Omega}}) dV \tag{3.2}$$

Taking the gradient of the indicator function and applying Stokes' theorem, we get

$$\nabla I(\mathbf{x}, t) = \int_{\Omega(t)} \nabla \delta(\mathbf{x} - \mathbf{x}_{\mathbf{\Omega}}) dV = \int_{\Gamma(t)} \mathbf{n} \delta(\mathbf{x} - \mathbf{x}_{\mathbf{\Gamma}}) dS \tag{3.3}$$

where **n** is the outer unit normal vector of the interface. Proceeding by taking the divergence then yields a Poisson equation for the indicator function:

$$\nabla^2 I(\mathbf{x}, t) = \nabla \cdot \int_{\Gamma(t)} \mathbf{n} \delta(\mathbf{x} - \mathbf{x}_{\mathbf{\Gamma}}) dS \tag{3.4}$$

By solving this equation we can then obtain the distribution of material properties from Equation (3.1). However, the integrand of Equation (3.4) is discontinuous across the front and therefore poses considerable numerical difficulties.

Using the ideas of Peskin [87], Unverdi and Tryggvason [114] addressed the sharp jump in fluid properties across the interface in their front tracking algorithm. They introduced an artificial thickness of the interface inside which the material properties vary continuously from one fluid to the other. According to this idea, a distribution function $D(\mathbf{x})$ is introduced to approximate the delta function $\delta(\mathbf{x})$ with the assumption of an artificial thickness of the interface. We here adopt the traditional Peskin distribution function [87],

$$D(\mathbf{x}) = \begin{cases} \frac{1}{(4h)^3} \prod_{i=1}^{3} \Big(1 + \cos\big(\frac{\pi}{2h}|x_i|\big)\Big) & \text{if } |\mathbf{x}| < 2h, \\ 0 \quad \text{otherwise.} \end{cases} \tag{3.5}$$

Here the artificial thickness is equal to $2h$. One may now replace the delta function in Equation (3.4) with this continuous $D(\mathbf{x}, t)$ to obtain

$$\nabla^2 I(\mathbf{x}, t) = \nabla \cdot \int_{\Gamma(t)} \mathbf{n} D(\mathbf{x} - \mathbf{x}_{\boldsymbol{\Gamma}}) dS. \tag{3.6}$$

Solving this modified Poisson equation will result in a smooth indicator function which will be zero in the liquid phase, vary continuously from zero to one in the artificial thickness region, and be one in the gas phase. Therefore Equation (3.6) is far more feasible to solve numerically than Equation (3.4).

### 3.2.3 The surface tension term

In addition to the discontinuity in fluid properties across the bubble interface, the surface tension is a singular source term that represents another significant challenge for numerical methods in multiphase flow. From Equation (2.9) we see that the surface tension force $\mathbf{F}_\sigma$ is given by

$$\mathbf{F}_\sigma(\mathbf{x}) = \int_{\Gamma} \sigma \kappa \mathbf{n} \delta(\mathbf{x} - \mathbf{x}_{\boldsymbol{\Gamma}}) dS. \tag{3.7}$$

There are two clear challenges in dealing with this term. Firstly, the delta function poses the same problems as mentioned previously, and we will address this by using the approximate $D(\mathbf{x})$ as defined in Equation (3.5). Secondly, the curvature $\kappa$ is defined in terms of second-order derivatives which are challenging to compute numerically. Therefore an alternative method is used in the current work to compute the surface tension force $\mathbf{F}_\sigma$. The bubble interface is triangulated and represented by $N$ triangles. This allows the net force $\mathbf{F}_\sigma$ to be calculated as a sum of the individual surface tension forces $\mathbf{F}_{\sigma,\mathbf{k}}$ on each surface element $k$:

$$\mathbf{F}_\sigma = \sum_{k=1}^{N} \mathbf{F}_{\sigma,k} D(\mathbf{x} - \mathbf{x_k}), \tag{3.8}$$

where $\mathbf{x}_k$ is the mass centre of the $k$-th surface element. The net surface tension force $\mathbf{F}_{\sigma,k}$ on the $k$-th element is then simply calculated as the sum of the surface tension forces $\mathbf{F}_{\sigma,k,i}$ on the three edges of the element:

$$\mathbf{F}_{\sigma,k} = \sum_{i=1}^{3} \mathbf{F}_{\sigma,k,i}. \tag{3.9}$$

The remaining question now is how do we calculate the surface tension force $\mathbf{F}_{\sigma,k,i}$ on the $i$-th edge of the $k$-th triangle? Based on the quantities defined in Figure 3.2 we get

$$\mathbf{F}_{\sigma,k,i} = \sigma(\mathbf{t}_{k,i} \times \mathbf{n}_{k,i,0}) \tag{3.10}$$

Thus we finally obtain the following expression for the surface tension force term:

$$\mathbf{F}_{\sigma}(\mathbf{x}) = \sigma \sum_{k=1}^{N} \Big[ D(\mathbf{x} - \mathbf{x}_k) \sum_{i=1}^{3} \big( \mathbf{t}_{k,i} \times \mathbf{n}_{k,i,0} \big) \Big]. \tag{3.11}$$

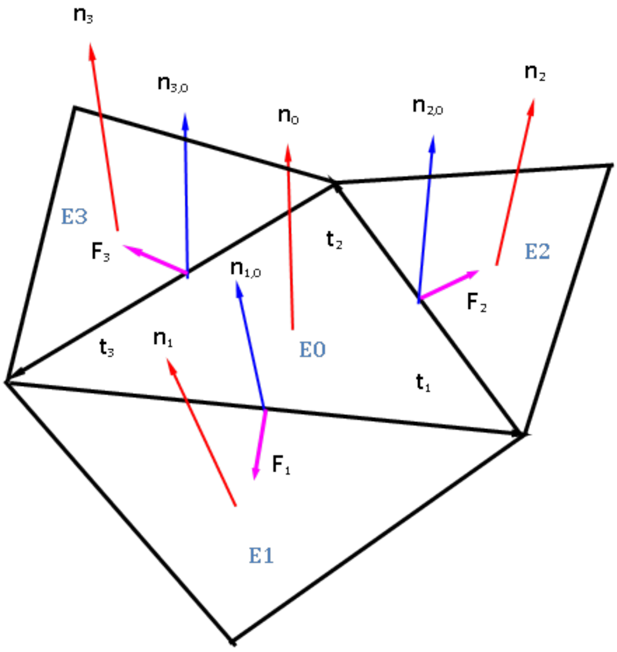

Figure 3.2: The surface tension forces ($\mathbf{F}_1$, $\mathbf{F}_2$ and $\mathbf{F}_3$) exerted on a central surface element ($E_0$) by the neighbouring elements ($E_1$, $E_2$ and $E_3$). Here $\mathbf{n}_1$, $\mathbf{n}_2$ and $\mathbf{n}_3$ represent the normal of element $E_1$, $E_2$ and $E_3$, respectively, while $\mathbf{n}_{1,0}$, $\mathbf{n}_{2,0}$ and $\mathbf{n}_{3,0}$ is the normal on the three edges of element $E_0$, respectively. Further, $\mathbf{t}_1$, $\mathbf{t}_2$ and $\mathbf{t}_3$ indicate the three edge vectors of element $E_0$.

### 3.2.4 Evolving the interface

With the techniques introduced in the previous sections, the governing equations can be solved on a fixed background grid to obtain the flow field. An adaptive, unstructured triangular mesh (front markers) is used to represent the interface between the two fluid phases. The velocity $\mathbf{u}_\Gamma(\mathbf{x}_\Gamma, t)$ of these moving front markers may then be obtained by interpolation from the flow field on the background mesh. Subsequently, the front mesh points can be advected in a Lagrangian manner from a position $\mathbf{x}_\Gamma^n$ at the $n$-th time step to a position $\mathbf{x}_\Gamma^{n+1}$

at the $(n+1)$-th time step. Thus the front moves with the same velocity as the surrounding fluid, and the so-called no-slip condition of the interface is satisfied. In this thesis, the interpolation is carried out using the same distribution function as the one used for the transfer of fluid properties to the background grid, yielding front marker velocity of

$$\mathbf{u}_\Gamma(\mathbf{x}_\Gamma, t) = \int_{\Gamma(t)} \mathbf{u}(\mathbf{x}, t) D(\mathbf{x} - \mathbf{x}_\Gamma) dS. \tag{3.12}$$

We may now use the front marker velocity obtained in Equation (3.12) to predict how the front marker position change from time step $n$ to time step $n+1$:

$$\mathbf{x}_\Gamma^{n+1} = \mathbf{x}_\Gamma^n + \mathbf{u}_\Gamma^n \Delta t, \tag{3.13}$$

where $\Delta t$ is the chosen time step.

As the front marker points are advected, the mesh size and quality may consequently change. The resolution of the front mesh has a strong effect on the information exchange with the fixed background grid, which may eventually affect the accuracy of the simulation results. Therefore, it is of key importance that the front mesh has a more or less constant quality and uniform resolution throughout the duration of the simulation. In this study, the resolution of the triangular mesh for the 3D surface of the bubble is maintained more or less uniform through adaptation as the interface evolves.

### 3.2.5 Mesh adaptation: The front mesh

As two sets of mesh are applied in the current front tracking method, the resolution of both the front mesh and the background mesh near the front plays an important role in resolving the interfacial physics of the multiphase flow. From physical principles it is known that fluid particles on the bubble interface will move downwards along the surface towards the bottom of the bubble as it rises. In the front tracking simulation, the mesh points on the bubble interface also move in a similar pattern. As a result, the mesh on the upper part of the bubble becomes coarser. On the other hand, the mesh at the lower part of the bubble becomes increasingly dense. The top front mesh in Figure 3.3 shows an example of a uniform mesh quality at initial time $t = 0$ before the bubble has started rising, whereas the bottom left and bottom right front mesh shows the same bubble after it has risen for a while, without and with mesh adaptation, respectively. It is obvious from the bottom left front mesh that the accuracy will be affected when the mesh on the top is too coarse, and that the dense fine mesh at the bottom of the bubble will consume excessive computing power without much benefit in accuracy. Thus, the front mesh adaptation as shown in the bottom right of Figure 3.3 is essential to ensure the accuracy and efficiency of the simulation. In this aspect, three basic operations are adopted to adapt the front mesh, namely edge swap, edge split and edge deletion. For long edges, the edge swap operation as shown in Figure 3.4 (a). This is a simple and easy operation to improve the mesh quality. In the edge split operation as shown in Figure 3.4 (b), a new point is generated by surface fitting of the existing neighbouring mesh points. This new point is then inserted into the two associated meshes, and new and finer triangles are generated to replace the old ones. Thus edge split is important to refine the front mesh. For the deletion of short edges as shown in Figure 3.4 (c), the triangles associated with the short edge will be

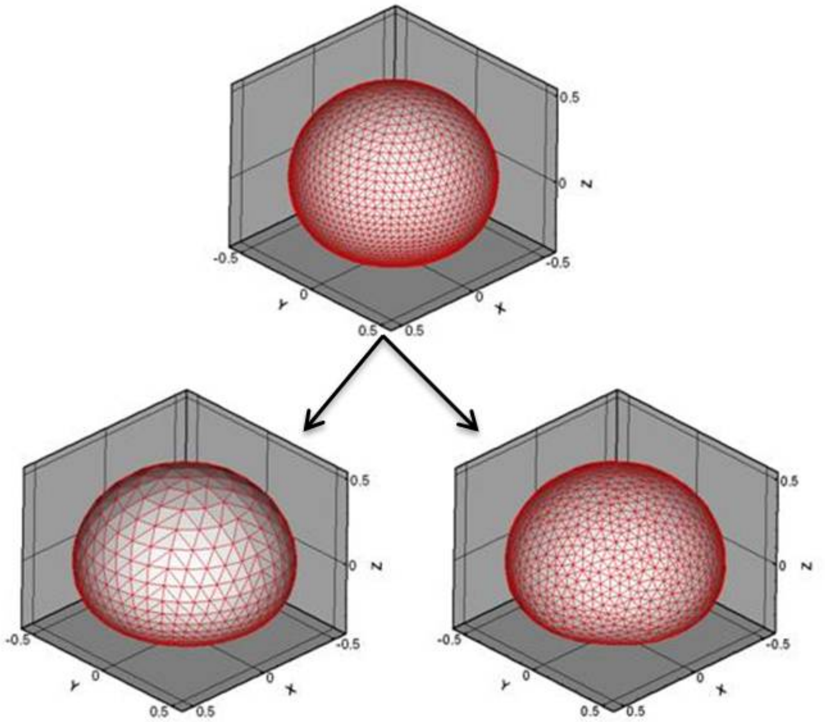

Figure 3.3: The front mesh representing a bubble at initial time $t = 0$ (top) and its evolution at a later time without (bottom left) and with (bottom right) mesh adaptation.

deleted, and the resulted gap will be sealed through merging the old nodes of the short edge. Hence, edge deletion is important to coarsen the front mesh. In addition, consistent checking of the mesh connectivity is also important to ensure the accuracy in calculating the surface tension.

### A note on volume conservation

As discussed in Chapter 2.2.2, the flow inside the gas bubble is assumed to be incompressible. A consequence of this assumption is that the volume of the bubble should remain constant throughout the simulations. Above we explained why it is necessary to adapt the front mesh, and it turns out that this adaptation may lead to changes in the volume enclosed by the mesh. At each time step any

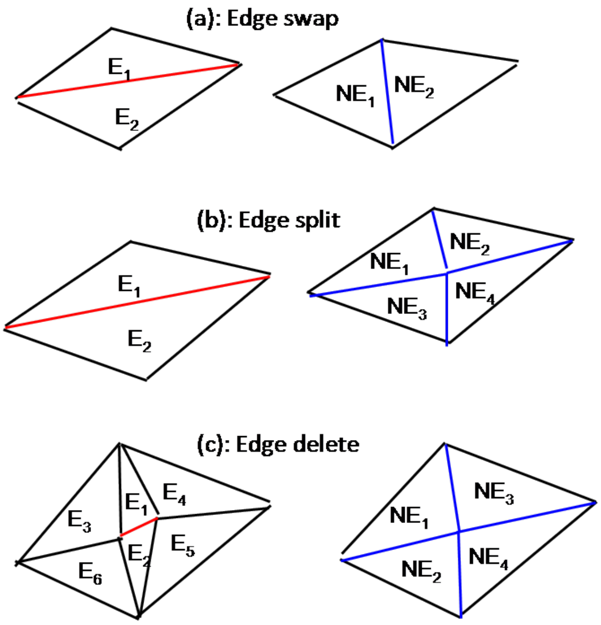

Figure 3.4: Basic operations: (a) edge swap, (b) edge split and (c) edge delete for the triangular mesh adaptation of the bubble surface mesh. E stands for existing element to be removed and NE for the new element to be created.

such volume change would be very small, but in simulations involving thousands of time steps, the accumulated volume change could be significant. To avoid a potential violation of the incompressibility assumption, volume conservation has therefore been enforced in a geometric manner by adjusting the position of the front markers every time the mesh has been adapted.

## 3.3 The flow solver: Modified SIMPLE

### 3.3.1 A projection-correction solver

A projection method was used to solve the Navier-Stokes equations in the previous works of Tryggvason et al. [114]. They used a fixed, regular, staggered grid and discretized the momentum equations using a second-order central difference scheme for the spatial variables and explicit second-order time integration. In their method, the front is advected first, and followed by density update. Once the density is updated, the velocity can be computed in the following two steps. In the first step of the projection scheme, the effects of pressure are ignored in the momentum equation, and the flow velocity is projected as follows:

$$\frac{\rho^{n+1}\mathbf{u}^* - \rho^n\mathbf{u}^n}{\Delta t} = -\nabla \cdot \rho^n\mathbf{u}^n\mathbf{u}^n + \nabla \cdot \mu^n(\nabla\mathbf{u}^n + \nabla^T\mathbf{u}^n) + \mathbf{F}_{st}, \tag{3.14}$$

where $\mathbf{u}^*$ is an intermediate velocity field, $\Delta t$ is the time step size, and the superscripts $n$ and $n+1$ refer to the current and the next time step, respectively. Then a correction step is performed to include the pressure gradient:

$$\frac{\rho^{n+1}\mathbf{u}^{n+1} - \rho^{n+1}\mathbf{u}^*}{\Delta t} = -\nabla p. \tag{3.15}$$

With the incompressibility condition ($\nabla \cdot \mathbf{u}^{n+1}$), the pressure can be obtained by solving the following nonseparable elliptic Poisson equation:

$$\nabla\frac{1}{\rho^{n+1}} \cdot \nabla p = \frac{1}{\Delta t}\nabla \cdot \mathbf{u}^* \tag{3.16}$$

A number of difficulties have been reported in the literature while solving the above pressure equation. For example, an artificial boundary condition for the pressure has to be provided (See [39] and [62]), and a large density ratio may lead to a problem in convergence [114, 15].

Next we will introduce the well-developed SIMPLE algorithm to solve the one-fluid flow equations. Later on in Chapter 7 we shall introduce a relatively new sequential regularization formulation which is designed to avoid solving the pressure Poisson equation and thus has a great potential to overcome difficulties associated with the pressure equation.

### 3.3.2 A semi-implicit finite volume solver

In order to overcome the difficulties in solving the pressure equation (3.16), an alternative approach is implemented in the present work. Similar to that of Tryggvason et al. [114], we also use a fixed, regular, staggered grid, but discretize the momentum equations using a finite volume approach. As the front is advected explicitly, the fluid property field and surface tension are updated subsequently. Then, the coupling between flow velocity and pressure is updated by solving the momentum equations and continuity equation using SIMPLE scheme [86] instead of projection method. The simulation process is more robust even in case of large density ratio because of the semi-implicit solving approach:

$$\frac{\rho^{n+1}\mathbf{u}^{n+1} - \rho^{n}\mathbf{u}^{n}}{\Delta t} + \nabla\cdot\rho^{n+1}\mathbf{u}^{n+1}\mathbf{u}^{n+1} = \nabla p^{n+1} + \nabla\cdot\mu^{n+1}(\nabla\mathbf{u}^{n+1} + \nabla^{T}\mathbf{u}^{n+1}) + \mathbf{F}_{st}^{n+1}. \tag{3.17}$$

Similar to the conventional approach, the above equation can be solved iteratively, together with the continuity equation, using the volume flux conserved SIMPLE algorithm [86]. In a multi-fluid system, due to the density jump over the interface, the traditional mass flux conservation in the control volume crossing the front interface is not valid. Instead, the volume flux conservation is adopted here to modify the SIMPLE algorithm. The divergence of velocity field over the whole solution domain will be kept at zero, as long as both liquid and gas can be reasonably treated as incompressible fluids. Based on this assumption, SIMPLE algorithm is used to calculate the correction value of pressure and velocity after solving the momentum equation as describe in the following.

### Discretization

In discretized form, the momentum equation can be expressed as the following:

$$a_p \mathbf{U}_p^* = \sum a_{n,p} \mathbf{U}_{n,p}^* + S_p - B \nabla P_p^* \tag{3.18}$$

in which $n$ indicates the neighbouring point surrounding the centre point $p$, and the coefficient $a_{n,p}$ involves the flow properties of convection, diffusion and geometrical property of the control volume. $S_p$ refers the source term and $B$ the coefficient for the pressure gradient term. Details about these coefficients can be obtained in the work of Patankar [86]. Improved pressure field ($P_p^{**}$) and velocity field ($\mathbf{U}_p^{**}$) can be obtained by adding the correction terms ($\mathbf{U}_p^{'}$, $P_p^{'}$) to the values used in Equation (3.18) based on calculation of $\mathbf{U}_p^*$,

$$\mathbf{U}_p^{**} = \mathbf{U}_p^* + \mathbf{U}_p^{'}, \tag{3.19}$$

or assumption of $P_p^*$,

$$\mathbf{P}_p^{**} = \mathbf{P}_p^* + \mathbf{P}_p^{'}. \tag{3.20}$$

Substituting the above equation into Equation (3.18), we have the relationship about correction velocity ($\mathbf{U}_p^{'}$) and correction pressure ($P_p^{'}$) as follows:

$$\mathbf{U}_p^{'} = \sum a_{n,p}\mathbf{U}_{n,p}^{'}/a_p - B/a_p \cdot \nabla P_p^{'}. \tag{3.21}$$

Applying incompressible fluid condition to the improved velocity field ($\nabla \cdot \mathbf{U}_p^{**} = 0$), the velocity correction ($\mathbf{U}^{'}$) should satisfy the following condition:

$$\nabla \cdot \mathbf{U}^{'} = -\nabla \cdot \mathbf{U}^{*}. \tag{3.22}$$

By taking divergence to the both sides of Equation (3.21), ignoring the first term (with high order) on the right hand side of Equation (3.21) and substituting it into Equation (3.22), the pressure correction can be obtained by solving the following equation:

$$\nabla \cdot [(B/a_p)\nabla P^{'}] = \nabla \cdot \mathbf{U}^{*}. \tag{3.23}$$

Based on the pressure correction, the velocity correction can also be derived according to Equation (3.21). The updated velocity and pressure are then used as the guessed field for the next iteration for solving the momentum Equation (3.18). Such iterations will be repeated until the convergence of both momentum and continuity equations. Compared with the projection method, the SIMPLE algorithm avoids directly solving the pressure equation, which enhances the numerical robustness for the cases with large density/viscosity jumps across the two-fluid interface [21].

### 3.3.3 Mesh adaptation: The background grid

In Section 3.2.5 we studied the resolution of the front mesh. Accordingly, the resolution of the background mesh also plays an important role in capturing the flow behaviour  particularly so in the vicinity of the interface. If the background mesh resolution is too low, then the detailed flow dynamics will not be captured reasonably well, resulting in unreliable and inaccurate simulations. Therefore, it is desirable to have relatively high-resolution grids, particularly near the interface, while coarse grids may be used away from the interface. This is achieved in our model by the use of the block-based adaptive mesh refinement (AMR) tool PARAMESH [70]. In this study, the refining and coarsening of the grid blocks is based on whether there exists a bubble front within the blocks. An example of the block-wise Cartesian mesh refinement generated by PARAMESH is showed in Figure 3.5. It can be seen that fine background grids are located in the vicinity of the bubble, while coarser background grids are applied in regions further away from the bubble front. This feature makes it more efficient to solve the governing equations and to capture the flow physics near the interface accurately. Another excellent feature of PARAMESH is that all blocks of Cartesian grid points have the same structure at any level of refinement. Hence, once the flow solver is developed for one grid block, it can be easily applied to all other blocks independent of the level of refinement. In addition, the different blocks can be distributed to different CPUs in an MPI parallel environment, which speed up the problem solving cycle.

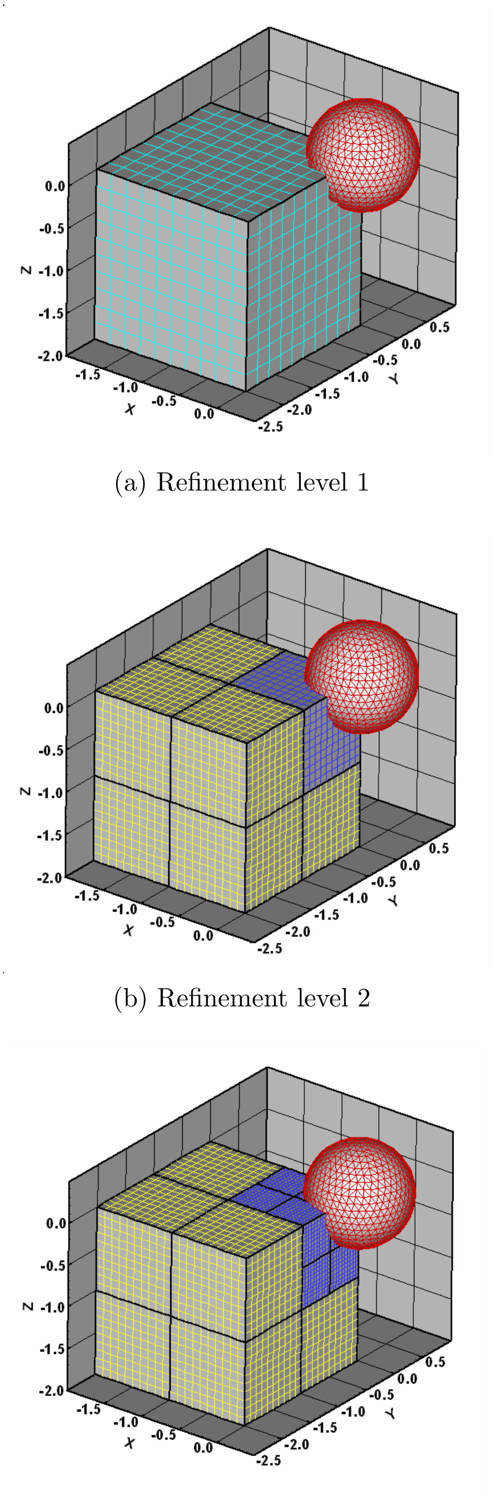

(a) Refinement level 1

(b) Refinement level 2

(c) Refinement level 3

Figure 3.5: Illustration of the successive refinement levels in PARAMESH.

## 3.4 Moving reference frame

In many applications of multiphase flow it is often desirable to study the long-term behaviour and evolution of the moving interface between the fluids. In such applications the front may move a considerable distance, and the study of the rise path of an air bubble in water is a typical example. The computational domain must then be correspondingly large to accommodate such extensive movement. However, in a three-dimensional model with a high-resolution grid, a large computational domain is computationally very expensive. Computational cost may therefore limit the domain size and thus also long-time simulations. To remedy this problem, we have therefore incorporated a moving reference frame into our numerical algorithm. The idea is to move the reference frame together with the front such that the front (e.g. a bubble) remains more or less fixed in the computational domain. The size of the computational domain may then be chosen independently of the duration of the simulation, and this will in turn reduce the computational cost significantly. As a result, we may carry out long-time simulations of moving interface problems which could not have been done in a stationary reference frame. Figure 3.6 illustrates a moving reference frame. There, the frame $XY$ stands for a stationary reference frame and the frame $X'Y'$ for a moving reference frame. The positions of a monitoring point in the frames $XY$ and $X'Y'$ are represented as $x_p$ and $x'_p$, respectively, which are correlated with the position of the moving reference frame ($\mathbf{x}_m$) according to (3.24). The velocity of the monitoring point $P$ is $\mathbf{u}(\mathbf{x}, t)$ in the frame $XY$ and $\mathbf{u}'(\mathbf{x}', t)$ in the moving frame $X'Y'$, and the velocity of the moving frame is $\mathbf{u}_m(t)$. The following correlations can be obtained:

$$\mathbf{x}_p = \mathbf{x}_m + \mathbf{x}'_p \tag{3.24}$$

and

$$\mathbf{u}(\mathbf{x},t) = \mathbf{u}_m(t) + \mathbf{u}'(\mathbf{x}',t). \tag{3.25}$$

Allowing translational, but not rotational, movement of the frame in the present study, the following is the updated governing flow equations in the moving reference frame:

$$\nabla' \cdot \mathbf{u}' = 0 \tag{3.26}$$

and

$$\begin{gathered}\frac{\partial(\rho\mathbf{u}')}{\partial t} + \nabla' \cdot \rho\mathbf{u}'\mathbf{u}' + \rho\frac{d\mathbf{u}_m}{dt} = \\ -\nabla' p + \frac{1}{Ar}\nabla' \cdot \left(\mu(\nabla'\mathbf{u}' + (\nabla'\mathbf{u}')^T)\right) + \frac{1}{Bo}\int_\Gamma \kappa\mathbf{n}\delta(\mathbf{x}' - \mathbf{x}'_\Gamma)dS + (\rho - 1)\mathbf{g}.\end{gathered} \tag{3.27}$$

The moving front will generally be accelerating and so will the moving reference frame. Thus the frame of reference in which we solve the governing equations is no longer an inertial frame, and we must therefore modify the momentum equations to take into account the acceleration of the frame. In addition, according to (3.25), when the governing equations are solved in a moving reference frame, the velocity condition on the boundary ($\mathbf{x}'_B$) should be modified as $\mathbf{u}'(\mathbf{x}_B,t) = \mathbf{u}(\mathbf{x}_B,t) - \mathbf{u}_m(t)$.

Notice the additional term on the left-hand side of the momentum equation (3.27), $\frac{d\mathbf{u}_m}{dt}$, which denotes the acceleration $\mathbf{a}_m$ of the moving reference frame. We aim to choose $\mathbf{a}_m$ so that the rising bubble remains as fixed as possible in the moving frame, i.e. ideally the acceleration of the frame is equal to the acceleration of the bubble. The bubble acceleration is of course unknown, so we need to approximate this acceleration at each time step. We shall adopt the prediction as presented by Rusche [96], namely

$$\mathbf{a}_m^{n+1} = -\frac{\Delta \mathbf{u}_m^{n+1}}{(\Delta t)^n}, \tag{3.28}$$

where

$$\Delta \mathbf{u}_m^{n+1} = \lambda_1 \frac{\mathbf{x}_d^0 - \mathbf{x}_d^n}{(\Delta t)^n} - \lambda_2 \frac{\mathbf{x}_d^n - \mathbf{x}_d^{n-1}}{(\Delta t)^n}. \tag{3.29}$$

Here $\mathbf{x}_d^j$ is the position of the bubble mass centre relative to the moving frame at time step $j$, $(\Delta t)^n = t^n - t^{n-1}$, and $\lambda_1$ and $\lambda_2$ are appropriate under-relaxation factors. It was found that $\lambda_1 = \lambda_2 = 0.1$ gave good results in the present study.

## 3.5 Boundary conditions

One aim of the current study is to investigate the dynamics of a single bubble rising in liquid. This system has been extensively studied experimentally, and can therefore be used as a good study case to validate the current numerical modelling algorithm. In experiments, the bubble rises in a liquid tank which

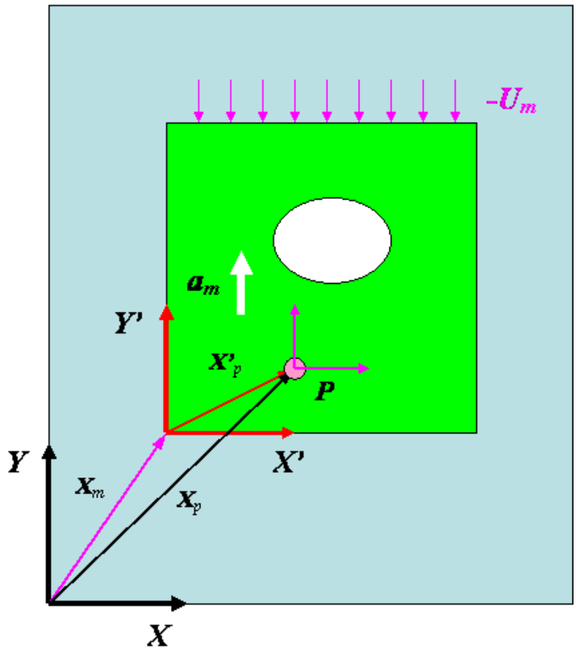

Figure 3.6: Schematic diagram showing the implementation of a moving reference frame attached to the rising bubble. Frame $XY$ represents a stationary frame and Frame $X_0Y_0$ a moving frame. P is a point associated with the bubble surface where the moving frame is to be attached.

is typically much larger than the bubble size (about 20 bubble diameters) to minimize the tank wall effect. In the present simulations, the side length of the cubic simulation domain is selected to be eight times the bubble diameter, which is large enough to neglect wall containment effects as concluded in the domain size sensitivity analysis presented in Section 4.2.1. In addition, free slip boundary conditions are applied on the four vertical walls of the cubic simulation domain. A pressure inlet boundary condition is applied on the top of the computational domain. Here the pressure is fixed to be zero, the vertical velocity component has a zero normal gradient, and the horizontal velocity components are assumed to be zero. A velocity outflow boundary condition is applied on the bottom of the simulation domain, where the flow velocity is set to be the moving speed of the reference frame and zero normal gradient condition is applied to the pressure. The moving speed for the stationary reference frame is set to be zero, while the speed for the moving reference frame can be calculated according to the method introduced in the previous section.

## 3.6 Summary: Solution procedure

We may now summarize the main steps in advancing the solution from one time step to the next as follows:

1. The velocity of the front marker points, $\mathbf{u}_\Gamma^n$, is calculated through interpolation of the fluid velocity field $\mathbf{u}^n$ according to (3.12).

2. The front is advected to its new position $\mathbf{x}_\Gamma^{n+1}$ by using the interface velocity $\mathbf{u}_\Gamma^n$ found in step (1), see (3.13). The front elements are then subject to examination for adaptation and topological change. Meanwhile, volume conservation is enforced.

3. The indicator function $I^{n+1}(\mathbf{x}_\Gamma^{n+1})$ is computed based on the interface position $\mathbf{x}_\Gamma^{n+1}$. This is done by solving the Poisson problem in (3.4) with the discrete delta distribution from (3.5). Subsequently, the distribution of the density $\rho^{n+1}$, the viscosity $\mu^{n+1}$ and the surface tension $\mathbf{F}_\sigma^{n+1}$ is updated on the flow solver grid points.

4. We find the velocity field $\mathbf{u}^{n+1}$ and the pressure $p^{n+1}$ by solving the mass continuity and momentum equations using a modified version of the SIMPLE algorithm. Appropriate boundary conditions are applied according to Section 3.5

5. Repeat steps (1) - (4) to advance the solution to time $t^{n+2}$.

# Chapter 4

# Front Tracking for Two-Phase Flow: Numerical Results

## 4.1 Introduction

In this chapter we thoroughly test the implementation of the numerical methodology presented in Chapter 3 for solving the mathematical model represented by Equations (3.26) - (3.29). A detailed sensitivity analysis of the computational set-up is presented in Section 4.2 where the impact of the domain size, mesh resolution and moving reference frame is scrutinized. Additionally, the validity of the mathematical model itself is assessed in Section 4.3 through comparisons of numerical predictions with available experimental data on gas bubbles rising in liquids. Data considered include terminal bubble rise velocities and bubble shapes, and validation results for the common air-water system are also presented.

## 4.2 Sensitivity analysis

A large number of sensitivity studies were carried out to gain insight into how some key parameters impacts on the numerical solution. These results and subsequent conclusions will be presented in this section.

### 4.2.1 Domain size

Extensive experiments have been performed in the past to study the rise and deformation of single gas bubbles in quiescent liquids. Often these experiments have been conducted in large containers with a size of at least 20 bubble diameters in each spatial direction to avoid wall containment effects [6]. In this study, we intend to validate simulation results against such experiments. To achieve this, the computational domain should also be rather large to avoid any significant effects caused by the wall confinement. On the other hand, if the domain is chosen too large, excessive computing time would be required to complete the simulations. To analyse the influence of the domain size, a number of numerical tests were run with cubic domain sizes ranging from two to 12 bubble diameters in each of the spatial dimensions. The grid resolution was kept constant and corresponded to approximately 20 cells inside the bubble in each direction. All computations were carried out in a moving reference frame. The terminal rise velocity and the terminal bubble shape were used to assess the wall confinement effects for various domain sizes. The aim of this particular sensitivity analysis was to find the smallest possible computational domain in which wall containment effects have negligible impact on the bubble terminal velocity and shape.

Figure 4.1 presents the simulation results of the terminal bubble shape and the rise velocity using different domain sizes under the conditions of $Bo = 243.0$, $Ar = 15.24$, $\rho_L/\rho_G = 1000$ and $\mu_L/\mu_G = 100$ (Case A4). There is a notable change in the terminal bubble shape and rise velocity as the domain size is increased from two to six bubble diameters. When the domain size is increased beyond six bubble diameters, no significant change in the simulation results is observed. Moreover, it is noted that the wall confinement has a strong effect on the terminal velocity for small domain sizes from two to six bubble diameters. However, the change in terminal velocity is only around 1% when increasing the computational domain size from eight to 10 bubble diameters in each spatial dimension.

Terminal bubble shapes and the rise velocities for different domain sizes were also studied in a regime with higher rise velocities: $Bo = 115.0$, $Ar = 134.6$, $\rho_L/\rho_G = 1000$ and $\mu_L/\mu_G = 100$ (Case A5). The results are presented in Figure 4.2, and the trends are similar to those seen for case A4. To the naked eye there is negligible change in the bubble shapes, though the terminal velocity does clearly change. The change in velocity is only about 1% when the cubic domain size goes beyond eight bubble diameters.

Based on these observations for two different flow regimes, we conclude that a domain size with side length of eight bubble diameters should be sufficient in our simulations. This conclusion is in good agreement with experimental results by Krishna et al. [59] who indicate that wall effects on a rising bubble is negligible when the diameter of the cylindrical liquid container is eight bubble diameters or larger. In addition, our results are consistent with the results reported in a numerical study of wall effects on gas bubbles rising in liquid by Mukundakrishnan et al. [81].

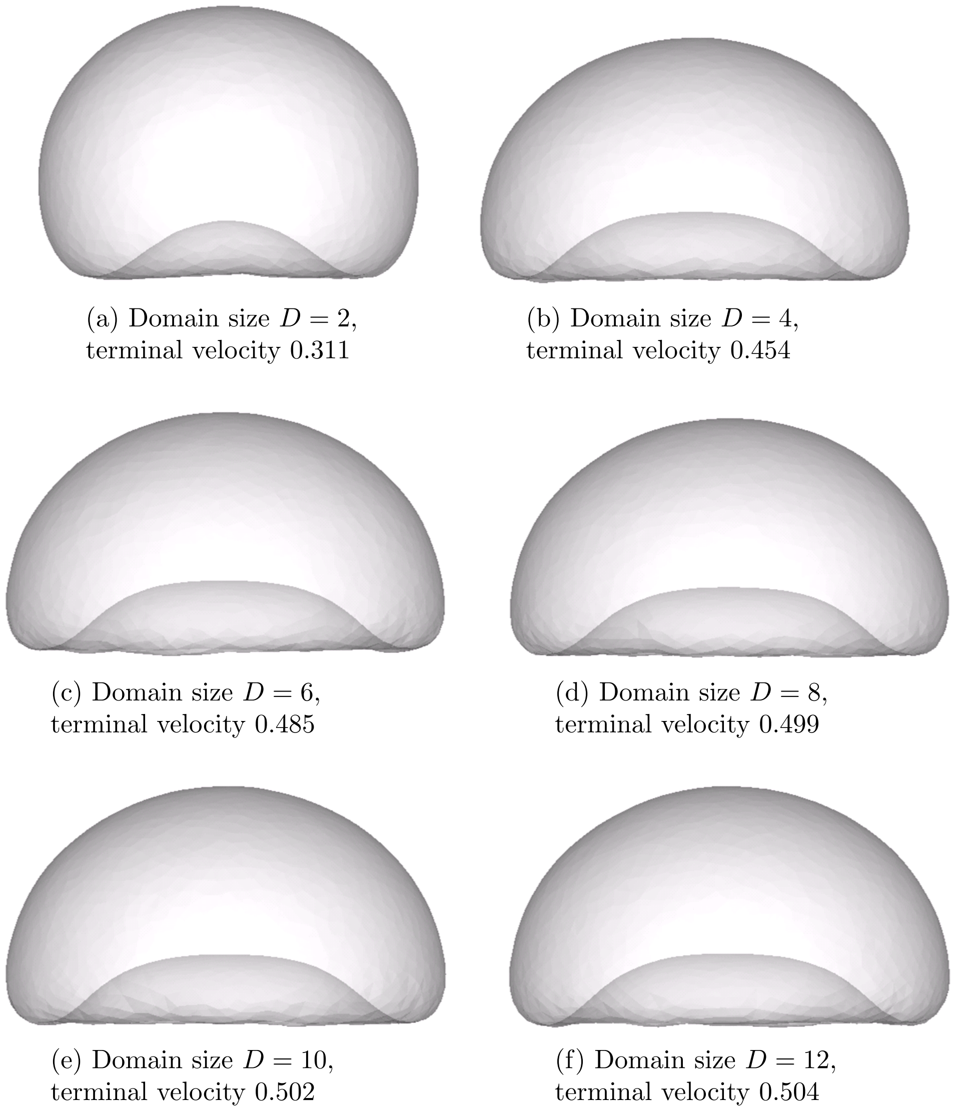

(a) Domain size $D = 2$, terminal velocity 0.311

(b) Domain size $D = 4$, terminal velocity 0.454

(c) Domain size $D = 6$, terminal velocity 0.485

(d) Domain size $D = 8$, terminal velocity 0.499

(e) Domain size $D = 10$, terminal velocity 0.502

(f) Domain size $D = 12$, terminal velocity 0.504

Figure 4.1: Sensitivity analysis about the effects of the computational domain size on terminal bubble shape and terminal rise velocity for the case A4.

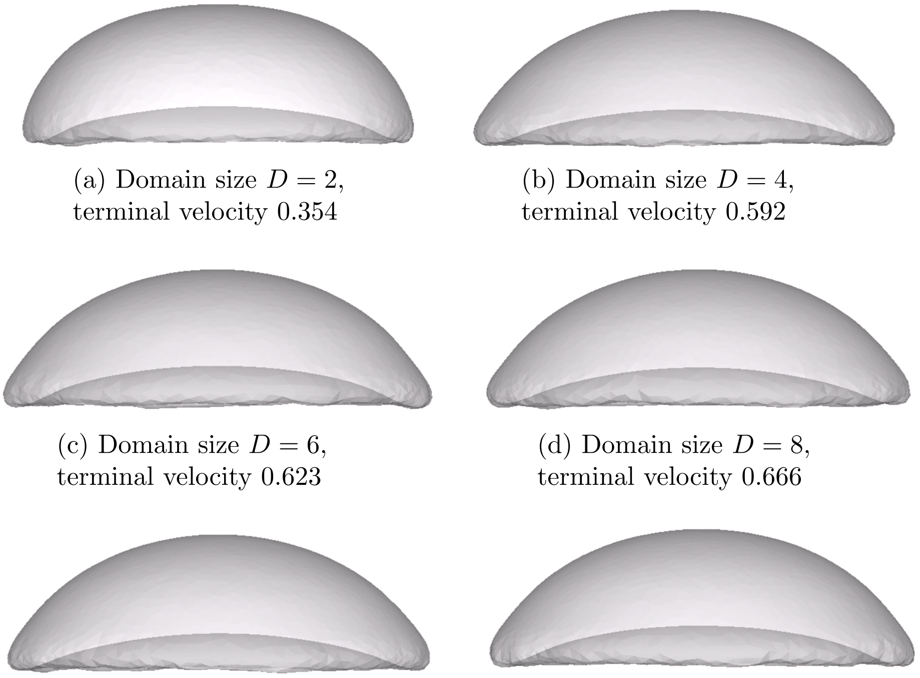

(a) Domain size $D = 2$, terminal velocity 0.354

(b) Domain size $D = 4$, terminal velocity 0.592

(c) Domain size $D = 6$, terminal velocity 0.623

(d) Domain size $D = 8$, terminal velocity 0.666

(e) Domain size $D = 10$, terminal velocity 0.658

(f) Domain size $D = 12$, terminal velocity 0.650

Figure 4.2: Sensitivity analysis about the effects of the computational domain size on terminal bubble shape and terminal rise velocity for the case A5.

### 4.2.2 Mesh resolution

In Section 3.3.3 we discussed the importance of having a high-resolution background grid to ensure that the flow physics is captured accurately, particularly near the interface. At the same time, higher grid resolution means more grid points and obviously increased computational demands both in terms of memory and CPU time. These demands may indeed be significant as we are dealing with a fully three-dimensional problem, and it is therefore desirable to obtain a compromise between grid resolution and computational cost. In this section we therefore carry out a study to find the minimum resolution needed such that increasing the resolution beyond this does not affect results significantly.

In our methodology, the flow equations are solved on a Cartesian background grid through the use of PARAMESH [70], a block-based adaptive mesh refinement tool discussed in Section 3.3.3. The computational domain is divided into a number of blocks in each spatial direction as illustrated in Figure 3.5. Each block consists of a certain number of grid cells in each direction, and the governing equations are discretized and solved numerically on these grid cells. For a computational domain of fixed size, there are therefore two ways to change the grid resolution using PARAMESH: either by changing the number of blocks, which is determined by the maximum number of refinement levels, or by changing the number of cells in each block. In this grid sensitivity analysis we kept the maximum refinement level (blocks) fixed and changed the number of cells in each block. All simulations were done in a moving, cubic computational domain with side length equal to eight bubble diameters using equal grid spacing in each of the spatial directions.

Similar to the sensitivity analysis carried out for the domain size in Section 4.2.1, we again use terminal bubble shape and velocity to assess the computational results. The first set of grid sensitivity analysis results can be found in Figure 4.3 under the conditions of $Bo = 243.0$, $Ar = 15.24$, $\rho_L/\rho_G = 1000$ and $\mu_L/\mu_G = 100$ (Case A4). It is noted that the terminal bubble velocity is highly sensitive to the mesh resolution up until 16 cells per bubble in each space direction. However, increasing the number of cells from 16 to 20 yields less than 1% change in terminal velocity. The terminal bubble shape also has a very strong dependence on the grid resolution – especially when the grid resolution is relatively low. In fact, we can even see a slight change in shape when increasing the number of cells per bubble diameter from 16 to 20. However, increasing the number of cells per bubble diameter further to 32 does not lead to any visually detectable change in the bubble shape.

Results from a higher velocity regime are given in Figure 4.4, the conditions being $Bo = 115.0$, $Ar = 134.6$, $\rho_L/\rho_G = 1000$ and $\mu_L/\mu_G = 100$ (Case A5). The trends are practically identical to those found in the lower velocity regime: Increasing the grid resolution beyond 16 cells per bubble in each space direction gives practically no change in the terminal velocity, while the bubble shape changes marginally when increasing the number of cells from 16 to 20. No changes are observed by increasing the number of cells to 32.

Based on the above studies one may conclude that it would be sufficient to use a resolution of 16 cells per bubble diameter in each space direction for our simulations of bubbles rising in viscous liquids. However, since minor bubble shape changes were observed when increasing the resolution to 20 cells, we have chosen this higher resolution to be the default value for our computations.

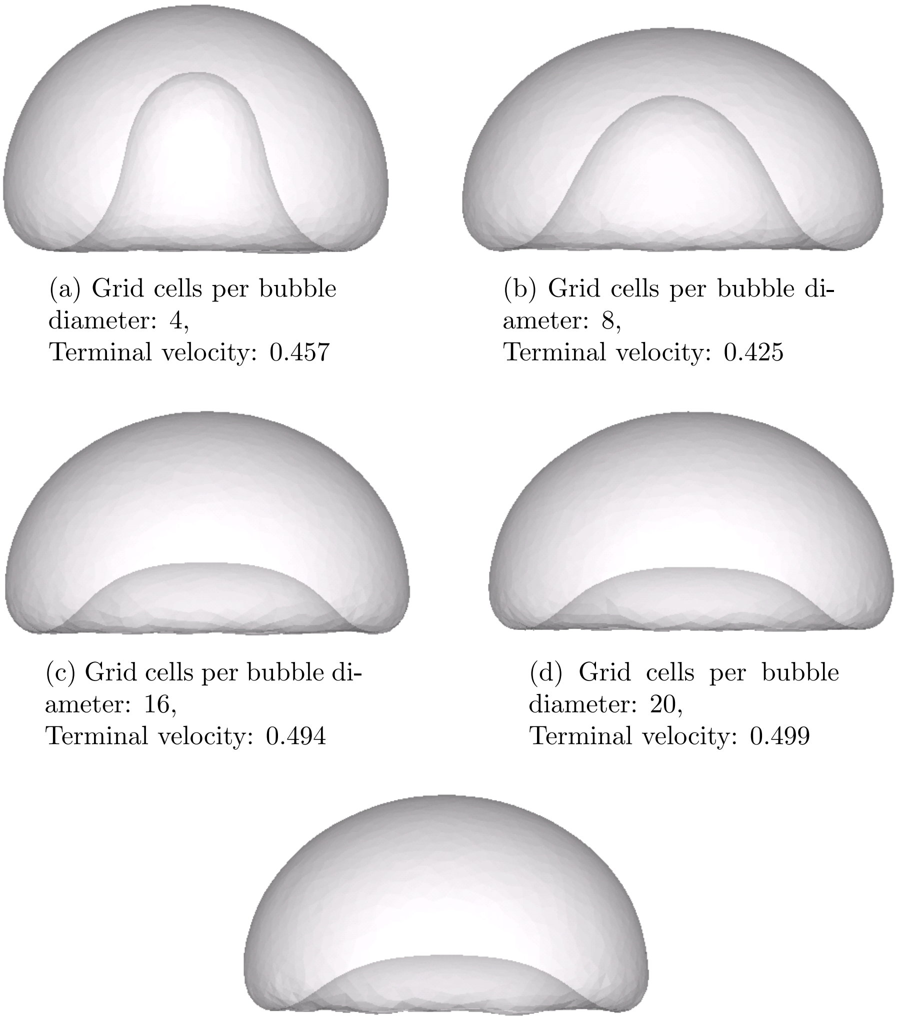

(a) Grid cells per bubble diameter: 4,
Terminal velocity: 0.457

(b) Grid cells per bubble diameter: 8,
Terminal velocity: 0.425

(c) Grid cells per bubble diameter: 16,
Terminal velocity: 0.494

(d) Grid cells per bubble diameter: 20,
Terminal velocity: 0.499

(e) Grid cells per bubble diameter: 32,
Terminal velocity: 0.504

Figure 4.3: Sensitivity analysis about the effects of the background grid resolution on terminal bubble shape and terminal rise velocity for the case A4.

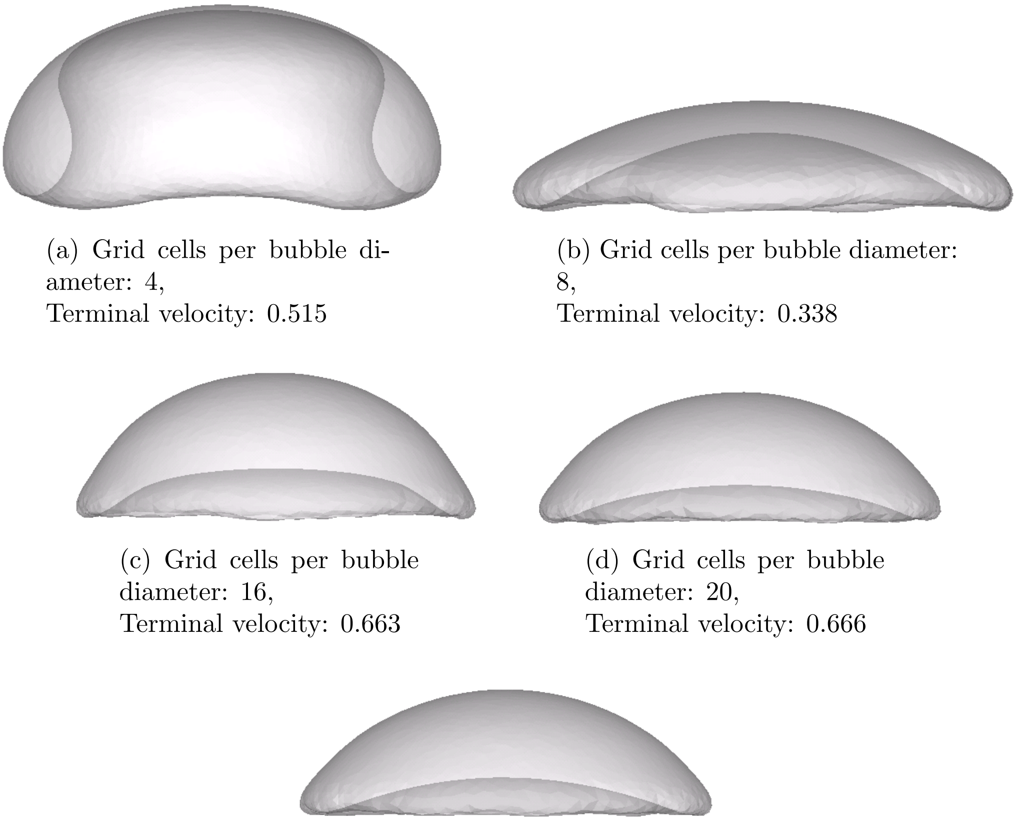

(a) Grid cells per bubble diameter: 4,
Terminal velocity: 0.515

(b) Grid cells per bubble diameter: 8,
Terminal velocity: 0.338

(c) Grid cells per bubble diameter: 16,
Terminal velocity: 0.663

(d) Grid cells per bubble diameter: 20,
Terminal velocity: 0.666

(e) Grid cells per bubble diameter: 32,
Terminal velocity: 0.663

Figure 4.4: Sensitivity analysis about the effects of the background grid resolution on terminal bubble shape and terminal rise velocity for the case A5.

### 4.2.3 Moving reference frame

A moving reference frame (MRF) is introduced in our numerical solution algorithm as detailed in Section 3.4. This was done to enable long-time simulations of both single bubbles rising and two bubbles interacting, and it is important to evaluate and verify the accuracy and impact of using a moving as opposed to a stationary reference frame (SRF). For this purpose, simulation results for Case A5 obtained in a stationary and in a moving reference frame are compared.

The bubble shapes predicted in both stationary and moving frames at different time steps are shown in Figure 4.5. A closer look at this figure shows that the differences between the shapes obtained in the two reference frames are negligible. A comparison of the velocity profiles of bubbles rising in a stationary and a moving reference frame is shown in Figure 4.6, and they are in reasonable agreement. Note that the velocity of the moving frame itself has been added to the bubble rise velocity obtained in the moving reference frame to enable a direct comparison with the bubble rise velocity in the stationary frame. In addition to comparing bulk behaviour of rising bubbles, we would also like to compare the detailed flow patterns around the bubbles. A comparison of the streamlines predicted in a stationary and a moving frame can be found in Figure 4.7. Since one frame is at rest and one is moving, comparing streamlines would only be sensible if we modify the velocity in one of the frames to account for the different velocities of the frames. Here we have chosen to subtract the velocity of the moving reference frame from the velocity field computed in the stationary frame before comparison. It can be seen from Figure 4.7 that an excellent agreement of the streamline patterns in the stationary and the moving frame is obtained. Furthermore, pressure distributions around the rising bubbles predicted in a stationary and a moving frame are compared in Figure 4.8, and again the results agree well.

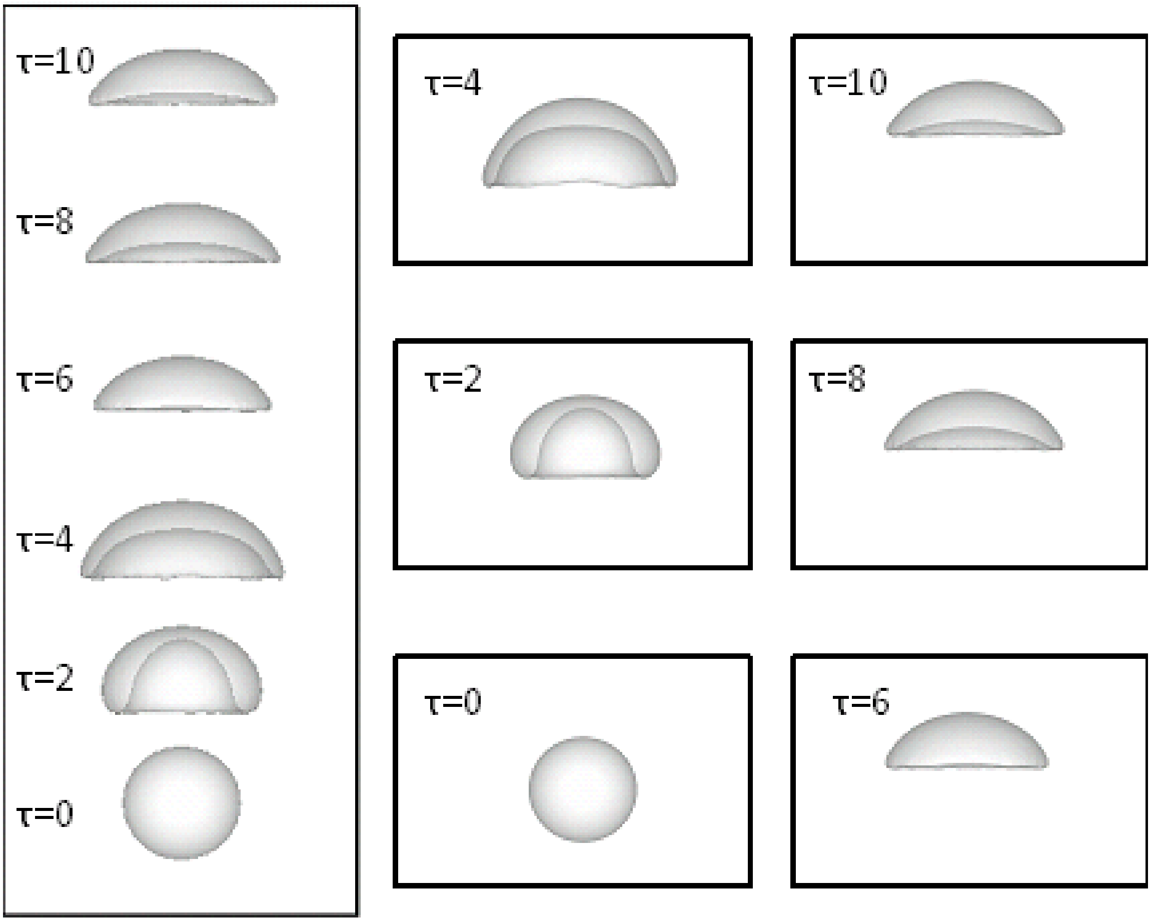

Figure 4.5: A comparison of the evolution of the predicted bubble shapes in a stationary (the left-most column) and a moving reference frame (the two right-most columns) for the case A5.

Based on the various tests and comparisons of different flow characteristics carried out as described above, we can conclude that the use of a moving reference frame yields numerical results in reasonable agreement to those obtained in a stationary reference frame.

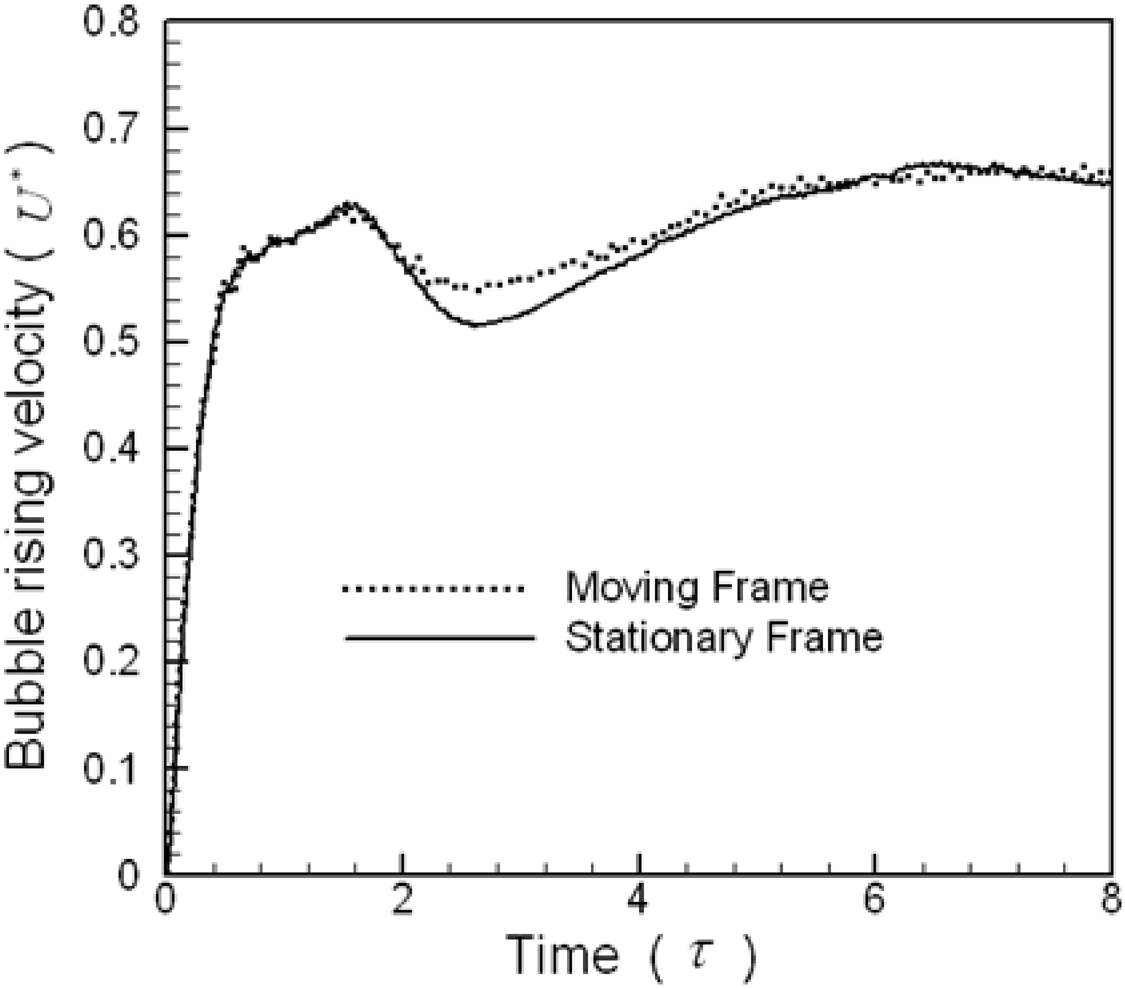

Figure 4.6: A comparison of the transient rise velocity of the bubble in a stationary and a moving reference frame for the case A5.

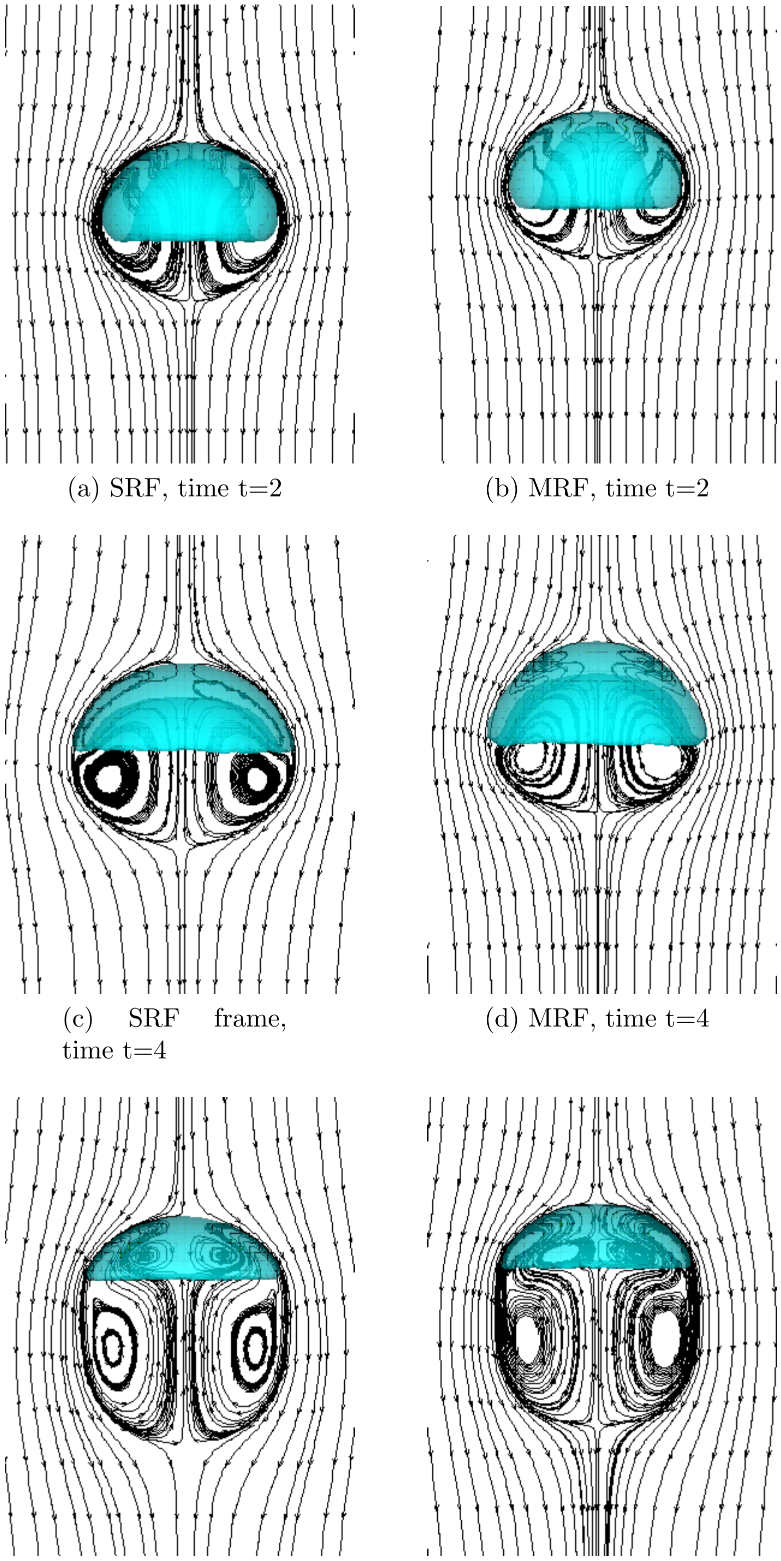

(a) SRF, time t=2

(b) MRF, time t=2

(c) SRF frame, time t=4

(d) MRF, time t=4

(e) SRF, time t=6

(f) MRF, time t=6

Figure 4.7: Continued on the next page.

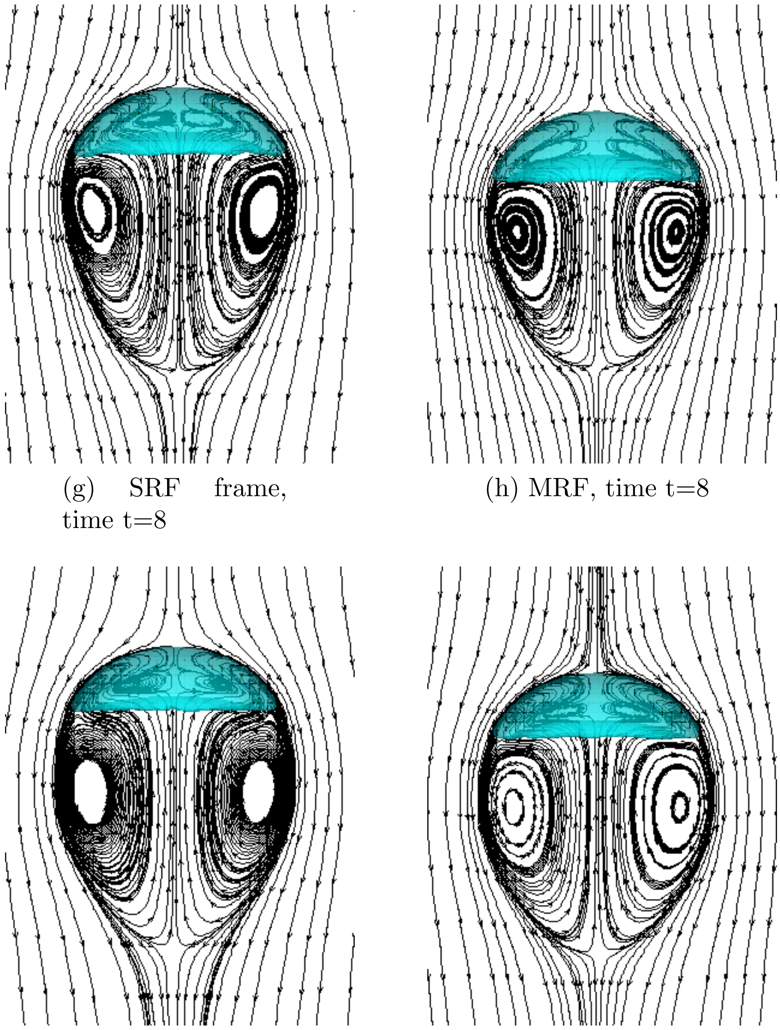

(g) SRF frame, time t=8

(h) MRF, time t=8

(i) SRF frame, time t=10

(j) MRF, time t=10

Figure 4.7: Comparison of flow streamlines near the bubble at different times computed in a stationary and a moving frame for case A5. To enable a direct comparison, the velocity of the moving frame was subtracted from the velocity computed in the stationary frame.

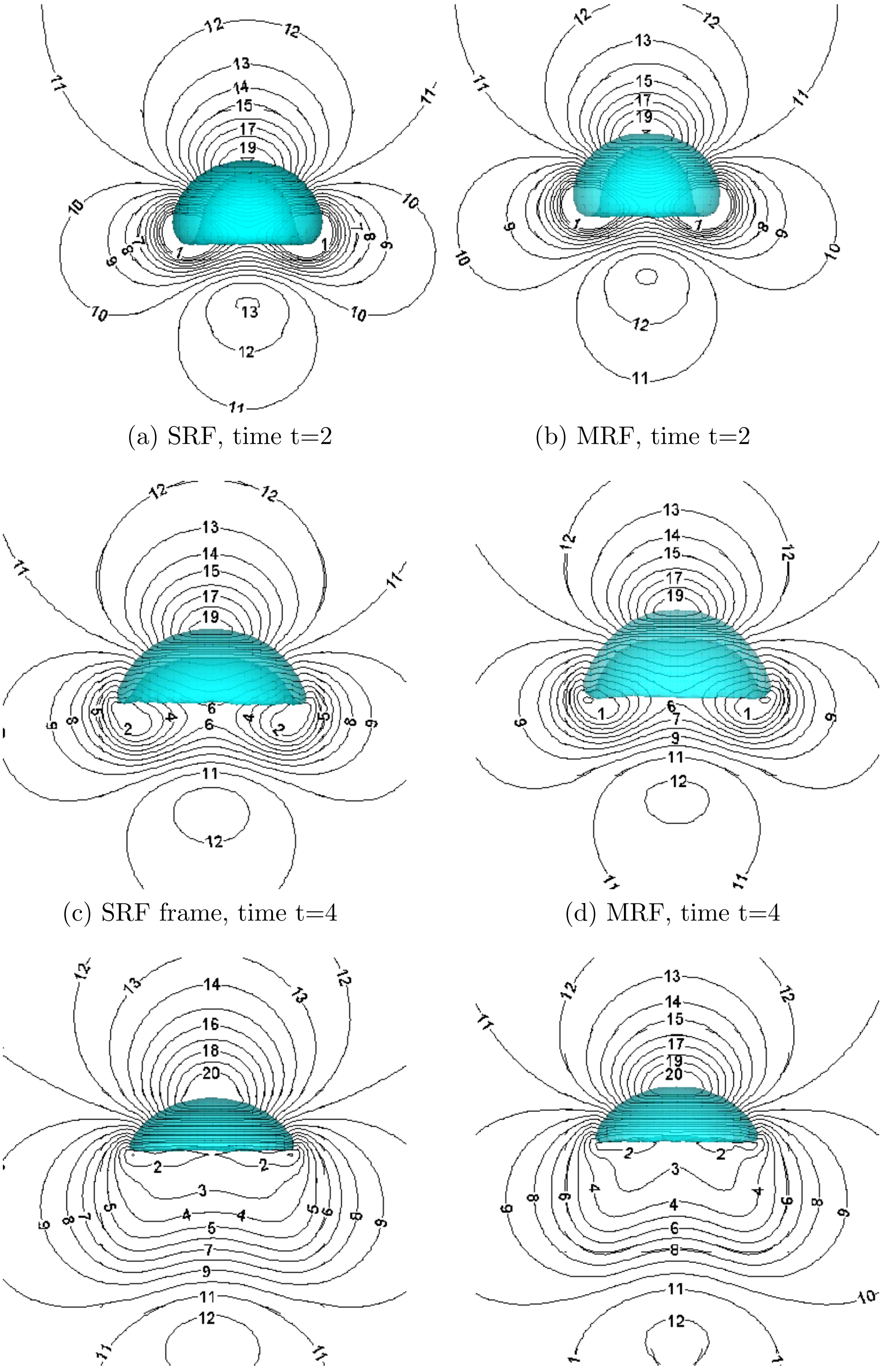

(a) SRF, time t=2

(b) MRF, time t=2

(c) SRF frame, time t=4

(d) MRF, time t=4

(e) SRF, time t=6

(f) MRF, time t=6

Figure 4.8: Continued on the next page.

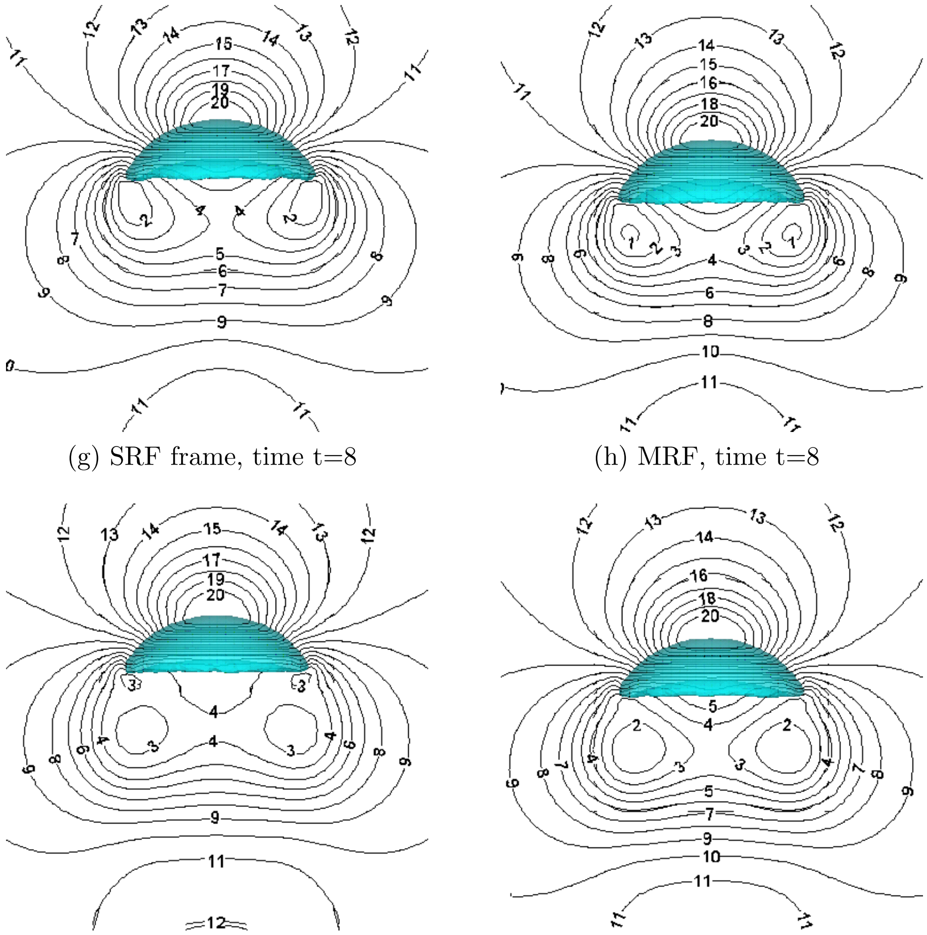

(g) SRF frame, time t=8

(h) MRF, time t=8

(i) SRF frame, time t=10

(j) MRF, time t=10

Figure 4.8: Comparison of pressure distributions near the bubble at different times computed in a stationary and a moving frame for case A5.

## 4.3 Validation

In Section 4.2 we carried out sensitivity analysis and decided on what would be an adequate size of the computational domain and grid resolution. We also saw that the use of a moving reference frame gave results as expected. The next natural step to increase our confidence in the adopted mathematical model and the numerical method and its implementation would be to compare numerical results with actual experimental data.

The problem of a single gas bubble rising in a viscous liquid has been widely used as a typical validation case for the development of new numerical methods for multiphase flow [21, 115, 116]. Due to numerous experimental and numerical studies in the past, the physical understanding of the bubble rise behaviour in liquid has been well-established in some flow regimes, e.g. regimes with lower Reynolds and Bond numbers [23, 6]. However, due to the complexity of multiphase flow physics and the difficulties in both experiments and simulations, the behaviour of a rising bubble with high Reynolds number is still not understood well [80, 58]. In this work, we validate our model through comparing computational results of a single bubble rising with experimental results [6] in aspects of both bubble shapes and terminal velocities. In addition, we apply the 3D model to simulate air bubbles rising in water, and we compare the terminal velocities and shapes of the bubbles predicted in our simulations with experimental data within a large range of initial bubble diameters: from 0.5 mm to 30 mm. There have been few numerical studies on this topic except some recent ones [29, 58]. However, since the process of air bubbles rising in water is so common in both our daily life and industrial applications, a better understanding of this system is of great importance.

### 4.3.1 Rising bubbles: Shapes and terminal velocities

Bhaga and Weber presented experimental data of shapes and terminal velocities of bubbles rising in viscous liquids in their popular paper from 1981 [6]. They carried out numerous experiments and correlated the terminal rise velocity to shape regimes, and we will here compare their results with predictions obtained by our numerical method.

In Figure 4.9, we compare observed and predicted terminal bubble shapes for a range of Reynolds and Bond numbers, and the results agree very well. Table 4.1 shows a comparison of the corresponding terminal rise velocities in terms of Reynolds numbers, and again there is generally good agreement between experiments and our numerical predictions.

However, it is noted that the relative deviation in Case A2 is a little bit high as the numerically predicted Reynolds number is about 20% lower than that observed in experiments. This deviation may be due to the low rise velocity where the relative error will be high even for small absolute errors though there is no change in the simulation accuracy. Another possible reason is that the hindrance effect due to the limited size of the domain becomes significant at low Reynolds numbers. Since free slip boundary is applied in the current simulation, the computation of a single bubble rising corresponds rigorously to the rise of a homogeneous swarm of bubbles. Sangani [101] calculated the sedimentation velocity of a swarm of spherical bubbles at low Reynolds numbers for a complete range of volume fractions. As the cubic simulation domain has a side length equal to eight bubble diameters (8D), the volume fraction of the bubble swarm is $\alpha = 4/3 \cdot \pi(D/2)^3/(8D)^3 \approx 1.023 \times 10^{-3}$. In this case $\alpha \ll 1$, and the velocity of the bubble swarm is given by $U_{swarm}/U_s = 1 - 1.76\frac{K+2/3}{K+1}\alpha^{1/3}$, where $U_S$ is the velocity of the single bubble, and $K = \mu_G/\mu_L$. Calculations then yield

| Test Case | Experiments | | Simulations | |
|---|---|---|---|---|
| | Test Conditions | Observed terminal bubble shape | Predicted terminal bubble shape | Modeling conditions and predicted terminal velocity |
| A2 | E = 17.7<br>M = 711<br>Re = 0.232 | 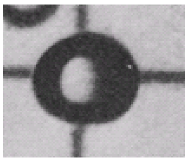 | 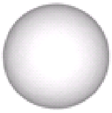 | Bo = 17.7<br>Ar = 1.671<br>Fr = 0.109 |
| A3 | E = 32.2<br>M = 8.2·10$^{-4}$<br>Re = 55.3 | 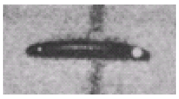 | 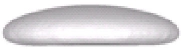 | Bo = 32.2<br>Ar = 79.88<br>Fr = 0.686 |
| A4 | E = 243<br>M = 266<br>Re = 7.77 | 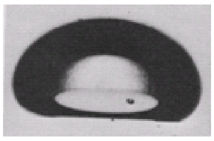 | 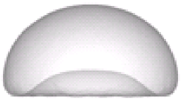 | Bo = 243<br>Ar = 15.24<br>Fr = 0.499 |
| A5 | E = 115<br>M =<br>4.63·10$^{-3}$<br>Re = 94.0 | 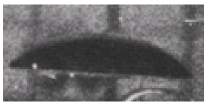 | 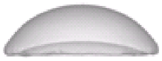 | Bo = 115<br>Ar = 134.6<br>Fr = 0.666 |
| A7 | E = 339<br>M = 43.1<br>Re = 18.3 | 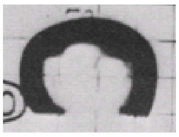 | 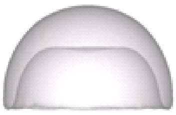 | Bo = 339<br>Ar = 30.83<br>Fr = 0.576 |

Figure 4.9: Comparison of terminal bubble shapes observed in experiments [6] and predicted by numerical simulations.

$U_{swarm}/U_s \approx 0.88$ as $K = 0.01$ for Case A2. Hence, due to the limited size of the computational domain, the estimated bubble swarm velocity is about 12% lower than the velocity of a single free rising bubble. This could explain the discrepancy observed for Case A2.

In conclusion, the numerical predictions, which cover regimes $1.671 < Ar < 134.6$ and $17.7 < Bo < 339$, match very well with the experiments presented in [6].

| Test cases | Experimental $Re$ | $Ar$ | $Fr$ | $Re_c$ | Deviation [%] |
|---|---|---|---|---|---|
| A2 | 0.232 | 1.671 | 0.109 | 0.182 | 21.49 |
| A3 | 55.3 | 79.88 | 0.686 | 54.798 | 0.91 |
| A4 | 7.77 | 15.24 | 0.499 | 7.605 | 2.13 |
| A5 | 94.0 | 134.6 | 0.666 | 89.644 | 4.63 |
| A7 | 18.3 | 30.83 | 0.576 | 17.758 | 2.96 |

Table 4.1: Comparison of terminal rise velocities found in experiments [6] and predicted by numerical simulations.

### 4.3.2 The air-water system

One extremely common system that has proven notoriously challenging to study both experimentally and numerically is that of air bubbles rising in water. We here present our results for a wide range of initial bubble diameters and compare terminal rise velocities with experimental results.

Air bubbles rising in water are common in many industrial processes. Examples in chemical engineering include bubble columns, loop reactors, agitated stirred reactors, flotation, and fermentation reactors. For the design of efficient two-phase reactors, detailed knowledge of bubble sizes and shapes, slip velocities, internal circulations, swarm behaviours, bubble induced turbulence and mixing, and bubble size distributions (including coalescence and breakup) is of fundamental importance. In such industrial applications, bubbles often have non-spherical and even dynamic shapes as well as asymmetric wake structures.

Extensive experimental studies have been performed to study air bubbles rising in water, e.g. by Clift et al. [23] and Tomiyama et al. [111]. Their measurements of the terminal rise velocity of air bubbles in water are presented in Figure 4.10 as a function of the bubble size. It is found that the measured terminal velocity vary significantly (bifurcation) when the bubble diameter is greater than 0.5 mm and smaller than 10 mm. Traditionally this variation has been explained by the presence of surfactants of varying degree [23], but more

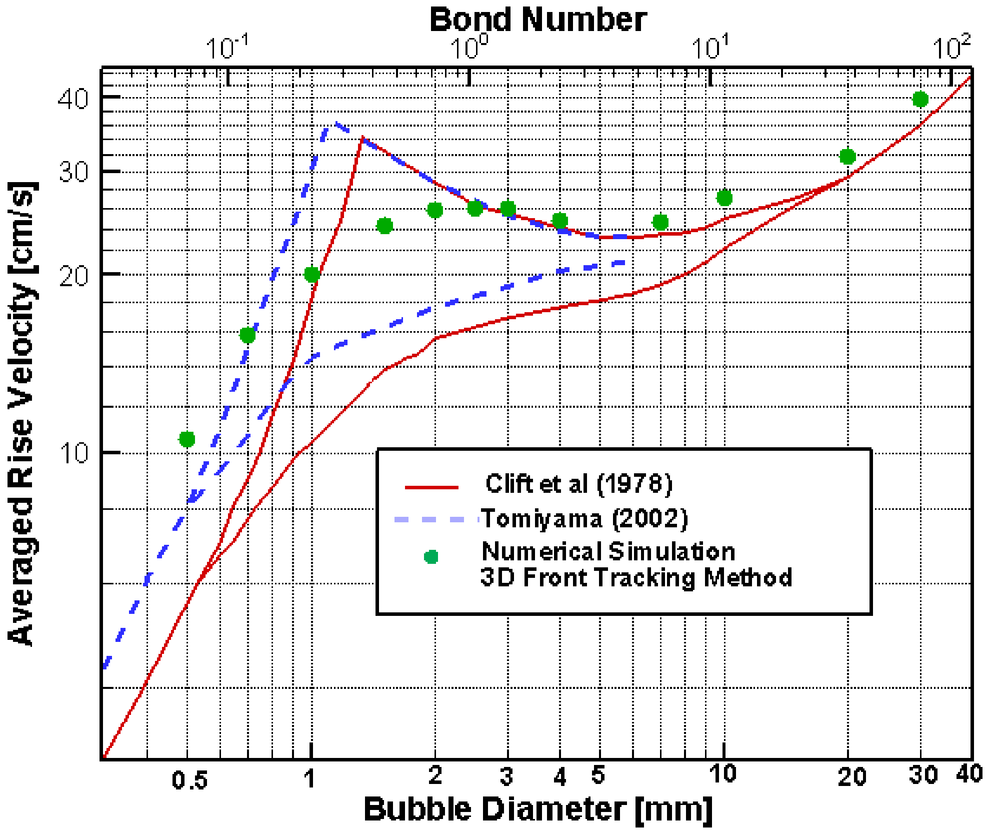

Figure 4.10: Comparison of the terminal velocity of air bubbles of different size rising in water predicted in the present simulations and observed in experiments by Clift et al. [23] and Tomiyama et al. [111].

recently both Wu and Gharib [119] and Tomiyama et al. [111] attributed this variation to the manner in which the bubbles were initially generated. The issue continues to be a matter of discussion – refer to Yang et al. [120].

Due to difficulties in measuring the physical properties on the bubble, a fundamental understanding of the system of a single bubble rising in high Reynolds number regimes is not well established. With the recent rapid increase in computing power, numerical simulations of two-phase flows based on continuum mechanics models with moving free interfaces have become feasible and proved extremely useful for a better understanding of fundamental processes and phenomena. However, numerical modelling of the multi-fluid system of air bubbles rising in water is still quite challenging due to the large density ratio of water to air, the low liquid viscosity of water, high Reynolds numbers, and large bubble deformations. Koebe et al. [58] started early trials of 3D direct numerical simulation of air bubbles rising in water at high Reynolds number using a volume of fluid (VOF) method. They studied bubbles with diameters from 0.5 to 15 mm, and their numerical predictions on the terminal rise velocity of the bubbles agree reasonably with experimental data. However, they introduced some initial white noise in the simulations, which may introduce non-physical perturbations to the simulation system. The recent work by Dijkhuizen et al. [29] reported their trial on simulation of single air bubbles rising in initially quiescent pure water using both a 3D front tracking method and a 2D VOF method for bubble diameters ranging from 1 to 8 mm. The calculated terminal rise velocities by the 3D front tracking method are quite close to the experimental observations by Tomiyama et al. [111], but they over-predicted the velocity for bubble diameters larger than 3 mm.

In this thesis, we use the front tracking method with features of mesh adaptation and moving reference frame, allowing a finer mesh in the region of the bubble surface. Consequently, better accuracy is obtained in the current simulations. We simulate a single air bubble rising in initially quiescent pure water with bubble diameters ranging from 0.5 to 30 mm. The numerically predicted rise velocities of the bubbles agree well with the upper bound of the experimental measurements by Tomiyama et al. [111] within the whole range of different bubble sizes as shown in Figure 4.10. The variation of terminal shapes for rising bubbles with initial bubble diameters ranging from 0.5 to 30 mm is shown in Figure 4.11, and the results are in reasonable agreement with experimental observations [23]. When the bubble diameter is in the range from 2.0 to 10

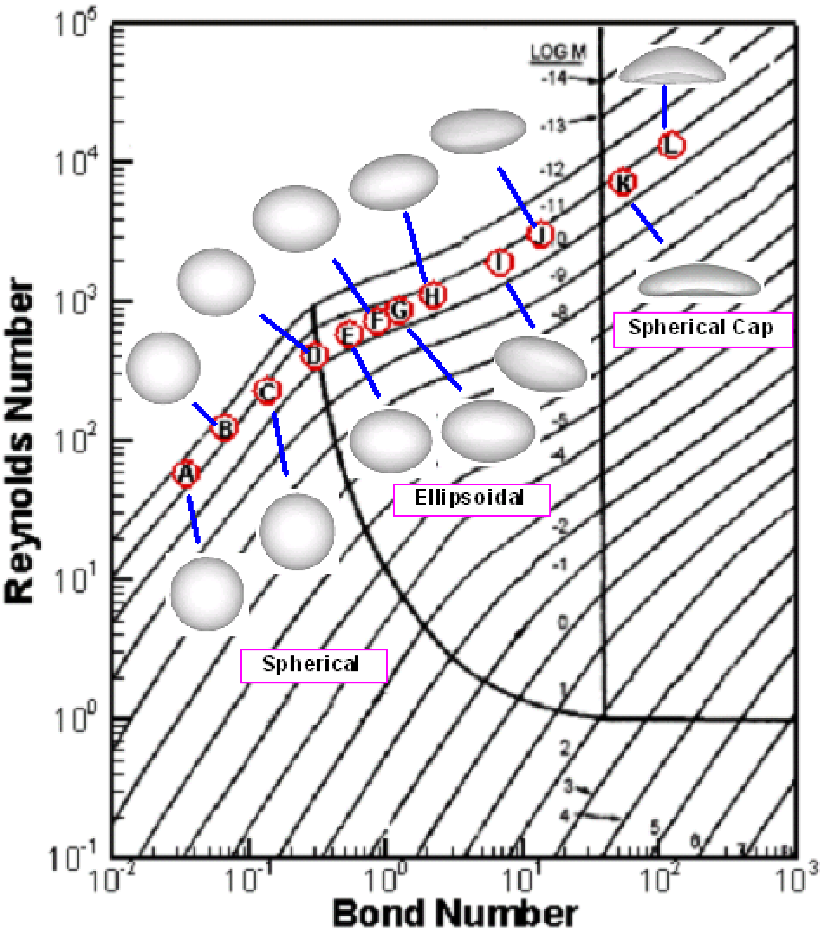

Figure 4.11: Numerically predicted terminal shapes of air bubbles rising in water for bubble diameters ranging from 0.5 to 30 mm. The points A to L correspond to the bubble size of 0.5, 0.7, 1.0, 1.5, 2.0, 2.5, 3.0, 4.0, 7.0, 10.0, 20.0 and 30.0 mm, respectively.

mm, simulation results predict an oscillation of the bubble rise velocity and the bubble shape. The terminal bubble rise velocity is therefore calculated through averaging the instantaneous rise velocity over a period of time. Since we assume the initial bubble shape to be spherical and the surface tension coefficient to be constant, the bifurcation of the bubble rise velocity is not revealed in the current simulation. However, this is an interesting topic to be explored in the future.

# Chapter 5

# Path Instability of Rising Bubbles

## 5.1 Introduction

It is a well-known fact that gas bubbles rising in still liquids do not generally rise along a rectilinear path - they may follow a zigzag or spiral trajectory. In Prosperetti's delightful paper ”Bubbles” [92] from 2004, the author refers to this rise behaviour as *Leonardo's paradox*. This is to acknowledge that Leonardo da Vinci's (1452 – 1519) observations and comments on this fascinating phenomenon may have been the first ones of a scientific nature. An in-depth review of studies on the path instability of rising bubbles was given by Magnaudet and Eames in 2000 [71]. They concluded that despite extensive theoretical [98, 43, 75], experimental [4, 66, 31, 69] and, to a certain extent, numerical [97, 7, 54] investigations in the area, the understanding of Leonardo's paradox is not satisfactory. They attributed the reasons for this short-coming to the possible complex interactions between the following phenomena:

1. Surfactants. Experiments have shown that impurities in the liquid can have dramatic impact on the flow dynamics, but it is difficult to measure or characterize the degree of surfactants.

2. Shape oscillations. For certain bubble sizes, their shapes have been observed to oscillate periodically, influencing the rise behaviour.

3. Wake instabilities. It is not well-understood how the complex wake structures and vortex shedding influences the rise path and vice-versa.

Efforts to gain further insight into Leonardo's paradox are ongoing, and significant progress has been made since the review paper of Magnaudet and Eames in year 2000. Recent experimental contributions include [32, 25, 78, 119, 80, 117], and numerical investigations are also becoming increasingly important. Indeed, the main purpose of this Chapter is to apply our front tracking methodology to reproduce Leonardo's paradox and to shed some light on the mechanisms behind it - see Section 5.2.2. However, we first review other direct numerical simulation attempts on bubble path instability in Section 5.2.1.

## 5.2 Numerical simulation of bubble path instability

### 5.2.1 Review of existing numerical results

The purpose of this Section is to provide an overview of literature presenting direct numerical simulation results for path instability of gas bubbles rising in liquids.

In 1989 Meiron [75] presented numerical results for bubbles rising in an axisymmetric inviscid flow. A stability analysis was carried out similar to what was done by Hartunian and Sears [43] in 1957. Meiron's main conclusion was that the interaction between hydrodynamic pressure forces and surface tension alone does not lead to linear instability of the bubble path; a conclusion contradicting the previous findings of Hartunian and Sears.

A common assumption in past numerical investigations is that the rising bubble has a fixed spherical shape, even though it is well-known that bubble deformation usually becomes important for increasing Reynolds numbers. Blanco and Magnaudet [7] (1995) relaxed the assumption of a fixed *spherical* shape and allowed for a fixed *oblate ellipsoidal* shape, a shape more appropriate to for example millimetric air bubbles in water. However, the fixed shape assumption remained, and, like Meiron, their investigations also assumed axisymmetry.

In 2002 Mougin and Magnaudet [78, 79] then solved the unsteady three-dimensional Navier-Stokes equations in a fluid domain surrounding a fixed-shape spheroidal bubble. They coupled these fluid equations with force and torque balances that determine the motion of the bubble to see if such a system would be sufficient to reproduce path instability. For certain values of the control parameters, results did indeed show both zigzagging and spiralling bubbles, indicating that small-scale bubble deformation is not necessary for path instability to occur.

A similar system was studied extensively by Jenny and co-workers [53] (2004), though they studied a sphere, both falling and rising, rather than a spheroid. Detailed numerical results were presented for the instability patterns of the sphere, with particular focus on the transition between different flow regimes in terms of density ratios and Galileo numbers.

In 2006 Mougin and Magnaudet [80] published an in-depth analysis of the forces and torques acting on a bubble as it rises. These results were based on processing the numerical results previously obtained in 2002 [78, 79], and they make observations on the influence of the wake and draw conclusions on what forces are important in determining the bubble path. A year later, Magnaudet and Mougin then presented further numerical results [72], this time considering the simpler system of unsteady three-dimensional flow around a fixed, oblate spheroidal bubble. A sensitivity analysis of the bubble aspect ratio was carried out, and a threshold value at which the flow becomes unstable was identified. Further analysis of the relationship between the wake structure and flow instability was also carried out.

In a recent paper [93], Rabha and Buwa presented fully three-dimensional results for air bubbles rising in both water (low viscosity) and a water-glycerol solution (high viscosity) using a VOF method. There was no assumption about a fixed-shape bubble as in previous studies by Mougin, Magnaudet and Jenny. However, the authors did not use adaptive grid refinement nor a moving reference frame, and due to computational constraints they therefore had to impose a velocity field rather than letting the bubbles rise freely due to buoyancy.

### 5.2.2 Our numerical results

The review above illustrates how direct numerical simulation methods have been contributing to an improved understanding of Leonardo's paradox. However, the review also reveals that one or more of the following simplifying assumptions have traditionally been enforced in DNS studies:

- Inviscid flow: Inviscid theory does not predict path instability and is therefore not an apt assumption in this context.

- Axisymmetric flow: For increasing Reynolds number, the axisymmetric wake breaks up and fully three-dimensional computations are needed.
- Fixed-shape bubbles: In reality the shape of the bubble evolves, and in certain flow regimes the shape will oscillate. Such oscillations, in particular, are important for the overall movement of the bubble and cannot be ignored if a realistic bubble path is to be predicted.

In this Section we have applied our front tracking methodology to simulate the rise behaviour of a single, initially stationary and spherical bubble in a quiescent viscous liquid without any of the above simplifying assumptions. The aim is to demonstrate the capabilities of the current simulation algorithm by reproducing path instability, and we also make some observations on the relationship between rise patterns and associated wake structures.

### A zigzag path

Figure 5.1 shows that the numerically predicted rise path of the bubble is a zigzag when the simulation parameters are set to be $Bo = 10.0$, $Ar = 1000$, $\frac{\rho_L}{\rho_G} = 1000$ and $\frac{\mu_L}{\mu_G} = 100$. A 3D view of the trajectory of the bubble mass centre is shown in Figure 5.1a. It clearly illustrates that the bubble moves laterally as it starts rising. When the velocity of the bubble becomes high enough, the bubble starts following a zigzag path. A projection of the trajectory into the $XY$-plane is shown in Figure 5.1b, revealing that the zigzag path lies almost entirely in one single vertical plane.

The mechanism of the bubble rising behaviour is closely related to the wake structure created by the rising bubble. A careful study of the wake structure of the rising bubble is illustrated in Figure 5.2, which shows the flow stream line path around the bubble and a pressure contour in the bubble wake. When the rise velocity is low, a bubble wake with symmetric, closed recirculation rings is formed, and a low pressure zone is generated at the recirculation centre as shown in Figure 5.2a. As the rise velocity increases, the flow instability is amplified and the bubble wake starts detaching from one side of the bubble bottom as shown in Figure 5.2b. Due to the asymmetric wake structure, the drag and lift forces acting on the bubble will now also become unbalanced, and the bubble is tilted as shown in Figure 5.2b. As the bubble speed increases further, the bubble wake becomes more asymmetric and the bubble tilting becomes more pronounced. As a result, the recirculation ring of the bubble wake is fully broken on one side as shown in Figure 5.2c, whereas the opposite end of the recirculation ring starts attaching itself to one bottom side of the oblate bubble as shown in Figure 5.2d. Consequently, two open recirculation rings attached to one side of the bubble bottom are finally formed, resulting in tilting and lateral movement of the bubble. The lateral movement makes the open recirculation rings in the bubble wake switch from one side to the other side of the bubble bottom as shown in Figures 5.2e and 5.2f. This oscillation of the two open wake recirculation rings from one side of the bubble bottom to the other causes the bubble to rise on a zigzag path.

### A spiral path

The parameters that produced a zigzagging bubble rise path were $Bo = 10.0$, $Ar = 1000$, $\frac{\rho_L}{\rho_G} = 1000$ and $\frac{\mu_L}{\mu_G} = 100$. Increasing the Bond number to $Bo = 32.0$ and the Archimedes number to $Ar = 1400$, the numerical predictions now show a spiral pattern for the bubble rise path as pictured in Figure 5.3. A 3D view of the trajectory of the mass centre of the bubble is shown in Figure 5.3a, and it clearly reveals that the bubble starts rising in a spiral with increasing radius

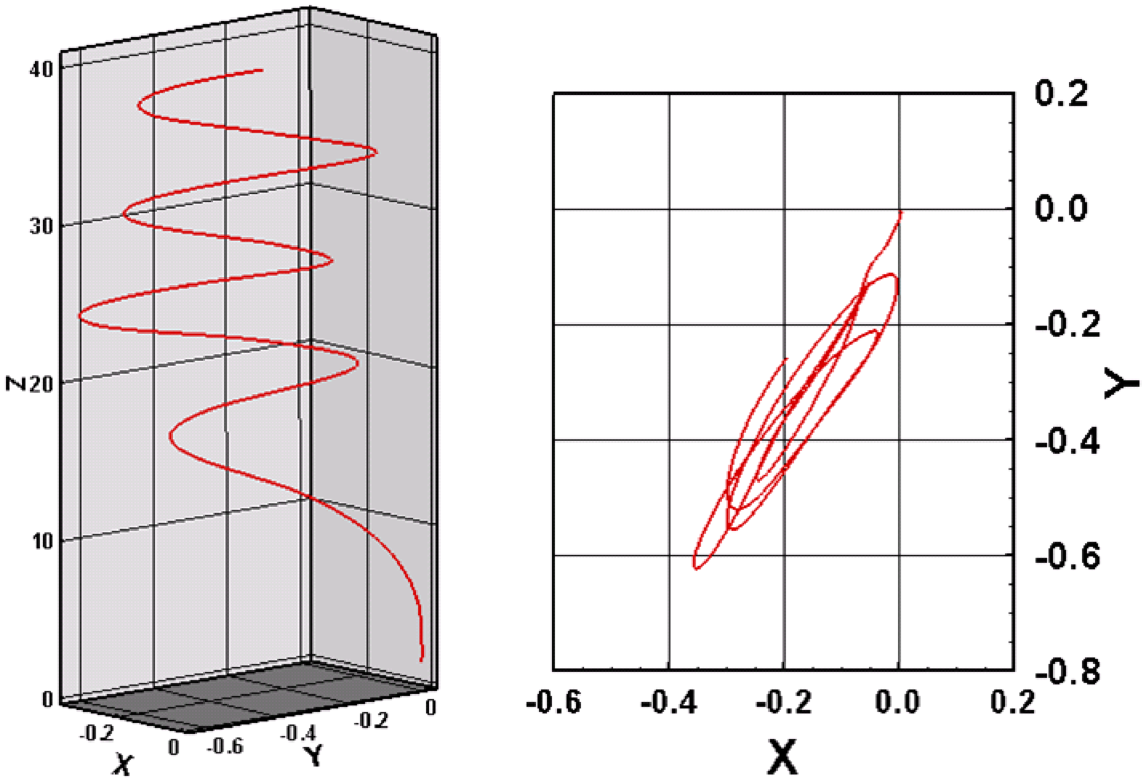

(a) A 3D view

(b) A 2D view from above

Figure 5.1: The trajectory of the mass centre of a bubble rising on a zigzag path.

until an almost constant radius is eventually obtained. The top view of the bubble rise trajectory shown in Figure 5.3b indeed confirms an almost constant spiral radius as the bubble rises. A careful study of the bubble wake structure is shown in Figure 5.4. It is found that the wake structure for a spiralling bubble is totally different from the one observed for a zigzagging bubble. For the spiralling bubble, only one single strong, open recirculation ring is attached to one side of bubble bottom, with the point of attachment being the lowest point of the bubble. This might be due to the higher deformability of the spiralling bubble given the higher Bond number. The point of attachment of the open recirculation ring moves along the bottom side edge of the oblate bubble and

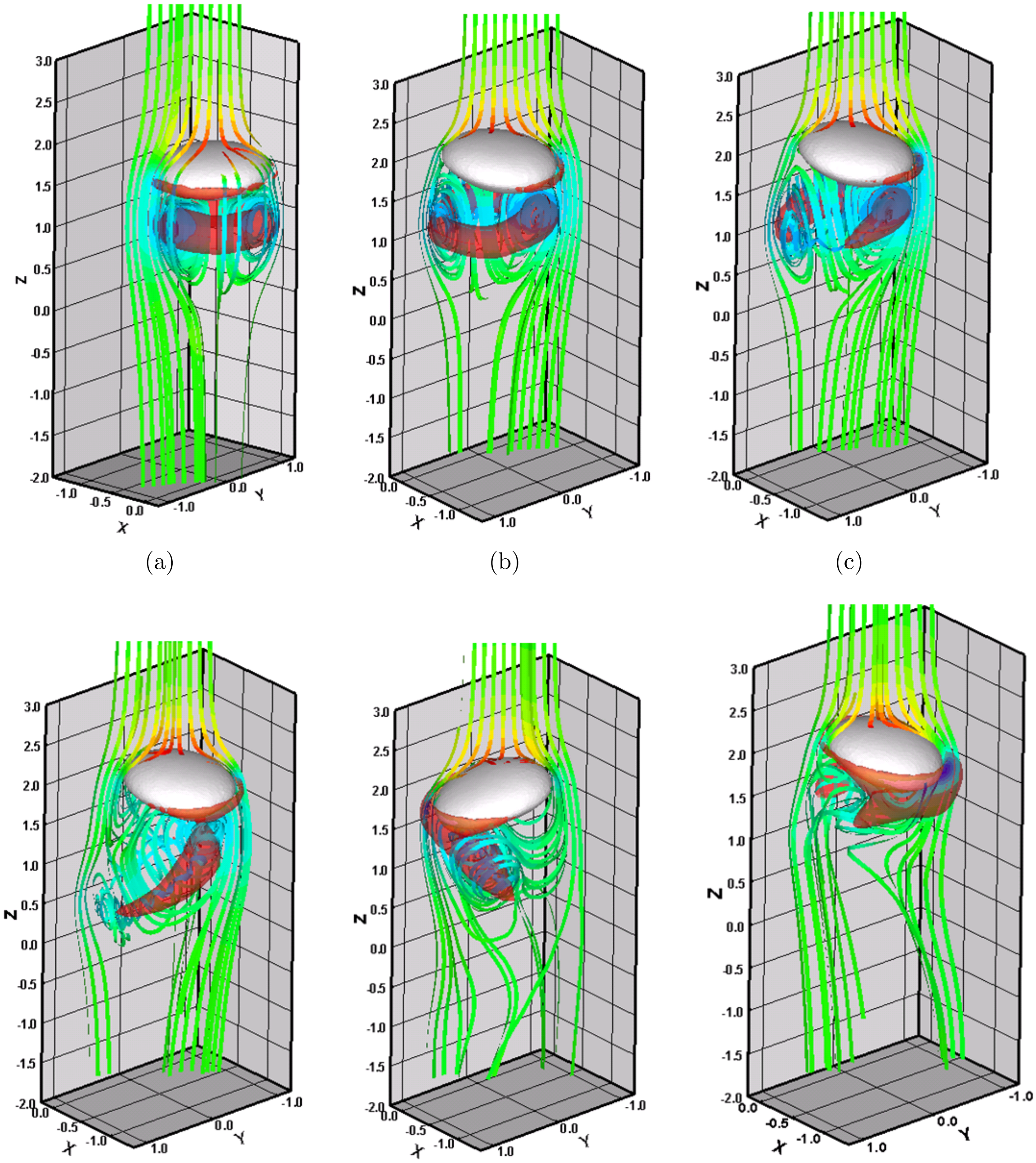

(a) (b) (c)

(d) (e) (f)

Figure 5.2: Variations of the bubble wake structure for a bubble rising on a zigzag path.

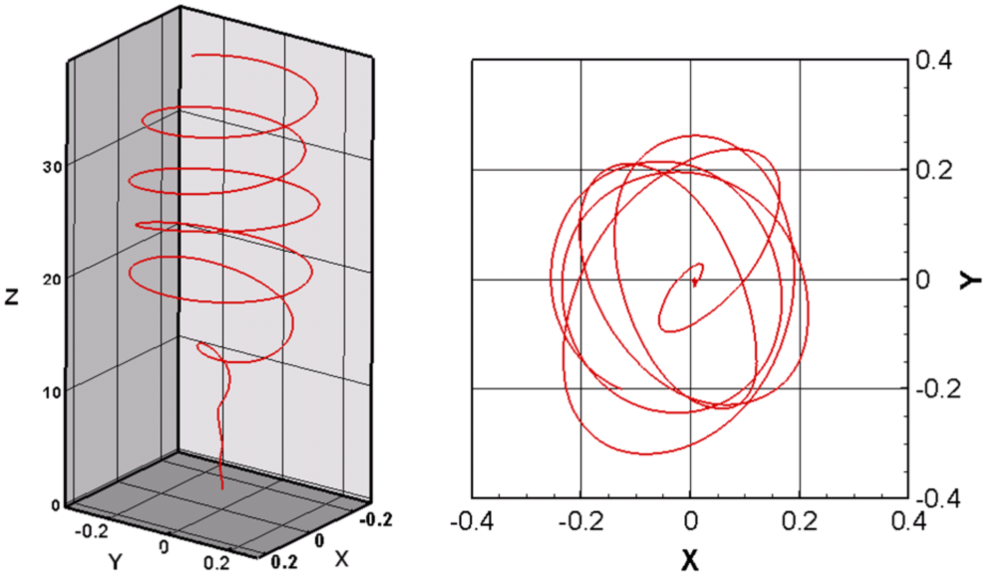

(a) A 3D view

(b) A 2D view from above

Figure 5.3: The trajectory of the mass centre of a bubble rising on a spiral path.

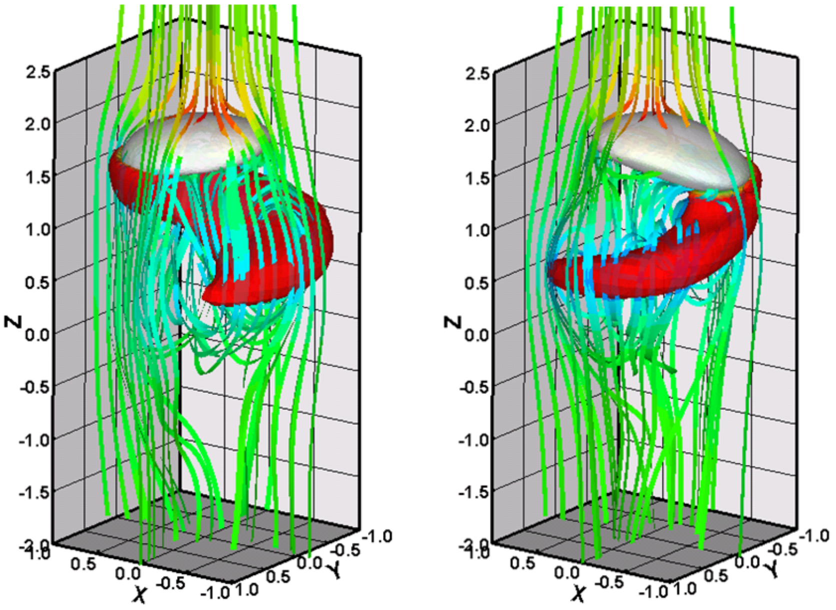

(a)

(b)

Figure 5.4: Variations of the bubble wake structure for a bubble rising on a spiral path.

causes the bubble to follow a spiral trajectory.

# Chapter 6

# Bubble-bubble Interaction

## 6.1 Introduction

The problem of a single bubble rising in a viscous liquid is an ideal case for numerical model validation as illustrated in Chapters 4 and 5. However, the final goal when developing a numerical model for multiphase flow is not just investigating the flow behaviour of single bubbles rising in viscous liquids, but also investigating multi-fluid systems with multiple bubbles. With the confidence from validating the current model for a single bubble rising in a viscous liquid, we therefore extend the model in this Chapter to explore the complex interaction between two bubbles rising in a liquid.

Some background information on bubble-bubble interaction is presented in Section 6.1.1. A review of existing numerical simulation results of this phenomenon is then given in Section 6.2.1, and this Chapter is then concluded by presenting our own numerical results in Section 6.2.2.

### 6.1.1 Background and motivation

In the Introduction of this thesis we mentioned how numerous bubbly flows are both in nature and in engineering and industrial applications. For this reason such flows have been and still are of great interest to both academics and engineers. Several experiments focussing on the interaction of multiple bubbles have been carried out and include work by Brereton and Korotney [13], Manga and Stone [73], Katz and Meneveau [57], Maxworthy and coworkers [74], and more recently by Sanada et. al. [100]. The work of such experimentalists have undoubtedly helped improve our knowledge and understanding of the complex dynamics of interacting bubbles. Yet many questions remain unanswered, and direct numerical simulation methods are increasingly contributing to answering these questions as will become apparent in the following Section. Key issues of interest often include bubble deformation, bouncing, coalescence, and rise velocities.

## 6.2 Numerical simulations of bubble-bubble interaction

### 6.2.1 Review of existing numerical results

The dynamics of a single gas bubble rising in a viscous liquid is fairly well-understood, though it is only recently that improved experimental techniques as well as DNS have helped in gaining more extensive insight into Leonardo's paradox as presented in Chapter 5. Moving on from the study of a single bubble rising, the next natural step is to investigate two bubbles rising and the complex interaction behaviour that consequently may occur. Several DNS studies have been carried out in this respect over the past fifteen years, and some of these will be briefly reviewed below. It will become evident that a range of different numerical methods have been applied to study bubble-bubble interaction.

Early three-dimensional simulations of two interacting bubbles were presented by Unverdi and Tryggvason [114] through the use of their front tracking method. The density and viscosity ratios considered were very modest, but the results were nevertheless impressive at the time (1992).

Chen and coworkers later investigated bubble-bubble interactions by using a modified VOF method taking surface tension into account and using a SIMPLE method for the velocity-pressure coupling [19, 20]. The focus was on the interaction between two equally sized bubbles rising in line, with Reynolds numbers from 10 to 100 and Bond numbers from 5 to 50. They concluded that the bubbles are more likely to merge for high-viscosity liquids and that a jet form behind the leading bubble in low-viscosity liquids, preventing bubble coalescence. Axisymmetry was assumed in these calculations.

The axisymmetric assumption was later relaxed in numerical computations carried out by Koebe [58], also using a VOF approach. Two air bubble pairs of sizes 6 mm and 8 mm rising in water were simulated, mainly for illustration purposes as the runs presented were limited and no conclusions about the bubble-bubble interaction dynamics were drawn. Initial white noise was added to the simulations to induce asymmetric rise behaviour. However, for large enough bubbles such asymmetry should be revealed by the numerical computations themselves without the need for artificial disturbances if the bubbles are allowed to rise for a long enough time period.

A different approach to simulating a rising pair of gas bubbles in viscous liquid was taken by Smolianski et. al. [106] as they applied a finite element method combined with the level set method to carry out two-dimensional computations. The coalescence of two bubbles rising in line were studied for a range of different shape regimes and reasonable agreement was found with experiments and other numerical results. However, the computations were limited by assuming two dimensions, and results for high density and viscosity ratios typical of e.g. the air-water system were not presented.

Around the same time, Watanabe and Sanada presented their axisymmetric numerical results on the in-line motion of a pair of rising bubbles [118]. Like Smolianski et. al. they also used a finite-element method, but they did not couple it with the level set method. Rather, they applied a deforming-spatial-domain/space-time approach to handle the moving and deforming bubbles. Their main focus was on investigating whether there exists an equilibrium distance between two bubbles rising in-line, and both experimental and numerical evidence of such an (unstable) equilibrium was presented.

Yet another computational approach was taken by Cheng et. al. [22] as they introduced a fully three-dimensional lattice Boltzmann method (LBM) to simulate the interaction of two gas bubbles rising in liquid. The LBM is interesting in that it is fundamentally different to the above methods as it solves single particle distributions rather than the macroscopic Navier-Stokes equations. In-line and oblique coalescence of bubbles of equal and un-equal size was considered for a wide range of liquid-gas density ratios, and observations were found to agree well with experimental data.

### 6.2.2 Our numerical results

One of the disadvantages most commonly mentioned about the front tracking method is that it does not handle topological change of the interface such as bubble coalescence and break up in a 'natural manner' as for example the VOF method does. On the other hand, the improved accuracy of the interface handling offered by front tracking count in its favour and has motivated several studies applying front tracking to simulate bubbles undergoing topological change, even in three space dimensions, e.g. [114, 105].

In the present study, three-dimensional bubble coalescence is also modelled. The coalescence process is simplified and based purely on geometric criteria rather than criteria related to the complex interface physics. This means that coalescence occurs when nodes on the two bubble surfaces get close enough, e.g. less than one fifth of the average triangle side length in the surface mesh. The associated topological change and volume conservation is also dealt with in a geometric manner. A similar modelling strategy can also been found in the work by Shin and Juric [105]. In the following we will present two simulations of the interaction of two initially spherical bubbles rising in a quiescent liquid due to buoyancy.

### Bubble-bubble interaction case I

Figure 6.1 shows the interaction of two initially spherical bubbles rising in a quiescent liquid due to buoyancy. Let $D$ represent the effective diameter of the big bubble, and the diameter of the small bubble is half that of the big bubble. The smaller bubble is initially located $2.5D$ above the big bubble in vertical direction, and $0.5D$ axis-off from the big bubble in the horizontal direction of $Y$. The flow conditions are $Bo = 115.0$ and $Ar = 134.6$ for the big bubble, while $Bo = 28.75$ and $Ar = 47.6$ for the smaller bubble. The density and viscosity ratios are $\frac{\rho_L}{\rho_G} = 1181$ and $\frac{\mu_L}{\mu_G} = 5000$, respectively, for both bubbles. Figure 6.1 shows the temporal bubble shape evolution of two ring bubbles. As the big bubble has a higher rise velocity, it catches up with and approaches the small bubble. When they are close enough, the trailing big bubble is significantly affected by the low-pressure zone in the wake of the leading small bubble. The trailing bubble therefore undergoes large deformations and moves towards the bottom wake zone of the leading bubble as shown in Figure 6.1c. Finally, the trailing big bubble merges with the leading smaller bubble, and a toroidal bubble ring as shown in Figure 6.1e is formed. In addition, Figure 6.2 shows the temporal variation of the position of the bubbles in both vertical and horizontal directions. It can be seen from Figure 6.2a that the trailing big bubble has a higher rise speed than the small leading bubble. The interesting finding is that when the two bubbles are close enough, then the rise speed of both bubbles increases significantly. After the coalescence of the two bubbles, the resulting merged bubble represents the familiar situation of a single bubble rising in a liquid. The lateral movement of the trailing bubble caused by the leading bubble can be seen in Figure 6.2b. Even though the leading bubble initially moves slightly away from the trailing bubble laterally, this distance is quite small. However, the trailing bubble, despite its big size, is significantly affected by the leading bubble and moves towards it.

**Bubble-bubble interaction case II**

In the second simulation, we still let $D$ be the effective diameter of the bigger bubble, while the diameter of the smaller bubble remains half that of the bigger bubble. The smaller bubble is initially located $2.5D$ above the bigger bubble in vertical direction just like in case I, but the horizontal centre-off position from the big bubble in the direction of $Y$ is now increased from $0.5D$ to $1.0D$. The flow conditions for the bigger bubble are $Ar = 15.24$ and $Bo = 243.0$, while

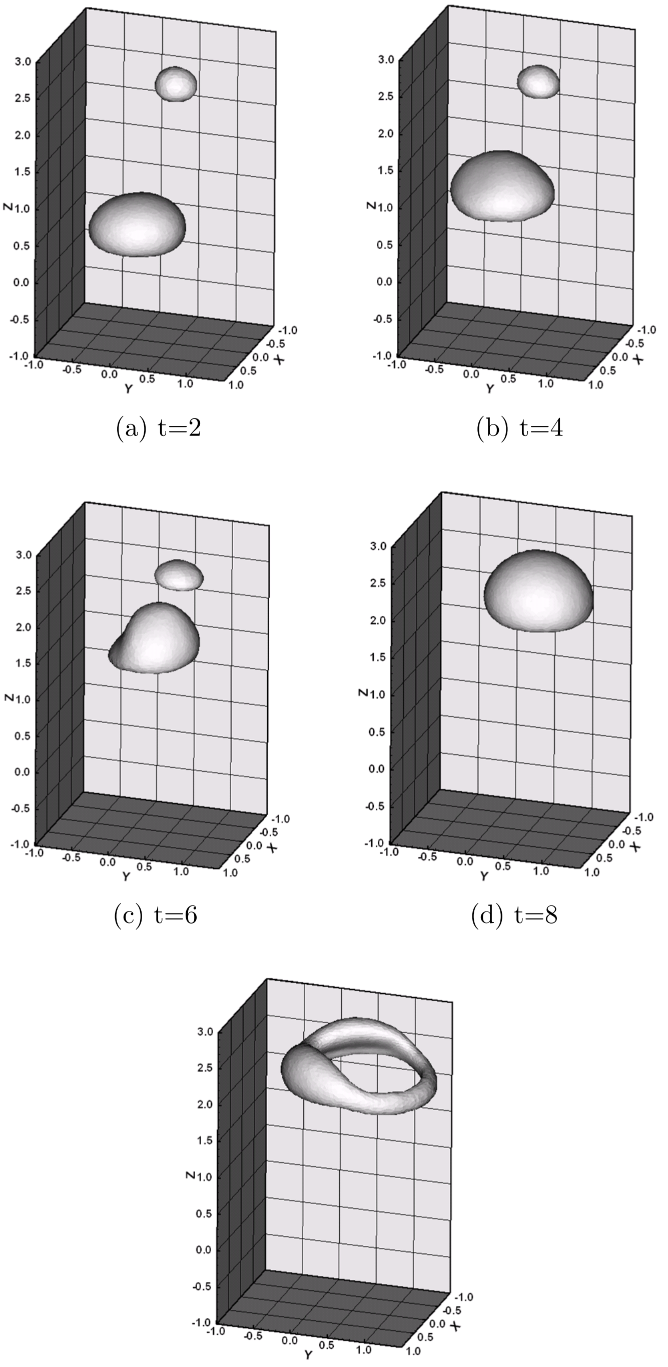

(a) t=2

(b) t=4

(c) t=6

(d) t=8

(e) t=10

Figure 6.1: The interaction of two initially spherical bubbles rising due to buoyancy.

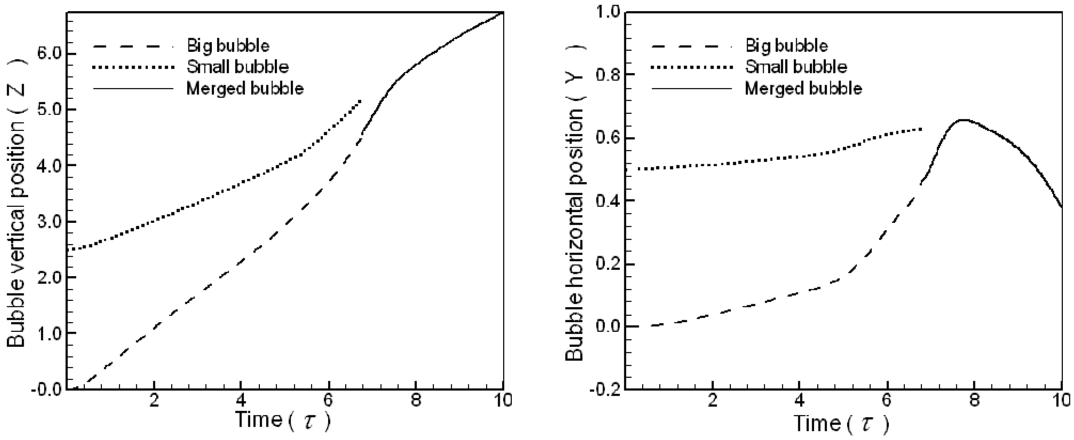

(a) (b)

Figure 6.2: Numerical predictions of (a) the vertical position and (b) the lateral position of the rising bubbles before and after coalescence.

the smaller bubble has $Ar = 5.38$ and $Bo = 60.75$. The density and viscosity ratios remain the same as in case I (i.e. $\frac{\rho_L}{\rho_G} = 1181$ and $\frac{\mu_L}{\mu_G} = 5000$). Figure 6.3 shows the temporal evolution of the two rising bubbles. In this case the initial horizontal off-set between the bubbles is larger than in the previous case, and as a result the bigger bubble now actually overtakes the smaller one. It can be seen from Figures 6.3 and 6.4b that the leading bubble first starts moving laterally away from the trailing bubble, whereas the trailing bubble then starts moving towards the leading bubble before the overtaking occurs ($t = 4.0$, $t = 6.0$, $t = 8.0$). After the bigger bubble has overtaken the smaller one, the smaller bubble is significantly affected by the wake of the bigger bubble. In fact, the smaller bubble is attracted to the wake of the bigger bubble, resulting in a highly deformed and elongated bubble shape as shown in Figure 6.3 ($t = 12.0$, $t = 14.0$, $t = 16.0$). It is also noticed from Figure 6.4a that the smaller bubble is accelerated and rises fast in the wake of the bigger bubble, and eventually it catches up and merges with the bigger bubble as is also shown in Figure 6.3 ($t = 18.0$, $t = 20.0$, $t = 22.0$). On the contrary to case I, the smaller trailing

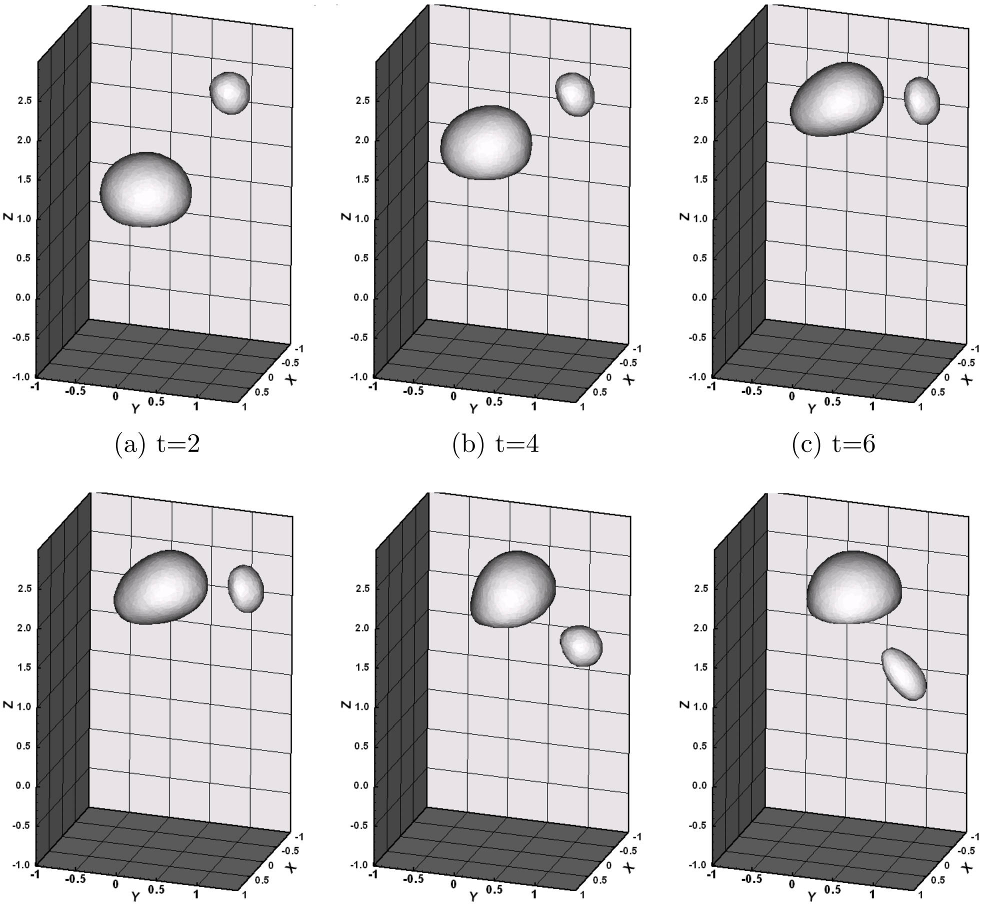

(a) t=2

(b) t=4

(c) t=6

(d) t=8

(e) t=10

(f) t=12

Figure 6.3: The interaction of two initially spherical bubbles rising due to buoyancy.

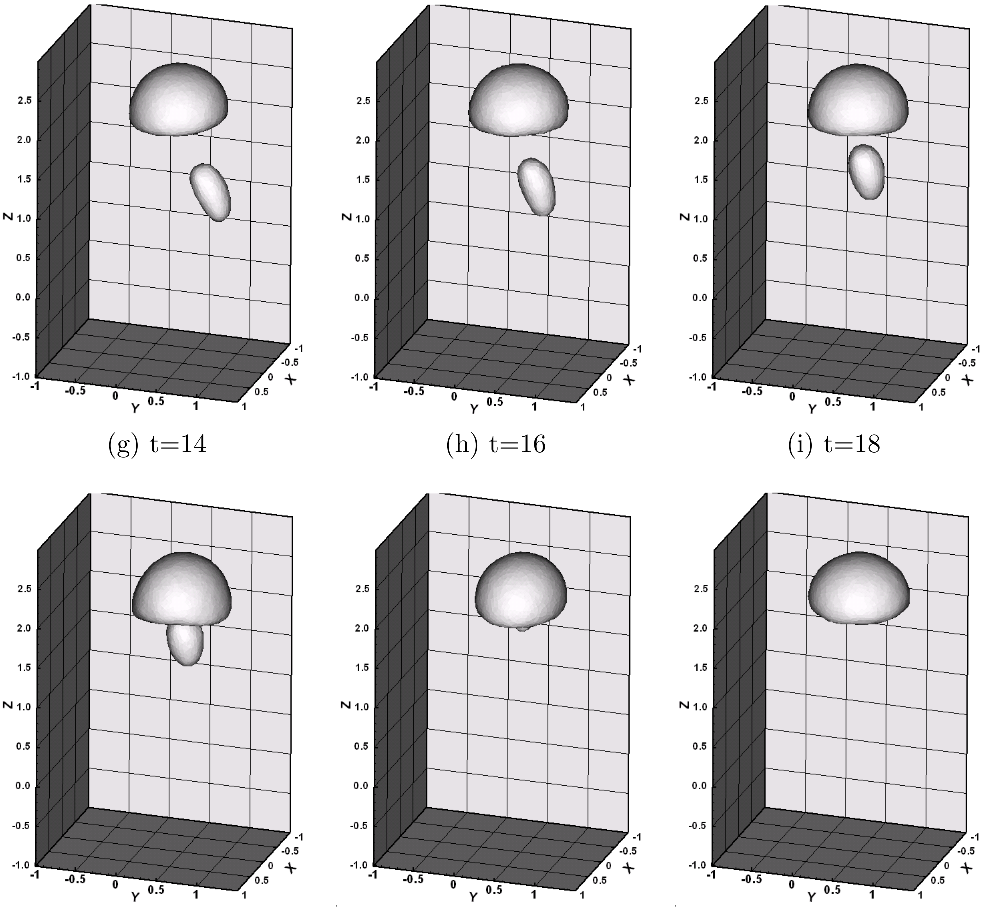

(g) t=14

(h) t=16

(i) t=18

(j) t=20

(k) t=22

(l) t=24

Figure 6.3: (cont.) The interaction of two initially spherical bubbles rising due to buoyancy.

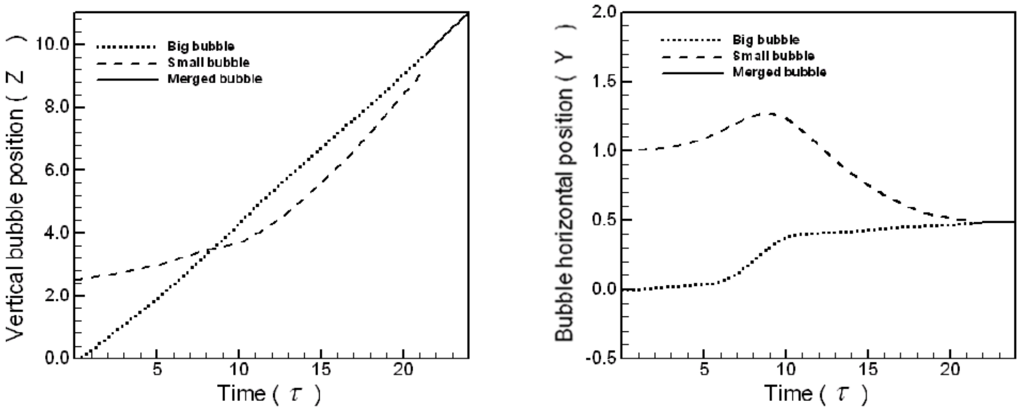

(a) (b)

Figure 6.4: Numerical predictions of (a) the vertical position and (b) the lateral position of the rising bubbles before and after coalescence.

bubble in this case has little or no effect on the rising speed of the bigger bubble.

# Chapter 7

# A Sequential Regularization Method for Two-phase Flow

## 7.1 Introduction

In this Chapter we explore the possibility of applying a *sequential regularization formulation* based flow solver to our front tracking methodology as presented in Chapter 3. The aim of developing such a method is two-fold: obtaining a more efficient flow solver which avoids solving the pressure equation and difficulties associated with it, as well as investigating the feasibility of applying sequential regularization methods to multiphase flows in its own right.

Background information and motivation of the proposed approach follows in Section 7.1.1, while a detailed description of the new scheme and its two main constituents are given in Section 7.2 for two space dimensions. Numerical results obtained using the new method then conclude this Chapter in Section 7.3.

### 7.1.1 Background and motivation

#### More efficient flow solver

The overall solution algorithm proposed in this thesis is summarized in Section 3.6. In that summary, three out of the five steps is concerned with handling the front representing the interface between the gas and the liquid. However, it is step four, namely solving the governing flow equations, that is by far the most expensive step in the entire algorithm. To improve the efficiency of our method it is therefore natural to examine whether this step can be carried out in an alternative manner. Indeed, numerous solution methods have been proposed in the literature that could possibly be adapted in step four. However, unlike some other methods, the SIMPLE method has proven to be a robust solver even for large density and viscosity ratios - a crucial property in our context of two-phase flow. We would therefore like to retain this robustness of SIMPLE but at the same time somehow reduce the overall computational cost. One approach that have given rise to many methods is to perform an initial reformulation and/or regularization of the governing equations with the aim of obtaining an alternative formulation that is hopefully better posed and easier to solve than the original formulation. It is indeed such an approach we shall explore here - namely a sequential regularization method (SRM).

#### SRM in a new context

Sequential regularization methods were first introduced for differential-algebraic equations (DAEs), a special case of which is simply ordinary differential equations with equality constraints. See for example [12, 40] for more details. One particular SRM to solve DAEs was proposed by Ascher and Lin [3, 2], and Lin later extended this approach to partial differential-algebraic equations (PDAEs) [62]. Specifically, the SRM was applied to the incompressible Navier-Stokes equations for single phase flow. Lin and coworkers developed the method further in the Navier-Stokes context: a discussion on the method itself can be found in [64] where a fully explicit method was introduced. The application of SRM in a finite element context was then given in [63], while further numerical analysis of the method was presented in [68]. An application to a long time solution of the Navier-Stokes equations was also given in [65].

All of the above work considered single phase flow. We here extend the SRM to apply to two-phase flow using the one-fluid formulation as introduced in Section 2.2.2. We remember that the density and viscosity now is discontinuous across fluid interfaces and that there is also a singular source term on the interface due to surface tension. For this system we obtain the following formulation for the SRM: Let $p_0(x,t)$ be an initial guess for the pressure and $\alpha_1$, $\alpha_2 \geq 0$. For $s = 1, 2, ...$, solve the system

$$p_s = p_{s-1} - \frac{1}{\epsilon}\Big(\alpha_1 \frac{\partial\big(\nabla \cdot \mathbf{u}_s\big)}{\partial t} + \alpha_2 \nabla \cdot \mathbf{u}_s\Big) \tag{7.1}$$

and

$$\begin{aligned} &\frac{\partial(\rho \mathbf{u}_s)}{\partial t} - \frac{1}{\epsilon}\nabla \cdot \Big(\alpha_1 \frac{\partial\big(\nabla \cdot \mathbf{u}_s\big)}{\partial t} + \alpha_2 \nabla \cdot \mathbf{u}_s\Big) + \nabla \cdot \rho \mathbf{u}_s \mathbf{u}_s = \\ &-\nabla p_{s-1} + \frac{1}{Ar}\nabla \cdot \big(\mu(\nabla \mathbf{u}_s + (\nabla \mathbf{u}_s)^T)\big) + \frac{1}{Bo}\int_\Gamma \kappa \mathbf{n} \delta(\mathbf{x} - \mathbf{x}_\Gamma) dS + (\rho - 1)\mathbf{g}. \end{aligned} \tag{7.2}$$

## 7.2 A SIMPLE-SR method in two dimensions

Our development and assessment of a combined SIMPLE-SR scheme shall for simplicity be carried out in two space dimensions. However, the extension to a three-dimensional method is in principle straight forward.

### Governing equations in component form

First we introduce notation applicable to the two-dimensional setting. Let $u$ and $v$ be the velocity components of the flow field in $x$- and $y$-direction, respectively, $\rho$ the fluid density, $p$ the pressure, $\mu$ the fluid viscosity, $\rho_l$ the density of the liquid, $g_x$ and $g_y$ the gravitational components, and $S_x$ and $S_y$ the components of the source term. Note that in the case of two-phase flow, surface tension will be taken into account and consequently the sources will include a singular surface term.

The vector formulation of the flow equations as given by Equation (2.9) yields the following left-hand side (LHS) of the momentum equation in the $x$-direction:

$$\text{LHS} = \frac{\partial(\rho u)}{\partial t} + \frac{\partial(\rho u u)}{\partial x} + \frac{\partial(\rho v u)}{\partial y}. \tag{7.3}$$

Using the product rule, this can be expanded to

$$\text{LHS} = \rho\frac{\partial u}{\partial t} + \rho u\frac{\partial u}{\partial x} + \rho v\frac{\partial u}{\partial y} + u\frac{\partial \rho}{\partial t} + u\frac{\partial(\rho u)}{\partial x} + u\frac{\partial(\rho v)}{\partial y}. \tag{7.4}$$

Now note that the continuity equation (2.4) reads as follows in the two-dimensional case:

$$\frac{\partial \rho}{\partial t} + \frac{\partial (\rho u)}{\partial x} + \frac{\partial (\rho v)}{\partial y} = 0. \tag{7.5}$$

From this we observe that the three last terms of Equation (7.4) are the continuity equation times $u$. Since this must be zero, Equation (7.4) simplifies to

$$\text{LHS} = \rho \frac{\partial u}{\partial t} + \rho u \frac{\partial u}{\partial x} + \rho v \frac{\partial u}{\partial y}, \tag{7.6}$$

so we have just shown that

$$\frac{\partial (\rho u)}{\partial t} + \frac{\partial (\rho u u)}{\partial x} + \frac{\partial (\rho v u)}{\partial y} = \rho \frac{\partial u}{\partial t} + \rho u \frac{\partial u}{\partial x} + \rho v \frac{\partial u}{\partial y}. \tag{7.7}$$

A corresponding identity can be shown for the momentum equation in $y$-direction, and in component form we thus have the following three simultaneous equations for two space dimensions:

$$\frac{\partial u}{\partial x} + \frac{\partial v}{\partial y} = 0, \tag{7.8}$$

$$\begin{aligned} \rho \frac{\partial u}{\partial t} + \rho \Big( u \frac{\partial u}{\partial x} + v \frac{\partial u}{\partial y} \Big) &= \\ - \frac{\partial p}{\partial x} + 2 \frac{\partial}{\partial x} \Big( \mu \frac{\partial u}{\partial x} \Big) &+ \frac{\partial}{\partial y} \Big( \mu \big( \frac{\partial u}{\partial y} + \frac{\partial v}{\partial x} \big) \Big) + S_x + (\rho - \rho_l) g_x \end{aligned} \tag{7.9}$$

and

$$\begin{aligned} \rho \frac{\partial v}{\partial t} + \rho \Big( u \frac{\partial v}{\partial x} + v \frac{\partial v}{\partial y} \Big) &= \\ - \frac{\partial p}{\partial y} + 2 \frac{\partial}{\partial y} \Big( \mu \frac{\partial v}{\partial y} \Big) &+ \frac{\partial}{\partial x} \Big( \mu \big( \frac{\partial u}{\partial y} + \frac{\partial v}{\partial x} \big) \Big) + S_y + (\rho - \rho_l) g_y. \end{aligned} \tag{7.10}$$

### 7.2.1 The SIMPLE algorithm in 2D

Equations (7.8) - (7.10) have been solved previously in this work by using the SIMPLE algorithm. This is a finite volume method where the velocity and the pressure are calculated at staggered grid points. Equations (7.9) and (7.10) above may be re-expressed such that the terms that are treated implicitly appear on the left, and the terms that appear on the right are treated explicitly:

$$\begin{aligned}\rho\frac{\partial u}{\partial t} + \rho\Big(u\frac{\partial u}{\partial x} + v\frac{\partial u}{\partial y}\Big) - \frac{\partial}{\partial x}\Big(\mu\frac{\partial u}{\partial x}\Big) - \frac{\partial}{\partial y}\Big(\mu\frac{\partial u}{\partial y}\Big) &= \\ -\frac{\partial p}{\partial x} + \frac{\partial}{\partial x}\Big(\mu\frac{\partial u}{\partial x}\Big) + \frac{\partial}{\partial y}\Big(\mu\frac{\partial v}{\partial x}\Big) &+ S_x + (\rho - \rho_l)g_x \end{aligned} \tag{7.11}$$

and

$$\begin{aligned}\rho\frac{\partial v}{\partial t} + \rho\Big(u\frac{\partial v}{\partial x} + v\frac{\partial v}{\partial y}\Big) - \frac{\partial}{\partial y}\Big(\mu\frac{\partial v}{\partial y}\Big) - \frac{\partial}{\partial x}\Big(\mu\frac{\partial v}{\partial x}\Big) &= \\ -\frac{\partial p}{\partial y} + \frac{\partial}{\partial y}\Big(\mu\frac{\partial v}{\partial y}\Big) + \frac{\partial}{\partial x}\Big(\mu\frac{\partial u}{\partial y}\Big) &+ S_y + (\rho - \rho_l)g_y. \end{aligned} \tag{7.12}$$

The SIMPLE method for solving Equations (7.8), (7.11) and (7.12) is then:

1. Guess the initial pressure distribution $p^*$.

2. Solve a discrete form of the momentum equations (7.11) and (7.12) to obtain an intermediate velocity field, $u^*$ and $v^*$. Note that when solving for $u^*$, then $v^*$ is treated as known (e.g. value from previous time step),

so the momentum equations are de-coupled. When solving for $v^*$, then $u^*$ is treated as known (the one calculated previously).

3. Solve a pressure-correction equation to obtain the corrected pressure $p$.

4. Evaluate the corrected velocity field $u$ and $v$.

5. Treat the corrected pressure $p$ as a new guessed pressure $p^*$ and repeat the whole procedure until a converged solution is obtained.

6. After having obtained a converged solution, all the coefficients will be updated. Repeat Steps 1 - 5 to march to the next time step.

Numerical results indicate that the above algorithm is quite robust. However, there is still difficulty in dealing with the pressure-correction equation in step 3 (e.g. artificial boundary condition for the pressure), and the number of iterations required in Step 5 for convergence is usually quite high, making the algorithm computationally expensive. Seeking a more efficient method, we would like to investigate the feasibility of combining the *sequential regularization* approach with the SIMPLE algorithm.

### 7.2.2 The sequential regularization method in 2D

The vector Equations (7.1) and (7.2) can be re-expressed in component form in two space dimensions as follows:

$$\alpha_1\Big(\frac{\partial u_s}{\partial x}\Big)_t + \alpha_1\Big(\frac{\partial v_s}{\partial y}\Big)_t + \alpha_2\frac{\partial u_s}{\partial x} + \alpha_2\frac{\partial v_s}{\partial y} = -\epsilon\big(p_s - p_{s-1}\big), \tag{7.13}$$

$$\begin{aligned}\rho\frac{\partial u_s}{\partial t}+\rho\Big(u_s\frac{\partial u_s}{\partial x}+v_s\frac{\partial u_s}{\partial y}\Big)&=\\ -\frac{\partial}{\partial x}\Big[p_{s-1}-\frac{1}{\epsilon}\Big(\alpha_1\big(\frac{\partial u_s}{\partial x}\big)_t+\alpha_1\big(\frac{\partial v_s}{\partial y}\big)_t+\alpha_2\frac{\partial u_s}{\partial x}+\alpha_2\frac{\partial v_s}{\partial y}\Big)\Big]&\\ +2\frac{\partial}{\partial x}\Big(\mu\frac{\partial u_s}{\partial x}\Big)+\frac{\partial}{\partial y}\Big(\mu\big(\frac{\partial u_s}{\partial y}+\frac{\partial v_s}{\partial x}\big)\Big)+S_x+\big(\rho-\rho_l\big)g_x&\end{aligned}\qquad(7.14)$$

and

$$\begin{aligned}\rho\frac{\partial v_s}{\partial t}+\rho\Big(u_s\frac{\partial v_s}{\partial x}+v_s\frac{\partial v_s}{\partial y}\Big)&=\\ -\frac{\partial}{\partial y}\Big[p_{s-1}-\frac{1}{\epsilon}\Big(\alpha_1\big(\frac{\partial u_s}{\partial x}\big)_t+\alpha_1\big(\frac{\partial v_s}{\partial y}\big)_t+\alpha_2\frac{\partial u_s}{\partial x}+\alpha_2\frac{\partial v_s}{\partial y}\Big)\Big]&\\ +2\frac{\partial}{\partial y}\Big(\mu\frac{\partial v_s}{\partial y}\Big)+\frac{\partial}{\partial x}\Big(\mu\big(\frac{\partial u_s}{\partial y}+\frac{\partial v_s}{\partial x}\big)\Big)+S_y+\big(\rho-\rho_l\big)g_y&\end{aligned}\qquad(7.15)$$

Note that the subscript $s$ refers to the number of the iteration of the sequential regularization.

### 7.2.3 Combining SIMPLE and SRM

The sequential regularization formulation (7.13) - (7.15) brings in some additional terms compared to the standard formulation (7.8) - (7.10). These terms are

$$\begin{aligned}-\frac{\partial}{\partial x}\Big[-\frac{1}{\epsilon}\Big(\alpha_1\big(\frac{\partial u_s}{\partial x}\big)_t+\alpha_1\big(\frac{\partial v_s}{\partial y}\big)_t+\alpha_2\frac{\partial u_s}{\partial x}+\alpha_2\frac{\partial v_s}{\partial y}\Big)\Big]&\\ =\frac{1}{\epsilon}\Big(\alpha_1\big(\frac{\partial^2 u_s}{\partial x^2}\big)_t+\alpha_1\big(\frac{\partial^2 v_s}{\partial x\partial y}\big)_t+\alpha_2\frac{\partial^2 u_s}{\partial x^2}+\alpha_2\frac{\partial^2 v_s}{\partial x\partial y}\Big)&\end{aligned}\qquad(7.16)$$

and

$$
\begin{aligned}
&-\frac{\partial}{\partial y}\Big[-\frac{1}{\epsilon}\Big(\alpha_1\big(\frac{\partial u_s}{\partial x}\big)_t+\alpha_1\big(\frac{\partial v_s}{\partial y}\big)_t+\alpha_2\frac{\partial u_s}{\partial x}+\alpha_2\frac{\partial v_s}{\partial y}\Big)\Big] \\
&\qquad\qquad=\frac{1}{\epsilon}\Big(\alpha_1\big(\frac{\partial^2 u_s}{\partial x\partial y}\big)_t+\alpha_1\big(\frac{\partial^2 v_s}{\partial y^2}\big)_t+\alpha_2\frac{\partial^2 u_s}{\partial x\partial y}+\alpha_2\frac{\partial^2 v_s}{\partial y^2}\Big). \quad (7.17)
\end{aligned}
$$

The SIMPLE algorithm described in Section 7.2.1 solves Equations (7.8) - (7.10). The idea is to modify the algorithm using the SR formulation as stated in Equations (7.13) - (7.15), that is, Step 3 of the algorithm may be removed and the pressure updating in Step 5 may be done using Equation (7.13). Thus the modified algorithm avoids solving the pressure-correction equation, and from the theory of the SR formulation the computation of the pressure may be more stable if $\alpha_1 \neq 0$. The details for this modification will be presented in Section 7.2.4 as we first present the main steps of the SIMPLE-SR algorithm:

### SIMPLE-SR algorithm

Notation: Subscript $s$ refers to the number of the iteration of the sequential regularization, while superscript $n$ refers to the time step.

1. Make an initial guess for the pressure at all time steps: $p_0^n$, $n = 1, 2, 3, 4, ....$

2. Calculate $p_1^0$ through the relation

$$p_1^0 = p_0^0 - \frac{1}{\epsilon}\Big[\alpha_1\big(\frac{\partial u_1^0}{\partial x}\big)_t+\alpha_1\big(\frac{\partial v_1^0}{\partial y}\big)_t+\alpha_2\frac{\partial u_1^0}{\partial x}+\alpha_2\frac{\partial v_1^0}{\partial y}\Big] \quad (7.18)$$

Assuming an initially stationary flow field, (7.18) reduces to

$$p_1^0 = p_0^0 - \frac{\alpha_2}{\epsilon}\Big[\frac{\partial u_1^0}{\partial x}+\frac{\partial v_1^0}{\partial y}\Big]. \quad (7.19)$$

Note that $u_s^0 = u_1^0$ and $v_s^0 = v_1^0$ for all $s$ since the initial velocity field is a known, given quantity. Therefore we may find $p_s^0$ for all $s$ through the relation

$$p_s^0 = p_{s-1}^0 - \frac{\alpha_2}{\epsilon}\Big[\frac{\partial u_1^0}{\partial x} + \frac{\partial v_1^0}{\partial y}\Big]. \tag{7.20}$$

3. The first time step:

   Calculate $u_1^1$ and $v_1^1$ by solving the momentum equations (7.14) and (7.15) that are modified for sequential regularization. The pressure used in the momentum equations to find $u_1^1$ and $v_1^1$ is $p_0^0$. Similarly, one may find $u_s^1$ and $v_s^1$ by using the pressure $p_{s-1}^0$ in the momentum equations.

   Conclude this step by calculating $p_s^1$ to be used in the next time step:

$$p_s^1 = p_{s-1}^1 - \frac{1}{\epsilon}\Big[\alpha_1\big(\frac{\partial u_s^1}{\partial x}\big)_t + \alpha_1\big(\frac{\partial v_s^1}{\partial y}\big)_t + \alpha_2\frac{\partial u_s^1}{\partial x} + \alpha_2\frac{\partial v_s^1}{\partial y}\Big] \tag{7.21}$$

4. The $n$-th time step:

   Find $u_s^n$ and $v_s^n$ (pressure $p_{s-1}^{n-1}$) using the modified SIMPLE algorithm with the pressure already obtained in the previous step, for $s = 1, 2, 3, 4, ....$

   Calculate $p_s^n$ to be used in the next time step:

$$p_s^n = p_{s-1}^n - \frac{1}{\epsilon}\Big[\alpha_1\big(\frac{\partial u_s^n}{\partial x}\big)_t + \alpha_1\big(\frac{\partial v_s^n}{\partial y}\big)_t + \alpha_2\frac{\partial u_s^n}{\partial x} + \alpha_2\frac{\partial v_s^n}{\partial y}\Big]. \tag{7.22}$$

5. Advance the solution in time by repeating the previous step as many times as required.

### 7.2.4 A special case

Note that the additional terms in (7.16) and (7.17) include terms with mixed space-time derivatives of the third-order if $\alpha_1 \neq 0$. For simplicity, we therefore here suggest to consider the special case when $\alpha_1 = 0$. The additional terms (7.16) and (7.17) brought in by the sequential regularization formulation then reduce to

$$-\frac{\partial}{\partial x}\Big[-\frac{\alpha_2}{\epsilon}\Big(\frac{\partial u_s}{\partial x}+\frac{\partial v_s}{\partial y}\Big)\Big] = \frac{\alpha_2}{\epsilon}\Big(\frac{\partial^2 u_s}{\partial x^2}+\frac{\partial^2 v_s}{\partial x \partial y}\Big) \tag{7.23}$$

and

$$-\frac{\partial}{\partial y}\Big[-\frac{\alpha_2}{\epsilon}\Big(\frac{\partial u_s}{\partial x}+\frac{\partial v_s}{\partial y}\Big)\Big] = \frac{\alpha_2}{\epsilon}\Big(\frac{\partial^2 u_s}{\partial x \partial y}+\frac{\partial^2 v_s}{\partial y^2}\Big). \tag{7.24}$$

Hence Equations (7.13) - (7.15) will simplify to

$$\alpha_2\frac{\partial u_s}{\partial x}+\alpha_2\frac{\partial v_s}{\partial y} = -\epsilon\big(p_s - p_{s-1}\big), \tag{7.25}$$

$$\begin{aligned}\rho\frac{\partial u_s}{\partial t}+\rho\Big(u_s\frac{\partial u_s}{\partial x}+v_s\frac{\partial u_s}{\partial y}\Big) &= -\frac{\partial}{\partial x}\Big[p_{s-1}-\frac{\alpha_2}{\epsilon}\Big(\frac{\partial u_s}{\partial x}+\frac{\partial v_s}{\partial y}\Big)\Big]\\ &+2\frac{\partial}{\partial x}\Big(\mu\frac{\partial u_s}{\partial x}\Big)+\frac{\partial}{\partial y}\Big(\mu(\frac{\partial u_s}{\partial y}+\frac{\partial v_s}{\partial x})\Big)+S_x+\big(\rho-\rho_l\big)g_x,\end{aligned} \tag{7.26}$$

and

$$\begin{aligned}\rho\frac{\partial v_s}{\partial t}+\rho\Big(u_s\frac{\partial v_s}{\partial x}+v_s\frac{\partial v_s}{\partial y}\Big) &= -\frac{\partial}{\partial y}\Big[p_{s-1}-\frac{\alpha_2}{\epsilon}\Big(\frac{\partial u_s}{\partial x}+\frac{\partial v_s}{\partial y}\Big)\Big]\\ &+2\frac{\partial}{\partial y}\Big(\mu\frac{\partial v_s}{\partial y}\Big)+\frac{\partial}{\partial x}\Big(\mu(\frac{\partial u_s}{\partial y}+\frac{\partial v_s}{\partial x})\Big)+S_y+\big(\rho-\rho_l\big)g_y.\end{aligned} \tag{7.27}$$

Some new terms, $\frac{\alpha_2}{\epsilon}\frac{\partial^2 v_s}{\partial x \partial y}$ and $\frac{\alpha_2}{\epsilon}\frac{\partial^2 u_s}{\partial x \partial y}$, will be treated explicitly, while the remaining new terms, $\frac{\alpha_2}{\epsilon}\frac{\partial^2 u_s}{\partial x^2}$ and $\frac{\alpha_2}{\epsilon}\frac{\partial^2 v_s}{\partial y^2}$, will be treated implicitly. Collecting all the implicit terms on the left and the explicit terms on the right, Equations (7.26) - (7.27) may be re-expressed as

$$\begin{aligned} \rho\frac{\partial u_s}{\partial t} + \rho\Big(u_s\frac{\partial u_s}{\partial x} + v_s\frac{\partial u_s}{\partial y}\Big) - \frac{\partial}{\partial x}\Big((\mu + \frac{\alpha_2}{\epsilon})\frac{\partial u_s}{\partial x}\Big) - \frac{\partial}{\partial y}\Big(\mu\frac{\partial u_s}{\partial y}\Big) = \\ -\frac{\partial p_{s-1}}{\partial x} + \frac{\partial}{\partial x}\Big(\mu\frac{\partial u_s}{\partial x}\Big) + \frac{\partial}{\partial y}\Big((\mu + \frac{\alpha_2}{\epsilon})\frac{\partial v_s}{\partial x}\Big) + S_x + \big(\rho - \rho_l\big)g_x, \end{aligned} \tag{7.28}$$

and

$$\begin{aligned} \rho\frac{\partial v_s}{\partial t} + \rho\Big(u_s\frac{\partial v_s}{\partial x} + v_s\frac{\partial v_s}{\partial y}\Big) - \frac{\partial}{\partial y}\Big((\mu + \frac{\alpha_2}{\epsilon})\frac{\partial v_s}{\partial y}\Big) - \frac{\partial}{\partial x}\Big(\mu\frac{\partial v_s}{\partial x}\Big) = \\ -\frac{\partial p_{s-1}}{\partial y} + \frac{\partial}{\partial y}\Big(\mu\frac{\partial v_s}{\partial y}\Big) + \frac{\partial}{\partial x}\Big((\mu + \frac{\alpha_2}{\epsilon})\frac{\partial u_s}{\partial y}\Big) + S_y + \big(\rho - \rho_l\big)g_y. \end{aligned} \tag{7.29}$$

If we compare the sequential regularization momentum equations (7.28) and (7.29) with the original momentum equations (7.11) and (7.12), we see a striking resemblance. This means that the original SIMPLE solver can be deployed to solve the momentum equations in the sequential regularization formulation by merely changing the value of some coefficients.

We repeat the solution algorithm in this special case:

1. Make an initial guess for the pressure at all time steps: $p_0^n$, $n = 1, 2, 3, 4, ....$

2. Calculate $p_1^0$ through the relation

$$p_1^0 = p_0^0 - \frac{\alpha_2}{\epsilon}\Big[\frac{\partial u_1^0}{\partial x} + \frac{\partial v_1^0}{\partial y}\Big] \tag{7.30}$$

Note that $u_s^0 = u_1^0$ and $v_s^0 = v_1^0$ for all $s$ since the initial velocity field is a known, given quantity. Therefore we may find $p_s^0$ for all $s$ through the relation

$$p_s^0 = p_{s-1}^0 - \frac{\alpha_2}{\epsilon}\left[\frac{\partial u_1^0}{\partial x} + \frac{\partial v_1^0}{\partial y}\right]. \tag{7.31}$$

3. The first time step:

   Calculate $u_1^1$ and $v_1^1$ by solving the momentum equations (7.28) and (7.29) that are modified for sequential regularization. We apply the modified SIMPLE algorithm as described above where one of the additional terms due to SR are incorporated in the source term and the other is treated implicitly. The pressure used in the momentum equations to find $u_1^1$ and $v_1^1$ is $p_0^0$. Similarly, one may find $u_s^1$ and $v_s^1$ by using the pressure $p_{s-1}^0$ in the momentum equations.

   Conclude this step by calculating $p_s^1$ to be used in the next time step:

$$p_s^1 = p_{s-1}^1 - \frac{\alpha_2}{\epsilon}\left[\frac{\partial u_s^1}{\partial x} + \frac{\partial v_s^1}{\partial y}\right] \tag{7.32}$$

4. The $n$-th time step:

   Find $u_s^n$ and $v_s^n$ (pressure $p_{s-1}^{n-1}$) using the modified SIMPLE algorithm, for $s = 1, 2, 3, 4, ....$

   Calculate $p_s^n$ to be used in the next time step:

$$p_s^n = p_{s-1}^n - \frac{\alpha_2}{\epsilon}\left[\frac{\partial u_s^n}{\partial x} + \frac{\partial v_s^n}{\partial y}\right]. \tag{7.33}$$

5. Advance the solution in time by repeating the previous step as many times as required.

## 7.3 Numerical results

There are several numerical parameters involved in the SR method, and in this section we present results from a detailed sensitivity analysis of a selection of these parameters. We then draw some conclusions and recommendations for values with respect to the parameters of interest.

### 7.3.1 Parameters of interest

When applying sequential regularization (SR) in combination with an iterative solver for the momentum equations, there are a number of parameters related to the solution process. Parameters controlling the SR include the number of relaxation steps $M$ at each time step and the penalty constant $\epsilon$, while the number of iterations $N$ regulates the solver for the momentum equations. We will in the following study what impact variations of these parameters have on the computed results of a single bubble rising.

Bubbles in two different flow regimes will be considered: regime A, which is in the regime of spherical bubbles, and regime B, which is in the skirted bubble regime. Further details on the physical properties of the liquid and gas bubble in these two regimes may be found in Table 7.1. Furthermore, a range of relevant parameters kept constant in all simulations are listed in Table 7.2. Eleven different cases with a variation of certain parameters where run for both regime A and regime B - see Table 7.3 for details.

| Parameter | Regime A | Regime B |
|---|---|---|
| $Ar$ | 1.671 | 15.24 |
| $Bo$ | 17.7 | 243 |
| $\rho_g/\rho_l$ | 1000 | 1000 |
| $\mu_g/\mu_l$ | 100 | 100 |

Table 7.1: Physical parameters for two different bubble regimes

| | |
|---|---|
| Computational domain: | $[0, 8] \times [0, 4]$ |
| Grid cells in $x$-direction: | 200 |
| Grid cells in $y$-direction: | 100 |
| Grid size $\Delta x = \Delta y$: | 0.04 |
| Time step: | 0.002 |
| Total time steps: | 2000 |
| End time: | 4.0 |

Table 7.2: Computational set-up for testing the SIMPLE-SR method

| Case | Penalty parameter $\epsilon$ | Sequential regularization steps $M$ | Solution iterations $N$ |
|---|---|---|---|
| 1 | 0.5 | 5 | 30 |
| 2 | 0.5 | 5 | 10 |
| 3 | 0.5 | 5 | 50 |
| 4 | 0.5 | 10 | 30 |
| 5 | 0.5 | 15 | 30 |
| 6 | 0.25 | 5 | 30 |
| 7 | 0.1 | 5 | 30 |
| 8 | 0.75 | 5 | 30 |
| 9 | 1 | 5 | 30 |
| 10 | 2 | 5 | 30 |
| 11 | 0.5 | 30 | 30 |

Table 7.3: List of test cases with variation of the parameters

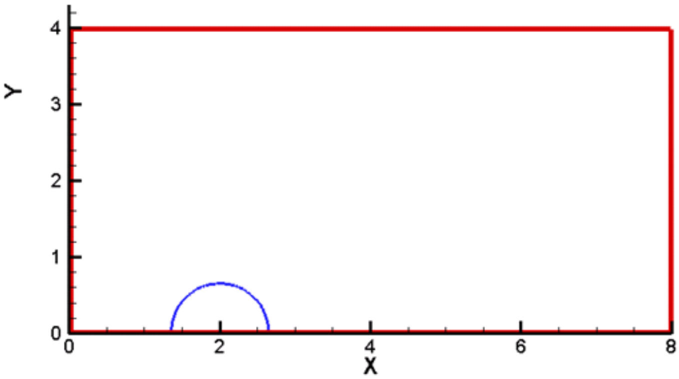

Figure 7.1: The initial set-up. The computational domain is indicated in red, and the original position of the bubble in blue. Note that gravity here points in the negative x-direction.

### 7.3.2 Results from the parameter study

The computational set-up can be seen in Figure 7.1.

**Value of the relaxation parameter $\alpha_2$**

By studying the governing equations, one can see that the relaxation parameter $\alpha_2$ always appears together with the penalty parameter $\epsilon$ as $\frac{\alpha_2}{\epsilon}$. For simplicity we therefore fix the relaxation parameter $\alpha_2 = 1$ and only vary the penalty parameter $\epsilon$.

**Value of the penalty parameter $\epsilon$**

The value of the penalty parameter $\epsilon$ is important in the sequential regularization approach. This parameter influences the convergence properties of the SR method, and it is this influence that will be the topic of investigation in this section. All simulations in this section are done using five sequential regularization steps at each time level. Figures 7.2 and 7.3 show the $u$ residual and

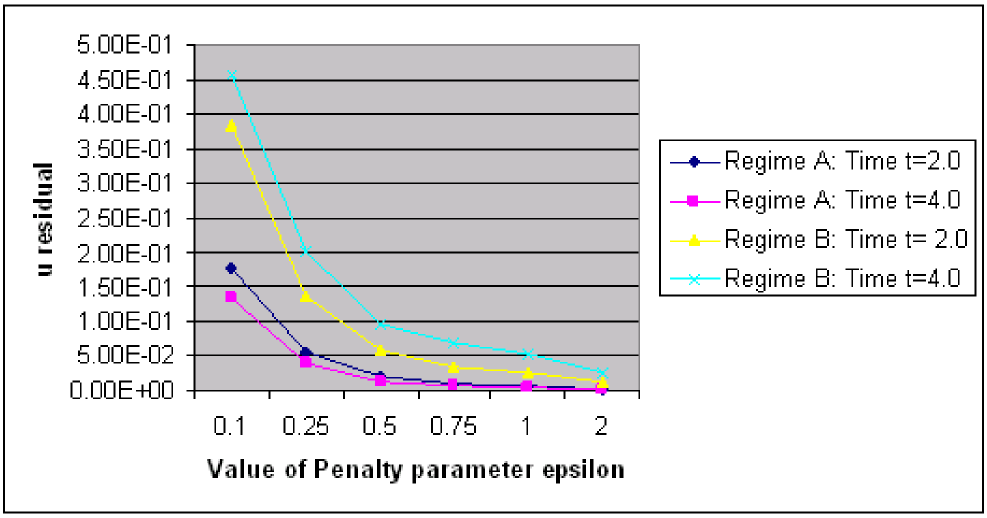

Figure 7.2: Residual in velocity $u$ as a function of the penalty parameter $\epsilon$.

divergence of the velocity, respectively, as a function of the penalty parameter $\epsilon$. Figure 7.2 shows that the $u$ residual decreases monotonically with an increasing value of $\epsilon$, while we have the opposite situation for the divergence as indicated in Figure 7.3: The divergence of the velocity field increases monotonically with increasing values of $\epsilon$. So we have to choose a large value of $\epsilon$ to get a desired small value for the $u$ residual, but this leads to a non-desirably large value for the divergence. Conversely, choosing a small value for $\epsilon$ leads to a desired small value of the divergence, but a non-desirably large value for the $u$ residual. It therefore appears that the choice of value for the penalty parameter $\epsilon$ must be a compromise; an intermediate value of 0.5 or 0.75 would be expected to give the most accurate results overall.

### Number of iterations for the momentum equations

In the SR approach, a modified set of momentum equations are solved through the use of an iterative method. Basically the momentum equations are decou-

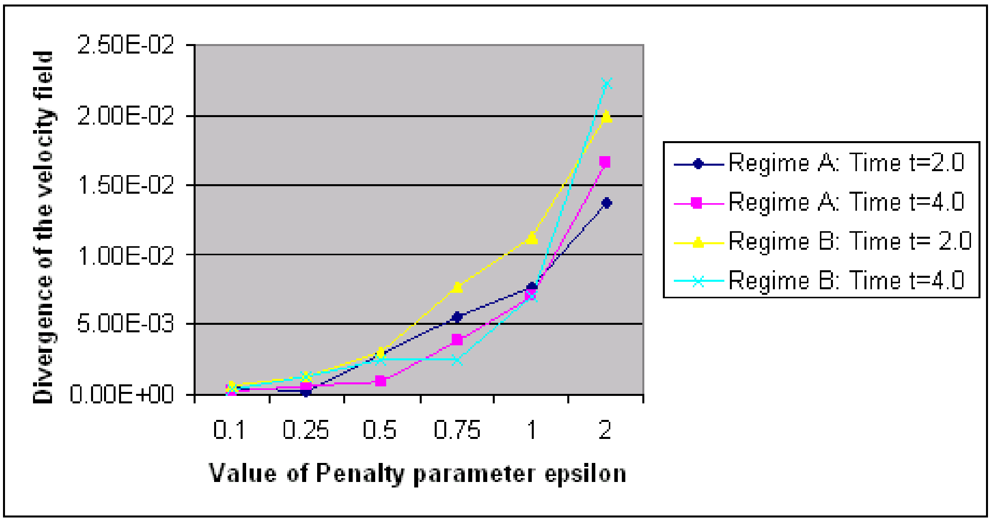

Figure 7.3: Divergence of the velocity as a function of the penalty parameter $\epsilon$.

pled, and at each iteration step one first solves for $u$ assuming a previous known value for $v$, and one then solves for $v$ using the recently obtained $u$. Obtaining an accurate velocity field is important for the success of the SR approach. In this section we would therefore like to investigate the impact of the number of iterations on the simulation results. All simulations in this section are done with five sequential regularization steps and a penalty parameter $\epsilon = 0.5$.

Table 7.4 displays the residuals in the $u$ velocity and the divergence of the velocity field at two different output times for each of the regimes A and B. We observe that the residuals for $u$ decrease with an increasing number of iterations, as expected. The divergence of the velocity should ideally be zero, and Table 7.4 shows a decreasing divergence when the number of iterations increase.

In addition to studying the effect of the number of iterations on the velocity residual and the divergence of the velocity, we would also like to find out the effect the number of iterations has on the solution itself. One way of examining this is to compare the location and shape of the bubble front obtained by using different numbers of iterations. In particular, Figures 7.4 - 7.7 compare the

| Regime | Time | $N$ | $u$ residual | Divergence |
|---|---|---|---|---|
| A | $t = 2.0$ | 10 | 1.64E-01 | 3.73E-03 |
| | | 30 | 2.03E-02 | 2.93E-03 |
| | | 50 | 4.06E-03 | 2.81E-03 |
| | $t = 4.0$ | 10 | 1.30E-01 | 2.04E-03 |
| | | 30 | 1.42E-01 | 8.87E-04 |
| | | 50 | 4.20E-03 | 7.93E-04 |
| B | $t = 2.0$ | 10 | 3.01E-01 | 4.45E-03 |
| | | 30 | 5.82E-02 | 3.07E-03 |
| | | 50 | 3.07E-02 | 2.98E-03 |
| | $t = 4.0$ | 10 | 3.74E-01 | 1.18E-03 |
| | | 30 | 9.76E-02 | 2.57E-03 |
| | | 50 | 5.98E-02 | 2.83E-03 |

Table 7.4: Residuals for the velocity $u$ and the computed divergence for an increasing number of iteration steps $N$

bubble front obtained using 10, 30, and 50 iterations for two different output times for regimes A and B. The four figures all show that there is a considerable difference between the position of the bubble front found using 10 iterations and when using 30 or 50 iterations. However, the differences in the bubble position obtained by using 30 and 50 iterations are very small. All the differences are considerably larger for regime B than regime A - this is natural as the rise velocity is larger in regime B than in regime A. The results indicate that 10 iterations is insufficient, while 30 iterations may be sufficient.

### Number of sequential regularization steps $M$

One of the important choices one have to make when applying the sequential regularization approach, is to decide the number of regularization steps to use. Computational cost increases with the number of steps, so it is desirable to find the minimum number of steps required to satisfy certain accuracy requirements. This is indeed the topic of this section as we study the impact the number of

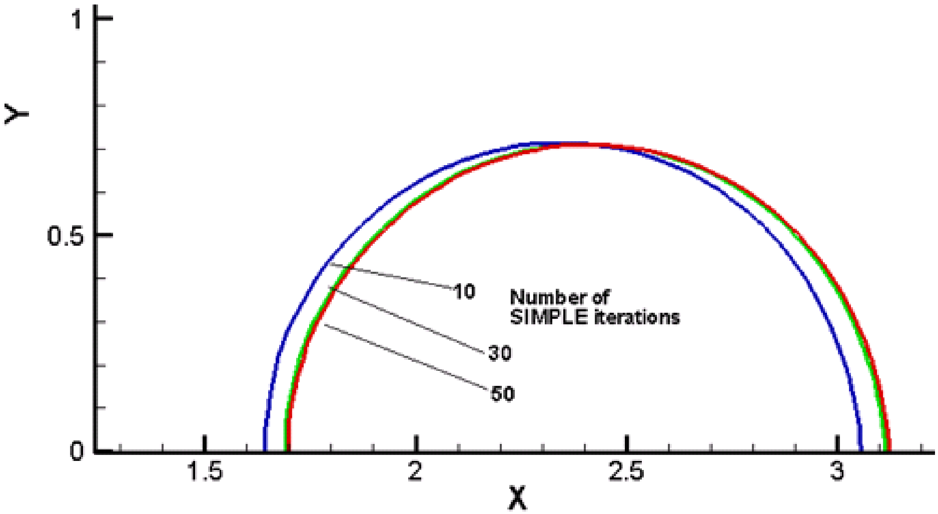

Figure 7.4: Regime A: The bubble front at time $t = 2.0$ for different numbers of iterations.

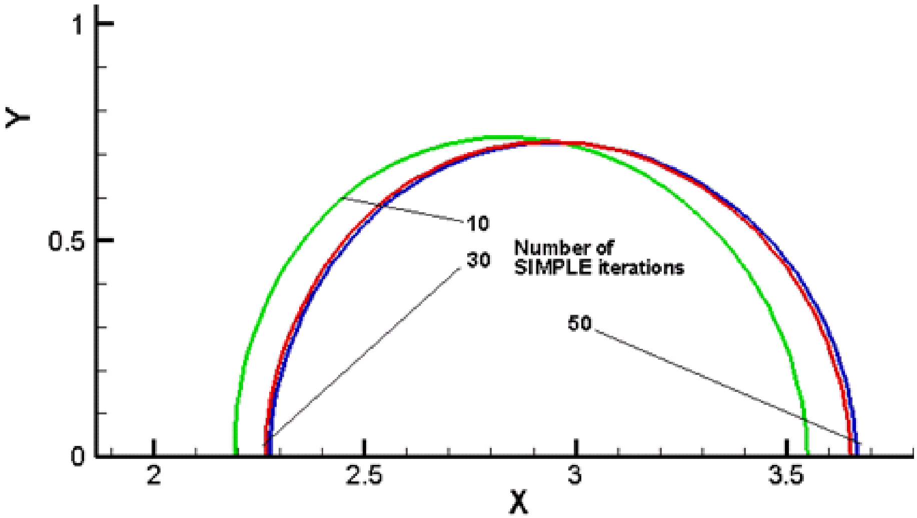

Figure 7.5: Regime A: The bubble front at time $t = 4.0$ for different numbers of iterations.

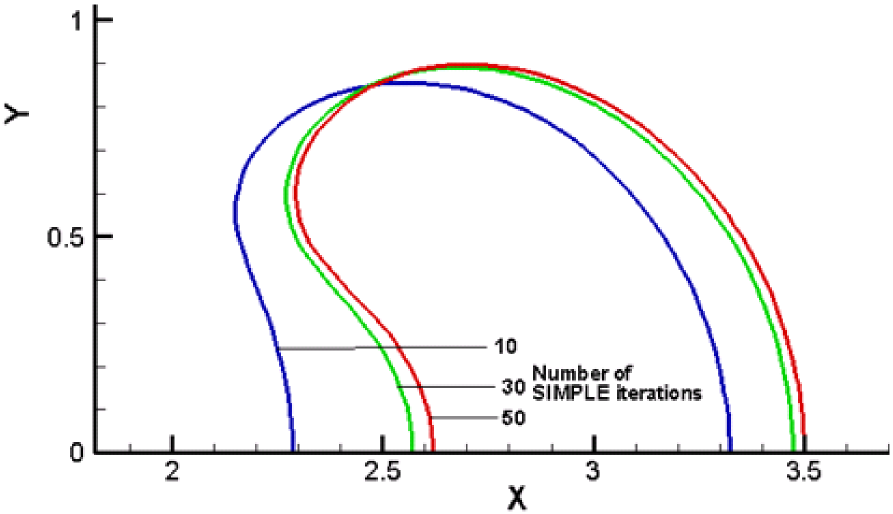

Figure 7.6: Regime B: The bubble front at time $t = 2.0$ for different numbers of iterations.

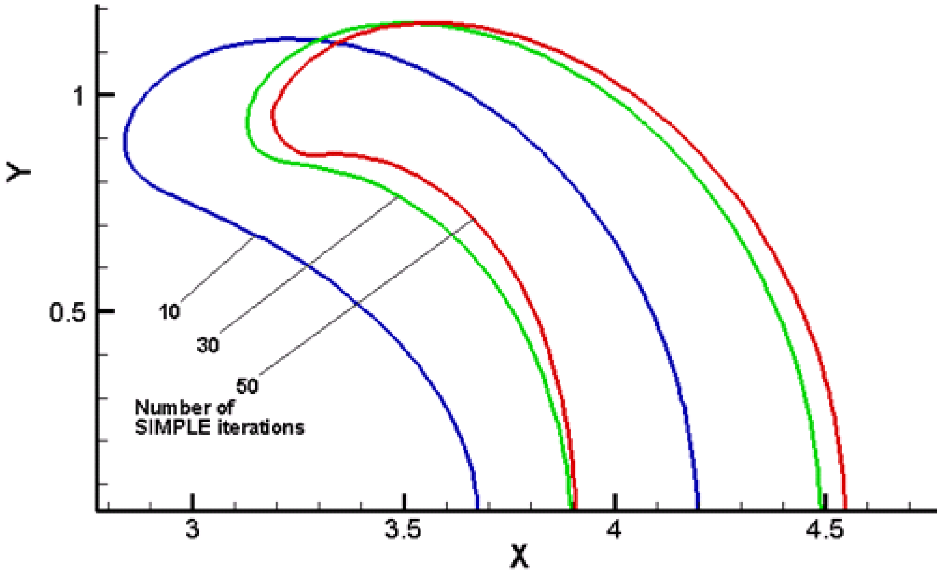

Figure 7.7: Regime B: The bubble front at time $t = 4.0$ for different numbers of iterations.

steps has on the numerical results. All simulations in this section are done with 30 iterations and a penalty parameter $\epsilon = 0.5$. Figures 7.8 and 7.9 show the $u$ residual and the divergence of the velocity field, respectively, as a function of the number regularization steps. Figure 7.8 shows that there is practically no difference in the $u$ residual when using five and 10 SR steps. However, increasing the number of steps from 10 to 15 actually leads to a dramatic increase in the residual for the $u$ velocity. The computed divergence decreases moderately from five to 10 SR steps as indicated in Figure 7.9. The same figure also shows that a further increase to 15 SR steps entails an abrupt increase in the divergence.

Based on the above, one may conclude that five SR steps is sufficient as there appear to be no significant improvement in the results by increasing the number of SR steps to 10. The increase in residual and divergence when increasing from 10 to 15 steps is due to our choice $\alpha_1 = 0$ which generates a weak instability in updating the pressure and thus taking effect in calculating the velocity as well. To investigate this further, an additional simulation for a rising bubble in regime B was carried out using 30 SR steps. This simulation broke down after only 13 time steps. However, this is not an issue here since in our numerical experiments five SR steps are often enough to reach the best accuracy, and no problem of such nature was ever encountered for simulations using 10 or less steps.

### 7.3.3 Conclusions on the SIMPLE-SR method

We here summarize the main findings with respect to values of key parameters in the SIMPLE-SR method:

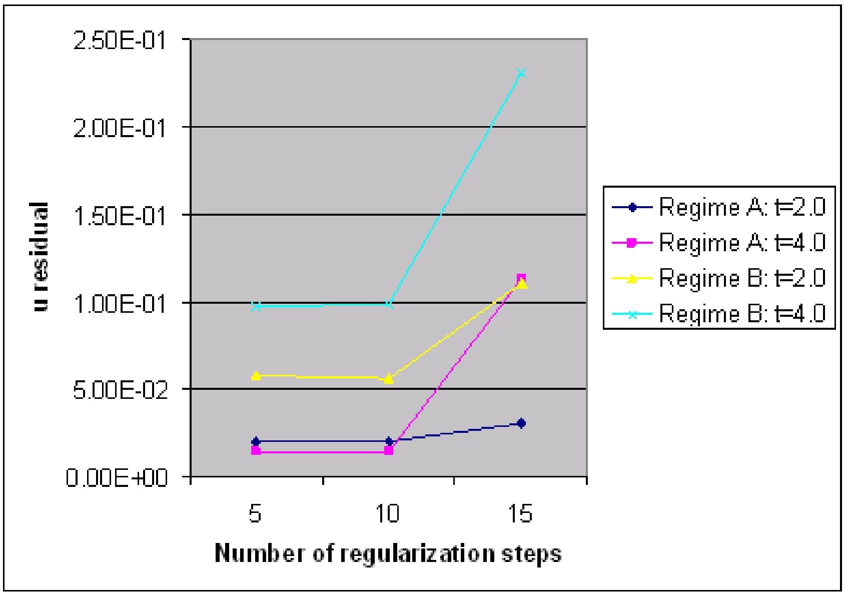

Figure 7.8: Residuals in the $u$ velocity as a function of the number of regularization steps used.

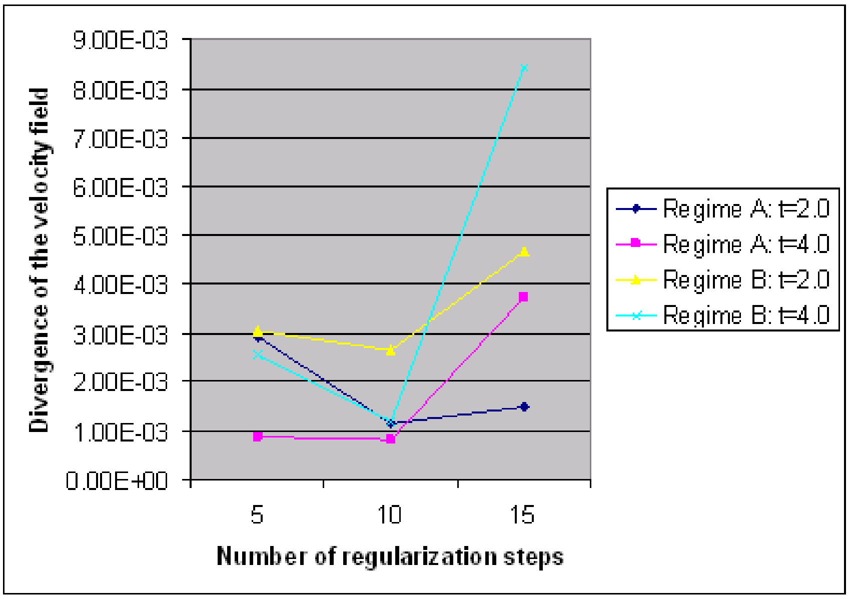

Figure 7.9: Divergence of the velocity field as a function of the number of regularization steps used.

- The number of iterations needed in the solution of the momentum equations are at least 30 - perhaps even as much as 50 iterations are required to obtain accurate results. A more thorough investigation including developing more appropriate semi-explicit schemes and more efficient iterative linear system solvers for the SR based momentum equation is in need.

- The required number of SR steps at each time step is not high - five steps seem to be sufficient. An increase to 10 steps did not show any significant improvement in the results, while an increase to 15 actually saw a deterioration of some results. Attempting to use 30 steps led to a breakdown in the simulation, which is caused by a weak instability in the pressure variable when $\alpha_1 = 0$ (cf. [62, 68]). However, no such problem has been observed for five and 10 steps.

- Choosing a low value of the penalty parameter $\epsilon$ gives low values for the divergence and high values for the $u$ residual, while high values of $\epsilon$ gives low values for the $u$ residual and high values for the divergence. It therefore appears that an intermediate value of 0.5 or 0.75 gives the most accurate overall results.

One may conclude that the SIMPLE-SR approach looks feasible through our numerical experiments and obviously simpler (avoiding solving the pressure correction equation) than the SIMPLE approach as presented in Chapter 3 of this thesis, but further investigation, especially developing better momentum equations solvers, would be required to improve its efficiency and robustness.

# Chapter 8

# Closure

The main pursuit of this thesis work has been the development and implementation of a direct numerical simulation algorithm for three-dimensional multiphase flows with applications to gas bubbles rising in quiescent viscous liquids. In this final Chapter we present a summary of the main conclusions from this work and also look to the future with some recommendations for potential further work in the area.

## 8.1 Conclusions

**Numerical method** The numerical method developed in this thesis has proven to be robust for the simulation of gas bubbles rising in viscous liquids for a wide range of Reynolds and Bond numbers. We attribute this robustness to the combination of several powerful components as highlighted in the below conclusions:

- The large density and viscosity ratios typical of realistic multiphase flows pose a significant challenge for the flow solver. In this work we used an iterative finite volume method based on the SIMPLE approach to solve the 'one-fluid' formulation of the flow equations. Due to the density jump across the interface, volume conservation rather than the traditional mass conservation was enforced for the control volumes, and the resulting method successfully handles large density and viscosity ratios.

- Complex flow physics near the moving interface require fairly high mesh resolution in this region, potentially making the method excessively expensive from a computational point of view. We here handled this challenge by using PARAMESH, an block-based, adaptive mesh refinement tool for parallel computing that allows high-resolution meshes only where needed.
- A front tracking approach was adopted to handle the moving interface whereby a separate triangular mesh represents the bubble surface. The surface is then advected using a velocity obtained from the surrounding flow field, and mesh adaptation was introduced to retain a uniform mesh quality. Peskin's smoothing technique was also adopted to avoid numerical oscillations due to discontinuities in material properties across the interface.
- In the pursuit of improving the flow solver further, the governing flow equations were reformulated through the use of a sequential regularization method, a novel approach in the context of multiphase flows. The new approach looks feasible based on analysis carried out in a two-dimensional setting, though further investigation would be required to draw more definite conclusions.

**Results and applications** The numerical method was put through thorough testing and applied to challenging systems of bubble flows to gain further insights into the prevailing flow physics. Below we summarize the main findings:

- The current simulation methodology is implemented for parallel processing, making it powerful both in terms of memory and CPU requirements. Nevertheless, three-dimensional simulations still remain computationally expensive, and sensitivity analyses were therefore carried out with the aim of minimizing computational demand while retaining an acceptable accuracy in the simulation results:
  - It was found that a computational domain size of eight bubble diameters in each spatial dimension was sufficient to avoid wall containment effects for the rising bubbles.
  - The mesh resolution in the vicinity of the rising bubble was found to be sufficient when using 16 grid cells across the diameter of the bubble.
- The flow equations were formulated in a non-inertial reference frame with the rising bubble fixed in the moving frame to allow for long-duration simulations without having to increase the domain size. To achieve this, the acceleration of the moving reference frame had to be estimated since the rise velocity of the bubble is not known. To assess the impact of this approach, results obtained in moving and stationary reference frames were carefully compared in terms of transient bubble shapes, rise velocities, flow streamlines and pressure distributions. Reasonable agreement was found in all cases.
- A crucial assessment of any mathematical model is the comparison of simulation results with experimental data:
  - We validated the method in terms of terminal bubble shape and rise velocity for Reynolds numbers up to around 100 with excellent agreement between experimental and simulation results.

  - Air bubbles rising in water have proven to be difficult to simulate. We presented simulation results for this system with bubble diameters ranging from 0.5 mm to 30 mm, a wider range than previously reported in the literature. The rise velocities agree well with the experimental results of Tomiyama [111] throughout the diameter range.

- With confidence from the above-mentioned validation, we applied the simulation algorithm to investigate two bubble phenomena:

  - The mechanisms triggering path instability of rising bubbles are not fully understood despite recent progress in the area. Our simulations reproduced rectilinear, zig-zag and spiral rise paths with less restrictive model assumptions than we have seen elsewhere in the literature. Analysing the results, we made some observations about the relationship between rise patterns and associated wake structures.
  - We extended our applications from single bubbles rising to study the interaction between two rising bubbles. This application illustrated how our front tracking approach is able to handle the merging of two rising bubbles into one single bubble.

## 8.2 Outlook and recommendations

It is the hope of the author that the numerical simulation methodology and results presented herein constitute a small contribution to the research on computational multiphase flows. We here discuss briefly how the method and applications could be improved, and we make some recommendations on further avenues that may be worth pursuing.

- Even though the current simulation approach utilizes parallel processing, the study of a bubble rising for a long period is still very time-consuming. The iterative flow solver requires a fairly high number of iterations at each time step, and a decrease in the number of iterations required would proportionally decrease the simulation time. The integration of a multigrid technique ([14]) within the PARAMESH grid framework is one suggestion that may help improve convergence and hence reduce the computational time required.

- The use of a moving reference frame proved particularly useful for studying long-term behaviour of rising bubbles. Section 4.2.3 showed that the results obtained in a moving frame are essentially the same as when a stationary frame is used. However, there are some differences observed in the transient rise velocities, and this is probably due to the way the acceleration of the non-inertial frame is estimated. The situation may be improved by an alternative estimation of the acceleration, or possibly by treating the acceleration as an unknown while adding an additional constraint.

- The bubble front is currently advected explicitly using a forward Euler approach according to Equation 3.13. It is believed that an alternative approach like backward Euler or a Runge-Kutta method would improve accuracy in the advection process, probably allowing larger time steps as well.

- Both volume conservation and the merging of interfaces is currently handled in a purely geometric manner. Though this seems to be a common approach in the front tracking context, it is highly desirable to take fluid physics into account in these situations. This also applies to a phenomena that has not been modelled in this work - namely the break-up of bubbles.

- The rise velocities of air bubbles in water for a wide range of diameters agree well with the experiments of Tomiyama [111]. However, there are significant differences in experimental rise velocities reported by researchers, often attributed to varying degree of surfactants and/or initial bubble deformations. It would therefore be very interesting to add surfactants and vary the initial bubble deformation using our simulation algorithm to see if we could reproduce the differences reported by experimentalists.

- Path instability of rising bubbles: We made some basic observations on the relationship between rise paths and the associated wake structures. Further analysis of these results could help shed light on the fundamental mechanisms involved in this intriguing phenomenon.

- Bubble-bubble interaction: We showed how our front tracking method could be used to simulate the interaction and possible merging of two rising bubbles. This approach could be extended to multiple bubbles, and potentially to bubbly flows, by distributing the bubble interfaces evenly between the processors available.

- The reformulation of the two-dimensional flow equations through a sequential regularization method avoids solving the pressure-correction equation, and reasonable results were obtained. However, further investigation and development of better momentum equation solvers would be required to improve its efficient and robustness.

# Bibliography

[1] D.M. Anderson, G.B. McFadden, and A.A. Wheeler, *Diffuse-Interface Methods in Fluid Mechanics*, Annu. Rev. Fluid Mech. **30** (1998), 139–165.

[2] U.M. Ascher and P. Lin, *Sequential regularization methods for higher index DAEs with constraint singularities: The linear index-2 case*, SIAM J. Numer. Anal. **33** (1996), 1921–1940.

[3] U.M. Ascher and P. Lin, *Sequential regularization methods for nonlinear higher-index DAEs*, SIAM J. Sci. Comput. **18** (1997), 160–181.

[4] N.M. Aybers and A. Tapucu, *The motion of gas bubbles rising through stagnant liquid*, Wärme- und Stoffübertragung **2** (1969), 118–128.

[5] G.K. Batchelor, *An Introduction to Fluid Dynamics*, Cambridge University Press, 1967.

[6] D. Bhaga and M.E. Weber, *Bubbles in viscous liquids: shapes, wakes and velocities*, J. Fluid Mech. **105** (1981), 61–85.

[7] A. Blanco and J. Magnaudet, *The structure of the axisymmetric high-Reynolds number flow around an ellipsoidal bubble of fixed shape*, Phys. Fluids **7** (1995), 1265.

[8] T. Bonometti and J. Magnaudet, *Transition from spherical cap to toroidal bubbles*, Phys. Fluids **18** (2006), 052102.

[9] D. Bothe, M. Schmidtke, and H.J. Warnecke, *Direct numerical computation of the lift force acting on single bubbles*, International Conference on Multiphase Flow, Leipzig, Germany, July 2007.

[10] L.A. Bozzi, J.Q. Feng, T.C. Scott, and A.J. Pearlstein, *Steady axisymmetric motion of deformable drops falling or rising through a homoviscous fluid in a tube at intermediate Reynolds number*, J. Fluid Mech. **336** (1997), 1.

[11] J. U. Brackbill, D. B. Kothe, and C. Zemach, *A Continuum Method for Modeling Surface Tension*, J. Comput. Phys. **100** (1992), 335–354.

[12] K.E. Brenan, S.L. Campbell, and L.R. Petzold, *Numerical solution of initial-value problems in differential-algebraic equations*, Society for Industrial and Applied Mathematics, 1996, First published in 1989 by North-Holland, New York.

[13] G. Brereton and D. Korotney, *Coaxial and oblique coalescence of two rising bubbles*, Dynamics of bubbles and vortices near a free surface, ASME Applied Mechanics Conference, Columbus, Ohio, June 1991.

[14] W.L. Briggs, V.E. Henson, and S.F. McCormick, *A Multigrid Tutorial*, 2nd ed., The Society for Industrial and Applied Mathematics, 2000.

[15] Bernard Bunner and Grétar Tryggvason, *Dynamics of homogeneous bubbly flows. Part 1. Rise velocity and microstructure of the bubbles*, J. Fluid Mech. **466** (2002), 17–52.

[16] M. Bussmann, J. Mostaghimi, and S. Chandra, *On a three-dimensional volume tracking model of droplet impact*, Phys. Fluids **11** (1999), no. 6, 1406–1417.

[17] R. Caiden, R.P. Fedkiw, and C. Anderson, *A Numerical Method for Two-Phase Flow Consisting of Separate Compressible and Incompressible Regions*, J. Comp. Phys. **166** (2001), 1–27.

[18] H.D. Ceniceros, R.L. Nós, and A.M. Roma, *Three-dimensional, fully adaptive simulations of phase-field fluid models*, J. Comput. Phys. **229** (2010), 6135–6155.

[19] L. Chen, S.V. Garimella, J.A. Reizes, and E. Leonardi, *Motion of interacting gas bubbles in a viscous liquid including wall effects and evaporation*, Num. Heat Transf. Part A **31** (1997), no. 6, 629–654.

[20] L. Chen, Y. Li, and R. Manasseh, *The coalescence of bubbles - a numerical study*, Third International Conference on Multiphase flow, June 1998.

[21] Li Chen, Suresh V. Garimella, John A. Reizes, and Eddie Leonardi, *The development of a bubble rising in a viscous liquid*, J. Fluid Mech. **387** (1999), 61–96.

[22] M. Cheng, J. Hua, and J. Lou, *Simulation of bubble-bubble interaction using a lattice boltzmann method*, Comput. Fluids (2009), In Press.

[23] R. Clift, J.R. Grace, and M.E. Weber, *Bubbles, Drops, and Particles*, Academic Press, 1978.

[24] R.M. Davies and F.I. Taylor, *The mechanism of large bubbles rising through extended liquids and through liquids in tubes*, Proc. R. Soc. Lond. **A 200** (1950), 375.

[25] A.W.G. de Vries, *Path and wake of a rising bubble*, Ph.D. thesis, University of Twente, 2001.

[26] W. Dijkhuizen, M. Van Sint Annaland, and J.A.M. Kuipers, *Numerical and experimental investigation of the lift force on single bubbles*, Chem. Eng. Sci. (2009), In Press.

[27] W. Dijkhuizen, I. Roghair, M. Van Sint Annaland, and J.A.M. Kuipers, *DNS of gas bubbles behaviour using an improved 3D front tracking model - drag force on isolated bubbles and comparison with experiments*, Chem. Eng. Sci. (2009), In Press.

[28] W. Dijkhuizen, I. Roghair, M. Van Sint Annaland, and J.A.M. Kuipers, *DNS of gas bubbles behaviour using an improved 3D front tracking model - model development*, Chem. Eng. Sci. (2009), In Press.

[29] W. Dijkhuizen, E.I.V. van den Hengel, N.G. Deen, M. van Sint Annaland, and J.A.M. Kuipers, *Numerical investigation of closures for interface forces acting on single air-bubbles in water using Volume of Fluid and Front Tracking models*, Chem. Eng. Sci. **60** (2005), 6169–6175.

[30] J. Du, B. Fix, J. Glimm, X. Jia, X. Li, Y. Li, and L. Wu, *A simple package for front tracking*, J. Comput. Phys **213** (2006), 613–628.

[31] P.C. Duineveld, *The rise velocity and shape of bubbles in pure water at high Reynolds number*, J. Fluid Mech. **292** (1995), 325–332.

[32] K. Ellingsen and F. Risso, *On the rise of an ellipsoidal bubble in water: oscillatory paths and liquid-induced velocity*, J. Fluid Mech. **440** (2001), 235–268.

[33] A. Esmaeeli and G. Tryggvason, *A direct numerical simulation study of buoyant rise of bubbles at O(100) Reynolds number*, Phys. Fluids **17** (2005), 093303.

[34] Aaron L. Fogelson and Charles S. Peskin, *A Fast Numerical Method for Solving the Three-Dimensional Stokes' Equations in the Presence of Suspended Particles*, J. Comput. Phys. **79** (1988), 50–69.

[35] J. Glimm, J. Grove, B. Lindquist, O. McBryan, and G. Tryggvason, *The bifurcation of tracked scalar waves*, SIAM J. Sci. Statist. Comput. **9** (1988), no. 1, 61–79.

[36] J. Glimm, J.W. Grove, X.L. Li, and D.C. Tan, *Robust computational algorithms for dynamic interface tracking in three dimensions*, SIAM J. Sci. Comput. **21** (1999), no. 6, 2240–2256.

[37] J. Glimm, E. Isaacson, D. Marchesin, and O. McBryan, *Front Tracking for Hyperbolic Systems*, Adv. Appl. Math. **2** (1981), 91–119.

[38] J. Glimm, O. McBryan, R. Menikoff, and D.H. Sharp, *Front tracking applied to Rayleigh-Taylor instability*, SIAM J. Sci. Statist. Comput. **7** (1986), no. 1, 230–251.

[39] P.M. Gresho, *Some current issues relevant to the incompressible Navier-Stokes equations*, Comput. Methods Appl. Mech. Engrg. **87** (1987), 201–252.

[40] E. Hairer and G. Wanner, *Solving ordinary differential equations II: Stiff and differential-algebraic problems*, second revised 1996 ed., Springer series in computational mathematics, vol. 14, Springer Verlag, 1991.

[41] J. Han and G. Tryggvason, *Secondary breakup of axisymmetric liquid drops. I. Acceleration by a constant body force*, Phys. Fluids **11** (1999), no. 12.

[42] J. Han and G. Tryggvason, *Secondary breakup of axisymmetric liquid drops. II. Impulsive acceleration*, Phys. Fluids **13** (2001), no. 6.

[43] R.A. Hartunian and W.R. Sears, *On the instability of small gas bubbles moving uniformly in various liquids*, J. Fluid Mech. **3** (1957), 27.

[44] C.W. Hirt and B.D. Nichols, *The volume of fluid (vof) method for the dynamics of free boundaries*, J. Comput. Phys **39** (1981), 210.

[45] T.Y. Hou, J.S. Lowengrub, and M.J. Shelley, *Boundary Integral Methods for Multicomponent Fluids and Multiphase Materials*, J. Comput. Phys. **169** (2001), 302–362.

[46] H.H Hu, N.A. Patankar, and M.Y. Zhu, *Direct numerical simulation of fluid-solid systems using the arbitrary Lagrangian-Eulerian technique*, J. Comput. Phys. **169** (2001), 427.

[47] J. Hua, P. Lin, and J.F. Stene, *Numerical Simulation of Gas Bubbles Rising in Viscous Liquids at High Reynolds Number*, Moving Interface Problems and Applications in Fluid Dynamics, Contemporary Mathematics, vol. 466, American Math. Society, 2008.

[48] J. Hua, J.F. Stene, and P. Lin, *Numerical Simulation of Gas Bubbles Rising in Viscous Liquids at High Reynolds Number*, 6th International Conference on Multiphase Flow, 2007, Paper No. 431.

[49] J. Hua, J.F. Stene, and P. Lin, *Numerical simulation of 3D bubbles rising in viscous liquids using a front tracking method*, J. Comput. Phys. **227** (2008), 3358–3382.

[50] Jinsong Hua and Jing Lou, *Numerical simulation of bubble rising in viscous liquid*, J. Comput. Phys. **222** (2007), 769–795.

[51] M. Ida, *An improved unified solver for compressible and incompressible fluids involving free surfaces. Part I. Convection.*, Comput. Phys. Commun. **132** (2000), 44.

[52] D. Jacqmin, *Calculation of two-phase Navier-Stokes flows using phase-field modeling*, J. Comput. Phys **155** (1999), 96.

[53] M. Jenny, J. Dušek, and G. Bouchet, *Instabilities and transition of a sphere falling or ascending freely in a Newtonian fluid*, J. Fluid Mech. **508** (2004), 201–239.

[54] T.A. Johnson and V.C. Patel, *Flow past a sphere up to a Reynolds number of 300*, J. Fluid Mech. **378** (1999), 19–70.

[55] D. Juric and G. Tryggvason, *A front-tracking method for dendritic solidification*, J. Comput. Phys. **123** (1996), 127–148.

[56] I.S. Kang and L.G. Leal, *Numerical solution of axisymmetric, unsteady free-boundary problems at finite Reynolds number. I. Finite-difference scheme and its application to the deformation of a bubble in a uniaxial straining flow*, Phys. Fluids **30** (1987), 1929.

[57] J. Katz and C. Meneveau, *Wake-induced relative motion of bubbles rising in line*, Int. J. Multiphase Flow **22** (1996), no. 2, 239–258.

[58] M. Koebe, D. Bothe, J. Pruess, and H.-J. Warnecke, *3D Direct Numerical Simulation of Air Bubbles in Water at High Reynolds Number*, Fluids Engineering Division Summer Meeting, ASME, July 2002, Montreal, Quebec, Canada.

[59] R. Krishna, M.I. Urseanu, J.M. van Baten, and J. Ellenberger, *Wall effects on the rise of single gas bubbles in liquids*, Int. Commun. Heat Mass Transfer **26** (1999), 781.

[60] R. LeVeque and Z. Li, *The Immersed Interface Method for Elliptic Equations with Discontinuous Coefficients and Singular Sources*, SIAM J. Numer. Anal. **31** (1994), no. 4, 1099–1044.

[61] Z. Li and K. Ito, *The Immersed Interface Method*, SIAM, 2006.

[62] P. Lin, *A sequential regularization method for time-dependent incompressible Navier-Stokes equations*, SIAM J. Numer. Anal. **34** (1997), no. 3, 1051–1071.

[63] P. Lin, X. Chen, and M.T. Ong, *Finite element methods based on a new formulation for the non-stationary incompressible Navier-Stokes equations*, Int. J. Numer. Meth. Fluids **46** (2004), 1169–1180.

[64] P. Lin, Q. Guo, and X. Chen, *A fully explicit method for incompressible flow computation*, Comput. Methods Appl. Mech. Engrg. **192** (2003), 2555–2564.

[65] P. Lin, J.-G. Liu, and X. Lu, *Long time numerical solution of the Navier-Stokes equations based on a sequential regularization formulation*, SIAM J. Sci. Comput. **31** (2008), no. 1, 398–419.

[66] J.T. Lindt, *On the periodic nature of the drag on a rising bubble*, Chem. Eng. Sci. **27** (1972), 1775–1781.

[67] J. Lu, S. Biswas, and G. Tryggvason, *A DNS study of laminar bubbly flows in a vertical channel*, Int. J. Multiphase Flow **32** (2006), 643–660.

[68] X. Lu, P. Lin, and J.-G. Liu, *Analysis of a sequential regularization method for the unsteady Navier-Stokes equations*, Math. Comp. **77** (2008), no. 263, 1467–1494.

[69] K. Lunde and R. Perkins, *Observations on wakes behind spheroidal bubbles and particles*, Fluids Engineering Division Summer Meeting, ASME, June 1997.

[70] Peter MacNeice, Kevin M. Olson, Clark Mobarry, Rosalinda de Fainchtein, and Charles Packer, *PARAMESH: A parallel adaptive mesh refinement community toolkit*, Comput. Phys. Commun. **126** (2000), 330–354.

[71] J. Magnaudet and I. Eames, *The motion of high-reynolds-number bubbles in inhomogeneous flow*, Annu. Rev. Fluid Mech. **32** (2000), 659.

[72] J. Magnaudet and G. Mougin, *Wake instability of a fixed spheroidal bubble*, J. Fluid Mech. **572** (2007), 311–337.

[73] M. Manga and H.A. Stone, *Collective hydrodynamics of deformable drops and bubbles in dilute low Reynolds number suspensions*, J. Fluid Mech. **300** (1995), 231–263.

[74] T. Maxworthy, C. Gnann, M. Kürten, and F. Durst, *Experiments on the rise of air bubbles in clean viscous liquids*, J. Fluid Mech. **321** (1996), 421–441.

[75] D.I. Meiron, *On the stability of gas bubbles rising in an inviscid fluid*, J. Fluid Mech. **198** (1989), 101–114.

[76] D.W. Moore, *The rise of a gas bubble in viscous liquid*, J. Fluid Mech. **6** (1959), 113.

[77] M. Moradoglu and G. Tryggvason, *A front-tracking method for computation of interfacial flows with soluble surfactants*, J. Comput. Phys. **227** (2008), 2238–2262.

[78] G. Mougin and J. Magnaudet, *The generalized Kirchhoff equations and their application to the interaction between a rigid body and an arbitrary time-dependent viscous flow*, Int. J. Multiphase Flow **28** (2002), 1837–1851.

[79] G. Mougin and J. Magnaudet, *Path instability of a rising bubble*, Phys. Rev. Lett. **88** (2002), no. 1.

[80] Guillaume Mougin and Jacques Magnaudet, *Wake-induced forces and torques on a zigzagging/spiralling bubble*, J. Fluid Mech. **567** (2006), 185–194.

[81] K. Mukundakrishnan, S. Quan, D.M. Eckmann, and P.S. Ayyaswamy, *Numerical study of wall effects on buoyant gas-bubble rise in liquid-filled finite cylinder*, Phys. Rev. E **76** (2007).

[82] M. Ohta, T. Imura, Y. Yoshida, and M. Sussman, *A computational study of the effect of initial bubble conditions on the motion of a gas bubble rising in viscous liquids*, Int. J. Multiphase Flow **31** (2005), 223.

[83] S. Osher and R.P. Fedkiw, *Level set methods: an overview and some recent results*, J. Comput. Phys **169** (2001), 463.

[84] S. Osher and R.P. Fedkiw, *Level Set Methods and Dynamic Implicit Surfaces*, Springer, 2002.

[85] S.J. Osher and J.A. Sethian, *Fronts propagating with curvature dependent speed. Algorithms based on Hamilton-Jacobi formulations*, J. Comput. Phys **79** (1988), 12.

[86] Suhas V. Patankar, *Numerical Heat Transfer and Fluid Flow*, series in computational methods in mechanics and thermal sciences, Taylor & Francis, 1980.

[87] Charles S. Peskin, *Numerical Analysis of Blood Flow in the Heart*, J. Comput. Phys. **25** (1977), 220–252.

[88] C.S. Peskin, *The Immersed Boundary Method*, Acta Numerica (2002).

[89] G. Pianet, S. Vincent, J. Leboi, J.P. Caltagirone, and M. Anderhuber, *Simulating compressible gas bubbles with a smooth volume tracking 1-Fluid method*, Int. J. Multiphase Flow **36** (2010), 273–283.

[90] C. Pozrikidis, *Interfacial Dynamics for Stokes Flow*, J. Comput. Phys. **169** (2001), 250–301.

[91] A. Prosperetti and G. Tryggvason, *Computational Methods for Multiphase Flow*, Cambridge University Press, 2007.

[92] Andrea Prosperetti, *Bubbles*, Phys. Fluids **16** (2004), no. 6.

[93] S.S. Rabha and V.V. Buwa, *Volume-of-fluid (VOF) simulations of rise of single/multiple bubbles in sheared liquids*, Chem. Eng Sci. (2009), In Press.

[94] R.D. Richtmyer and K.W. Morton, *Difference methods for initial-value problems*, Interscience publisher, John Wiley & Sons, 1967.

[95] W.J. Rider and D.B. Kothe, *Reconstructing Volume Tracking*, J. Comput. Phys. **141** (1998), 112–152.

[96] Henrik Rusche, *Computational Fluid Dynamics of Dispersed Two-Phase Flows at High Phase Fractions*, Ph.D. thesis, Imperial College, December 2002.

[97] G. Ryskin and L.G. Leal, *Numerical simulation of free-boundary problems in fluid mechanics. Part 2. Buoyancy-driven motion of a gas bubble through a quiescent liquid*, J. Fluid Mech. **148** (1984), 19.

[98] P.G. Saffman, *On the rise of small air bubbles in water*, J. Fluid Mech. **1** (1956), 249.

[99] R. Samulyak, J. Du, J. Glimm, and Z. Xu, *A numerical algorithm for MHD free surface flows at low magnetic Reynolds numbers*, J. Comput. Phys. **226** (2007), 1532–1549.

[100] T. Sanada, A. Sato, M. Shirota, and M. Watanabe, *Motion and coalescence of a pair of bubbles rising side by side*, Chem. Eng. Sci. **64** (2009), 2659–2671.

[101] A.S. Sangani, *Sedimentation in ordered emulsions of drops at low reynolds numbers*, ZAMP **38** (1987), 542.

[102] R. Scardovelli and S. Zaleski, *Direct numerical simulation of free-surface and interfacial flow*, Annu. Rev. Fluid Mech. **31** (1999), 567.

[103] J.A. Sethian, *Level Set Methods and Fast Marching Methods: Evolving Interfaces in Computational Geometry, Fluid Mechanics, Computer Vision, and Materials Science*, Cambridge University Press, 1999.

[104] W.L. Shew and J.-F. Pinton, *Viscoelastic effects on the dynamics of a rising bubble*, J. Stat. Mech. **P01009** (2006), ?

[105] S. Shin and D. Juric, *Modelling three-dimensional multiphase flow using a level contour reconstruction method for front tracking without connectivity*, J. Comput. Phys. **180** (2002), 427.

[106] A. Smolianski, H. Haario, and P. Luukka, *Vortex shedding behind a rising bubble and two-bubble coalscence: a numerical approach*, Appl. Math. Model. **29** (2005), 615–632.

[107] Mark Sussman, Peter Smereka, and Stanley Osher, *A Level Set Approach for Computing Solutions to Incompressible Two-Phase Flow*, J. Comput. Phys. **114** (1994), 146–159.

[108] M. Taeibi-Rahni, E. Loth, and G. Tryggvason, *Flow modulation of a planar free layer with large bubbles - direct numerical simulations*, Int. J. Multiphase Flow **20** (1994), no. 6, 1109–1128.

[109] T.D. Taylor and A. Acrivos, *On the deformation and drag of a falling viscous drop at low reynolds number*, J. Fluid Mech. **18** (1964), 466.

[110] S. Thomas, A. Esmaeeli, and G. Tryggvason, *Multiscale computations of thin films in multiphase flows*, Int. J. Multiphase Flow (2009), In Press.

[111] A. Tomiyama, G.P. Celata, S. Hosokawa, and S. Yoshida, *Terminal velocity of single bubbles in surface tension force dominant regime*, Int. J. Multiphase Flow **28** (2002), 1497.

[112] G. Tryggvason, B. Bunner, O. Ebrat, and W. Tauber, *Computations of multiphase flows by a finite difference/front tracking method. I. Multi-fluid flows*, Von Karman lecture notes, the Von Karman Institute (1998).

[113] G. Tryggvason, B. Bunner, A. Esmaeeli, D. Juric, N.Al-Rawahi, W. Tauber, J. Han, S. Nas, and Y.-J. Jan, *A Front-Tracking Method for the Computations of Multiphase Flow*, J. Comput. Phys. **169** (2001), 708–759.

[114] Salih Ozen Unverdi and Grétar Tryggvason, *A Front-Tracking Method for Viscous, Incompressible, Multi-fluid Flows*, J. Comput. Phys. **100** (1992), 25–37.

[115] M. van Sint Annaland, N.G. Deen, and J.A.M. Kuipers, *Numerical simulation of gas bubbles behaviour using a three-dimensional volume of fluid method*, Chem. Eng. Sci. **60** (2005), 2999–3011.

[116] M. van Sint Annaland, W. Dijkhuizen, N. G. Deen, and J. A. M. Kuipers, *Numerical Simulation of Behavior of Gas Bubbles Using a 3-D Front-Tracking Method*, AIChE J. **52** (2006), no. 1, 99–110.

[117] Christian Veldhuis, *Leonardo's Paradox: Path and Shape Instabilities of Particles and Bubbles*, Ph.D. thesis, University of Twente, 2007.

[118] M. Watanabe and T. Sanada, *In-line motion of a pair of bubbles in a viscous liquid*, JSME Int. J. Ser. B **49** (2006), no. 2, 410–418.

[119] M.M. Wu and M. Gharib, *Experimental studies on the shape and path of small air bubbles rising in clean water*, Phys. Fluids **14** (2002), L49.

[120] B. Yang, A. Prosperetti, and S. Takagi, *The transient rise of a bubble subject to shape or volume changes*, Phys. Fluids **15** (2003), 2640.

[121] G.H. Yeoh and J. Tu, *Computational Techniques for Multiphase Flows*, Butterworth-Heinemann, 2009.

[122] C. Zhou, P. Yue, J.J. Feng, C.F. Ollivier-Gooch, and H.H. Hu, *3D phase-field simulations of interfacial dynamics in Newtonian and viscoelastic fluids*, J. Comput. Phys. **229** (2010), 498–511.